1991-06

A wind tunnel study of the Pioneer remotely piloted vehicle

Bray, Robert M.

Monterey, California. Naval Postgraduate School

NAVAL POSTGRADUATE SCHOOL

Monterey, California

THESIS

A WIND TUNNEL STUDY
OF THE
PIONEER REMOTELY PILOTED VEHICLE

by

Robert M. Bray

June, 1991

Thesis Advisor: Richard M. Howard

Approved for public release; distribution is unlimited

Unclassified

Security Classification of this page

REPORT DOCUMENTATION PAGE

1a Report Security Classification: Unclassified
1b Restrictive Markings
2a Security Classification Authority
3 Distribution Availability of Report: Approved for public release; distribution is unlimited.
2b Declassification/Downgrading Schedule
4 Performing Organization Report Number(s)
5 Monitoring Organization Report Number(s)
6a Name of Performing Organization: Naval Postgraduate School
6b Office Symbol (*If Applicable*): 33
7a Name of Monitoring Organization: Naval Postgraduate School
6c Address (*city, state, and ZIP code*): Monterey, CA 93943-5000
7b Address (*city, state, and ZIP code*): Monterey, CA 93943-5000
8a Name of Funding/Sponsoring Organization
8b Office Symbol (*If Applicable*)
9 Procurement Instrument Identification Number
8c Address (*city, state, and ZIP code*)
10 Source of Funding Numbers

Program Element Number	Project No	Task No	Work Unit Accession No

11 Title (*Include Security Classification*): A Wind Tunnel Study of the Pioneer Remotely Piloted Vehicle

12 Personal Author(s): Robert M. Bray

13a Type of Report	13b Time Covered From	To	14 Date of Report (*year, month,day*)	15 Page Count
Master's Thesis			June 1991	144

16 Supplementary Notation: The views expressed in this thesis are those of the author and do not reflect the official policy or position of the Department of Defense or the U.S. Government.

17 Cosati Codes			18 Subject Terms (*continue on reverse if necessary and identify by block number*)
Field	Group	Subgroup	RPV, UAV, Wind Tunnel, Stability and Control, Simulation, Flight Performance.

19 Abstract (*continue on reverse if necessary and identify by block number*)

Remotely Piloted Vehicles (RPVs) performed impressively well in the recent Gulf War. The Pioneer RPV has been fielded as the ground-launched, short-range RPV for the Marine Corps, and as a RATO-launched, short-range RPV operating off of the Navy's battleships.

A realistic flight simulation of the Pioneer RPV for training system operators was desired. A 0.4-scale model of the Pioneer RPV was tested in the Wichita State University 7 by 10 foot wind tunnel to acquire its aerodynamic coefficients. A collateral benefit was the calculation of the Pioneer RPV's flight performance.

Graphs and tables of the stability and control derivatives necessary for a six-degree-of-freedom simulation are included in this thesis. Additionally, performance predictions were calculated using these newly acquired aerodynamic data and engine test data from the Naval Air Propulsion Center. Preliminary comparisons indicate good correlation between the wind tunnel based performance predictions and actual flight data.

20 Distribution/Availability of Abstract
[X] unclassified/unlimited [ ] same as report [ ] DTIC users

21 Abstract Security Classification: Unclassified

22a Name of Responsible Individual: Richard M. Howard
22b Telephone (*Include Area code*): (408) 646-2870
22c Office Symbol: AA/Ho

DD FORM 1473, 84 MAR 83 APR edition may be used until exhausted
All other editions are obsolete

security classification of this page: Unclassified

Approved for public release; distribution is unlimited.

A Wind Tunnel Study of the Pioneer Remotely Piloted Vehicle

by

Robert M. Bray
Captain, United States Marine Corps
B.S.E., Purdue University, 1982

Submitted in partial fulfillment of the requirements for
the degree of

MASTER OF SCIENCE IN AERONAUTICAL ENGINEERING

from the

NAVAL POSTGRADUATE SCHOOL
June 1991

ABSTRACT

Remotely Piloted Vehicles (RPVs) performed impressively well in the recent Gulf War. The Pioneer RPV has been fielded as the ground-launched, short-range RPV for the Marine Corps and as a RATO-launched, short-range RPV operating off of the Navy's battleships.

A realistic flight simulation of the Pioneer RPV for training system operators was desired. A 0.4-scale model of the Pioneer RPV was tested in the Wichita State University 7 by 10 foot wind tunnel to acquire its aerodynamic coefficients. A collateral benefit was the calculation of the Pioneer RPV's flight performance.

Graphs and tables of the stability and control derivatives necessary for a six-degree-of-freedom simulation are included in this thesis. Additionally, performance predictions were calculated using these newly acquired aerodynamic data and engine test data from the Naval Air Propulsion Center. Preliminary comparisons indicate good correlation between the wind tunnel based performance predictions and actual flight data.

TABLE OF CONTENTS

SYMBOLS AND NOMENCLATURE

Symbol	Definition
A	Aspect ratio
a	Lift curve slope or speed of sound (fps)
alpha	Angle of attack (degrees)
b	Wing span (ft)
beta	Sideslip
C	Test section cross-sectional area (ft^2)
$\bar{c}$	Wing chord (ft)
C_D	Drag Coefficient
C_{Do}	Drag coefficient at zero lift
c.g.	Center of gravity
C_L	Lift coefficient
C_l	Rolling moment coefficient
C_m	Pitching moment coefficient
C_n	Yawing moment coefficient
C_Y	Sideforce coefficient
D	Drag force (lbs)
d	Change in (i.e., $d\alpha$ is the change in angle of attack)
D_B	Buoyancy drag (lbs)
dC_p/dl	Longitudinal static pressure gradient coefficient
deg	Degrees
e	Oswald efficiency factor
F	Fahrenheit

Symbol	Definition
fpm	Feet per minute
fps	Feet per second
FQ&P	Flight Qualities and Performance
FS_{REF}	Horizontal distance from the wing leading edge to the desired fuselage station of the model's c.g. (ft)
FS_{tr}	Horizontal distance from the wing leading edge to the fuselage station of the model's trunnions (ft)
GCS	Ground Control Station
hp	Horsepower
I	Interference
k_1	Factor used in wing solid blockage correction [Ref. 6]
k_3	Factor used in wing solid blockage correction [Ref. 6]
L	Lift force (lbs)
l_t	Distance from the c.g. to the 1/4 chord of the tail (ft)
M	Pitching moment (ft-lbs)
MAC	Mean aerodynamic chord
NAVAIR	Naval Air Systems Command
P	Power (hp)
p	Roll rate (rad/sec)
pi	3.14159
PMTC	Pacific Missile Test Center
psf	Pounds per square foot
q	Dynamic pressure (lbs/ft^2) or pitching velocity (rad/sed) (deg/s or rad/sec)

Symbol	Definition
r	Yaw rate (rad/sec)
rad	Radian
RATO	Rocket Assisted Take-Off
R/C	Rate of climb (fpm)
RM	Rolling moment (ft-lbs)
RN	Reynolds number
rpm	Revolutions per minute
RPV	Remotely piloted vehicle
S	Wing area (ft^2)
S_t	Horizontal tail area (ft^2)
SFC	Specific fuel consumption (lb of fuel per unit power per unit time)
T	Tare, temperature or thrust force (lbs)
TED	Trailing edge down
TF	Wind-tunnel turbulence factor
t_{max}	Maximum fuselage thickness (ft)
UAV	Unmanned Air Vehicle
V	Velocity (knots, or fps for derivatives) or volume (ft^3)
V_H	Horizontal tail volume ratio ($S_t l_t/Sc$)
W	Weight (lbs)
WL_{REF}	Vertical distance from the tunnel floor to the desired water line of the model's c.g. (ft)
WL_{tr}	Vertical distance from the tunnel floor to the water line of the model's trunnions (ft)
Y	Sideforce (lbs)

Symbol	Definition
YM	Yawing moment (ft-lbs)
α	Angle of attack
αdot	Time rate of change of angle of attack (deg/s)
β	Sideslip
γ	Angle of Climb
δ	Factor used in streamline curvature corrections [Ref. 6]
ε	Dynamic pressure blockage correction factor or Downwash
ε_{SB}	Support and fairing solid blockage factor, ε_{SB} = frontal area/4C
η	Propeller efficiency or tail efficiency (q_{tail}/q)
λ_3	Factor used in buoyancy drag correction [Ref. 6]
μ	Viscosity (slugs/ft-sec)
π	3.14159
ρ	Air density (slugs/ft^3)
τ_1	Factor used in solid blockage correction [Ref. 6]
τ_2	Factor used in streamline curvature computation [Ref. 6]
ψ	Angle of yaw
^	Raised to a power

Subscripts

avail	Available
b	Body
c	Corrected data or calibrated
e	Equivalent
i	Indicated

Symbol	Definition
in	Induced
inv	Inverted
PS	Pitch strut
req	Required
SB	Solid blockage
SC	Streamline curvature
s	Sea level
t	Tail or true
tb	Total blockage
u	Uncorrected data
W	Wind axes data
w	Wing
WB	Wake blockage

ACKNOWLEDGMENTS

The wind-tunnel testing of the Pioneer RPV has been the highlight of my studies at the Naval Postgraduate School. My thesis advisor Dr. Richard Howard cheerfully gave of his expertise and valuable time. His keen interest and knowledge of experimental testing techniques has been a source of inspiration and guidance throughout this aerodynamic analysis.

Many thanks to Keith Bratberg, Steve Dean and the other members of the Simulation Support Branch at the Pacific Missile Test Center (PMTC). My enjoyment of this project is directly attributable to Keith Bratberg's confidence in my technical expertise, and the positive atmosphere he created throughout the test. My teamwork with Steve Dean was instrumental to the success of this project. He conceived the test plan and is currently writing the simulation.

A special thanks to Bonnie Johnson, Dave Phillis, Ben Hagnauer and Art Porter for their outstanding support and technical assistance throughout the wind-tunnel testing at Wichita State University.

I would also like to thank Captain Mark Ballinger of the Marine Aviation Detachment at PMTC for incorporating some of our performance predictions into his flight tests. Initial results indicate good correlation between actual flight and our predictions.

Finally, I would like to thank all the professors, secretaries and friends who contributed to my excellent education and enjoyment of my time at the Naval Postgraduate School. Catherine Keane was especially helpful in proofreading my thesis.

I. INTRODUCTION

Remotely Piloted Vehicles (RPVs) are a force multiplier on the modern battlefield. A Remotely Piloted Vehicle is an unmanned air vehicle capable of being controlled by a person from a distant location through a communications link. It is normally designed to be recoverable and can carry a wide variety of payloads. [Ref. 1:p. 309]

The Pioneer RPV has been fielded as the ground-launched, short-range RPV for the Marine Corps and as a RATO-launched, short-range RPV operating off of the Navy's battleships. Figure 1.1 shows a Pioneer RPV being launched from a pneumatic rail launcher.

Current Pioneer system training requires co-use by the internal pilot, external pilot, technicians and mechanics on an operational system. Training the pilots is a time-intensive, weather-dependent evolution requiring a complete system. Furthermore, reluctance to allow troubleshooting and parts replacement on an operational system hinders the training of the technicians and mechanics.

To provide responsive training that is cost effective and doesn't require the use of a flying RPV, the decision was made to develop a real-time simulation of the Pioneer RPV. This simulation will be integrated into the current Ground Control Station (GCS) for internal pilot training and coupled with a wide-screen three-dimensional display of a fully-functional Pioneer RPV for external pilot training. During a typical operation the internal pilot controls the air vehicle when out of visual range of the launch site from inside the GCS, and the external pilot launches and recovers the aircraft visually.

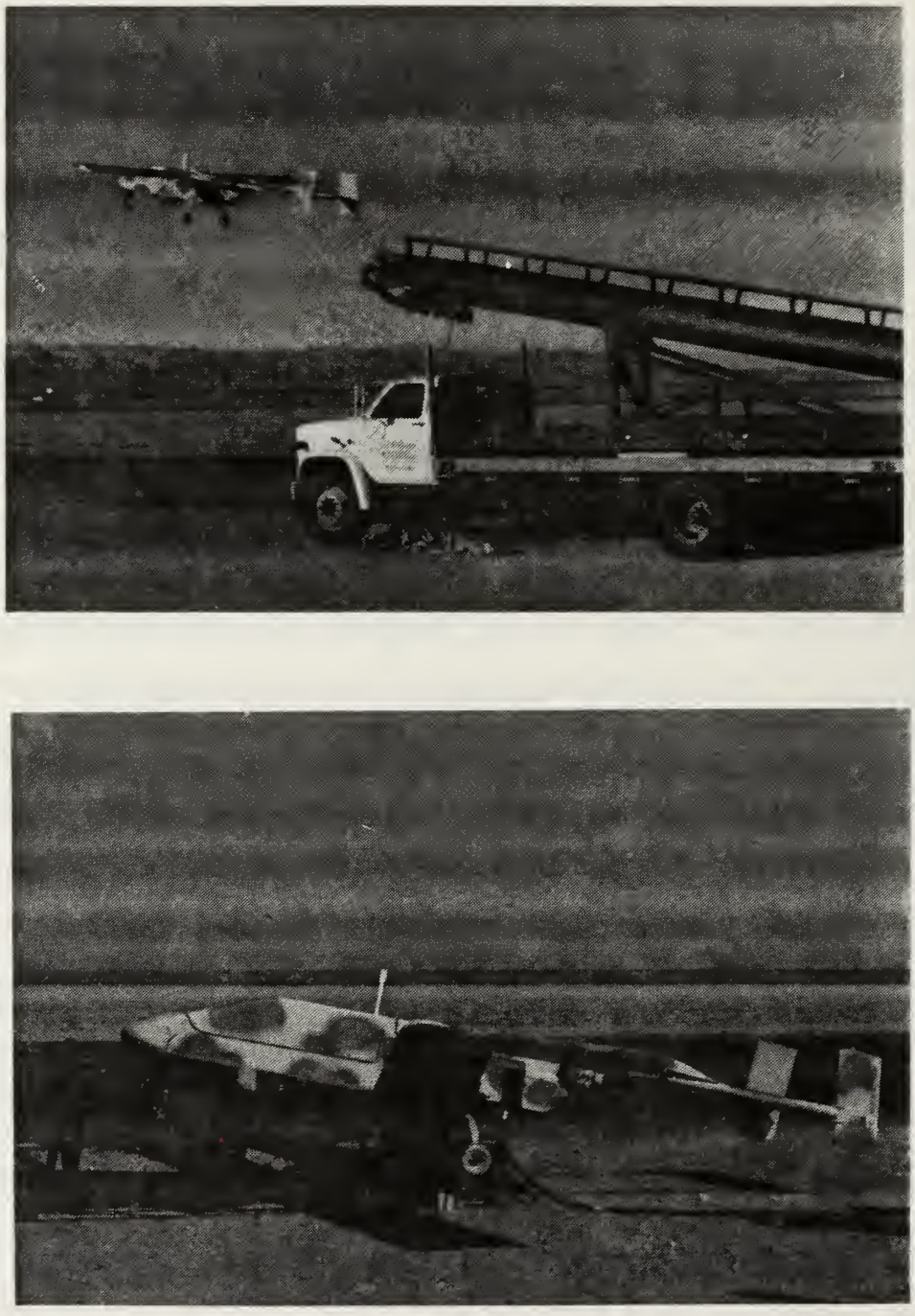

Figure 1.1 Pioneer RPV

PMA-205 at NAVAIR, responsible for RPV training, contracted the Cruise Missile Division, Simulation Support Branch (Code 1074) at Point Mugu Pacific Missile Test Center (PMTC) to develop a realistic simulation for training.

Adequate aerodynamic coefficients were unavailable. Wind-tunnel testing of a scaled Pioneer RPV was chosen as the best method to acquire the needed aerodynamic coefficients. Prior to this wind-tunnel test some limited aerodynamic analysis of the Pioneer RPV had been conducted at the Naval Postgraduate School including flight testing of a half-scale Pioneer RPV and a computational fluid dynamics analysis .

A 0.4-scale model of the Pioneer RPV was constructed and tested in the Wichita State University 7 by 10 foot wind tunnel. The purpose of these tests was to experimentally obtain the Pioneer RPV's aerodynamic coefficients for integration into a realistic flight simulation. The data acquired from the wind-tunnel test were also used to predict the Pioneer's performance. These performance predictions can be used to streamline the Flying Qualities and Performance (FQ&P) testing of the full-scale vehicle and improve mission profiles.

II. PIONEER SHORT RANGE REMOTELY PILOTED VEHICLE BACKGROUND

The importance of Remotely Piloted Vehicles was highlighted during the recent Gulf War. The Pioneer RPV provided real-time video surveillance and accurate gunfire adjustment throughout the theater of operation. Bunkers in Kuwait were hit with pinpoint accuracy using Pioneer RPVs as spotters for the battleship's 16-inch guns.

In Lebanon in December of 1983 Syrian artillery shot down two Navy fighter-bombers while they were avenging previous anti-aircraft attacks on Navy reconnaissance planes. The reconnaissance planes had been helping pick targets for the battleship New Jersey. The Navy figher-bomber's targets had been within range of the battleship's 2,600 pound shells, but given the threat to manned aircraft, accurate spotting was unavailable. RPVs would have provided unmanned, cost-effective, reliable spotting. Their smaller size and relatively low speeds provide the added advantage of often being undetected. [Ref. 2:p. 84]

In July 1985, then Secretary of the Navy, John Lehman, directed that a short-range Unmanned Air Vehicle (UAV) be procured using existing technology and off-the-shelf equipment to provide the Navy and Marine Corps effective reconnaissance, strike support, gunfire support, and battle damage assessment in a defended-threat environment. [Ref. 3:p. 4]

The Pioneer won the short-range RPV fly-off in December 1985 and was fielded as an interim short-range RPV [Ref. 3:p. 5]. The Pioneer RPV has been used for simultaneous training and development of tactics, test and evaluation

under operational conditions, and development of advanced operational concepts.

The Pioneer RPV system provides real-time video imagery from either daylight or forward-looking infrared sensors to the battlefield commander. Pioneer RPVs are used for real-time targeting, artillery and naval gunfire adjustment, and reconnaissance. The Pioneer observed every 16-inch round fired from the battleships in the Persian Gulf War [Ref. 4:p. 86].

The Marine Corps deployed three Pioneer RPV Companies to the Mideast, and Navy detachments flew Pioneers from the battleships Wisconsin and Missouri in the Persian Gulf. Pioneer RPVs logged over 1,000 hours during 307 flights in Operation Desert Storm. [Ref. 4:p. 86]

The flexibility of the Pioneer allows collection of information unavailable from satellites or tactical aircraft. Half of the missions were flown at night. Previously undetected Iraqi bunkers were found by Pioneers following Iraqi resupply trucks at night. [Ref. 5:p. 181]

The Pioneer RPV was so successful that an Iraqi artillery battalion abandoned their howitzers and waved surrender flags when they heard a Pioneer flying overhead. The Marines were still 20 kilometers away. [Ref. 5:p. 182]

During the advance on Kuwait City the Marine task force commander monitored RPV video imagery of the Iraqis' reaction to Marine armor, artillery and troop movements on a console in his command vehicle. General Al Gray, commandant of the Marine Corps, recently told Congress that the Marine Corps wanted more RPVs. He stated that the Pioneer RPV was extraordinarily successful. [Ref. 4:p. 86]

III. THE WIND-TUNNEL TEST

A. BACKGROUND

Aerodynamics deals with the atmospheric forces exerted on moving objects. Since the aerodynamic properties of a body are the same whether it moves through the air or whether the air moves over the body, wind tunnels have been used extensively for the analysis of aerodynamic flows over aircraft.

When a body moves through the air, forces arise that are due to the viscosity of the air, its inertia, its elasticity, and gravity. Since the model was not in free-flight, the forces due to gravity were included in the static weight tares and subtracted from the measured forces and moments.

The remaining important force ratios are the Reynolds number and Mach number defined as follows [Ref. 6:p. 7]:

$$\text{Reynolds number} = \frac{\text{Inertia force}}{\text{Viscous force}} = \frac{\rho}{\mu} V\bar{c} \qquad (3.1)$$

$$\text{Mach number} = \frac{\text{Inertia force}}{\text{Elastic force}} = \frac{V}{a}$$

If a model test has the same Reynolds and Mach numbers as the full scale vehicle, the flow about the model and the full scale vehicle will be identical. Under these conditions, the forces and moments developed by the model can be directly scaled to full scale. Unfortunately, it is impossible to match both the Reynolds number and the Mach number when testing a scale model in an unpressurized tunnel. In the low-speed flight regime of the Pioneer RPV, the

Reynolds number effects predominate, and matching the Mach number is not critical due to the small compressibility effects at its flight speeds. The test Reynolds number was set to match the full-scale flight Reynolds number.

B. MODEL

An 0.4-scale model of the Pioneer RPV (Figure 3.1) was designed and constructed at the Wichita State University engineering shop adjacent to the wind tunnel. The model was designed to withstand the maximum estimated loads at a dynamic pressure of 58 psf.

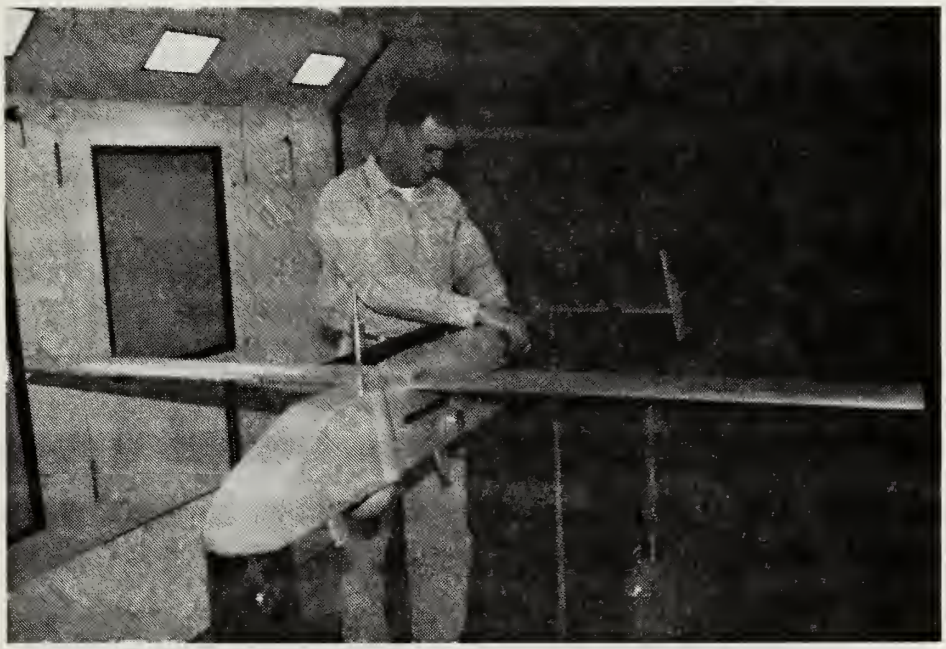

Figure 3.1 Pioneer Model in Test Section

Some of the items included on the model were the payload bubble, payload shield, rail launching mounts, cooling vents and directional antenna. The model was dimensioned from detailed drawings produced by Integrated Systems Analysts, Inc. (ISA) based on actual vehicle measurements, and from information provided by AAI, the Pioneer RPV prime contractor. The wing

incidence angle was set at 2° with respect to the fuselage water line (the water line parallels the lower fuselage surface) as specified by ISA and AAI. Further inquiries indicated that the actual wing incidence should have been set at 3° [Ref. 7]. This slight error from the full-scale vehicle accounts for a small but negligible shift in the lift and drag curves.

The wing and tail surfaces were milled from solid aluminum on a computer-controlled milling machine. The constant-chord, untwisted unswept wing with an aspect ratio of 9.4 had a uniform NACA 4415 airfoil section. The vertical and horizontal stabilizers were constant chord NACA 0012 airfoils. Control surface deflections were set using custom protractors as shown in Figure 3.2. Tail booms were made of steel tube for rigidity, and the remainder of the aircraft was a combination of aluminum, wood and composite materials.

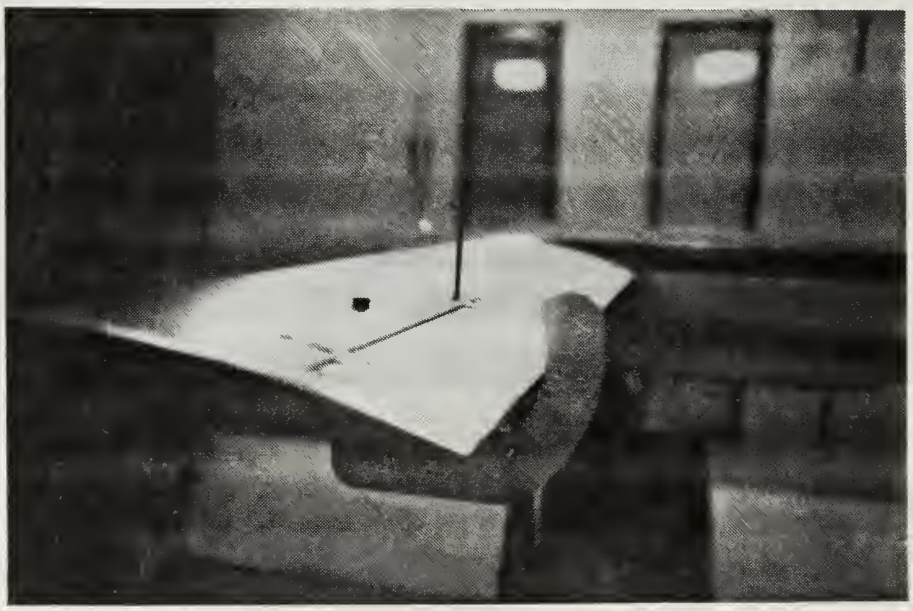

Figure 3.2 Custom Protractor for Setting Aileron Deflection

The model had a 10,000 rpm, water-cooled, variable-speed electric motor. Blade pitch was variable and set using a custom protractor. Engine rpm was variable from the control room. Power was stabilizing and increased the maximum lift of the aircraft. Power effects are not described in this thesis.

The model datum used for measurements during model construction and as a reference location for locating the desired model center of gravity and balance attachment points was set at the center of the wing leading-edge on the chord plane. The main support trunnions were located at 68% MAC. They were positioned this far aft to allow the pitch trunnion to be attached to the horizontal stabilizer.

C. BEECH MEMORIAL LOW-SPEED WIND TUNNEL

The Walter H. Beech Memorial Low-speed Wind Tunnel at Wichita State University, Wichita, Kansas, was used for the wind-tunnel testing. It is a low-speed, horizontal, closed-circuit, unpressurized wind tunnel with a 7 by 10 foot test section as shown in Figure 3.3. The test section is rectangular with triangular fillets in each corner. The contraction ratio is six to one. Velocity in the test section is variable up to 180 miles per hour. The tunnel airflow is generated by a 1,000 hp continuous duty (1,500 hp intermittent duty), 2300 volt, 3-phase, 60 Hz, wound-rotor induction motor that drives a four-blade, variable-pitch, 11-foot diameter fan. Accurate tunnel speed and background noise levels are obtained by using a combination of both propeller pitch and rpm controls. Wind-tunnel details are from the Facility Description of the 7 by 10 foot Walter H. Beech Memorial Low-speed Wind Tunnel by Davidson [Ref. 8].

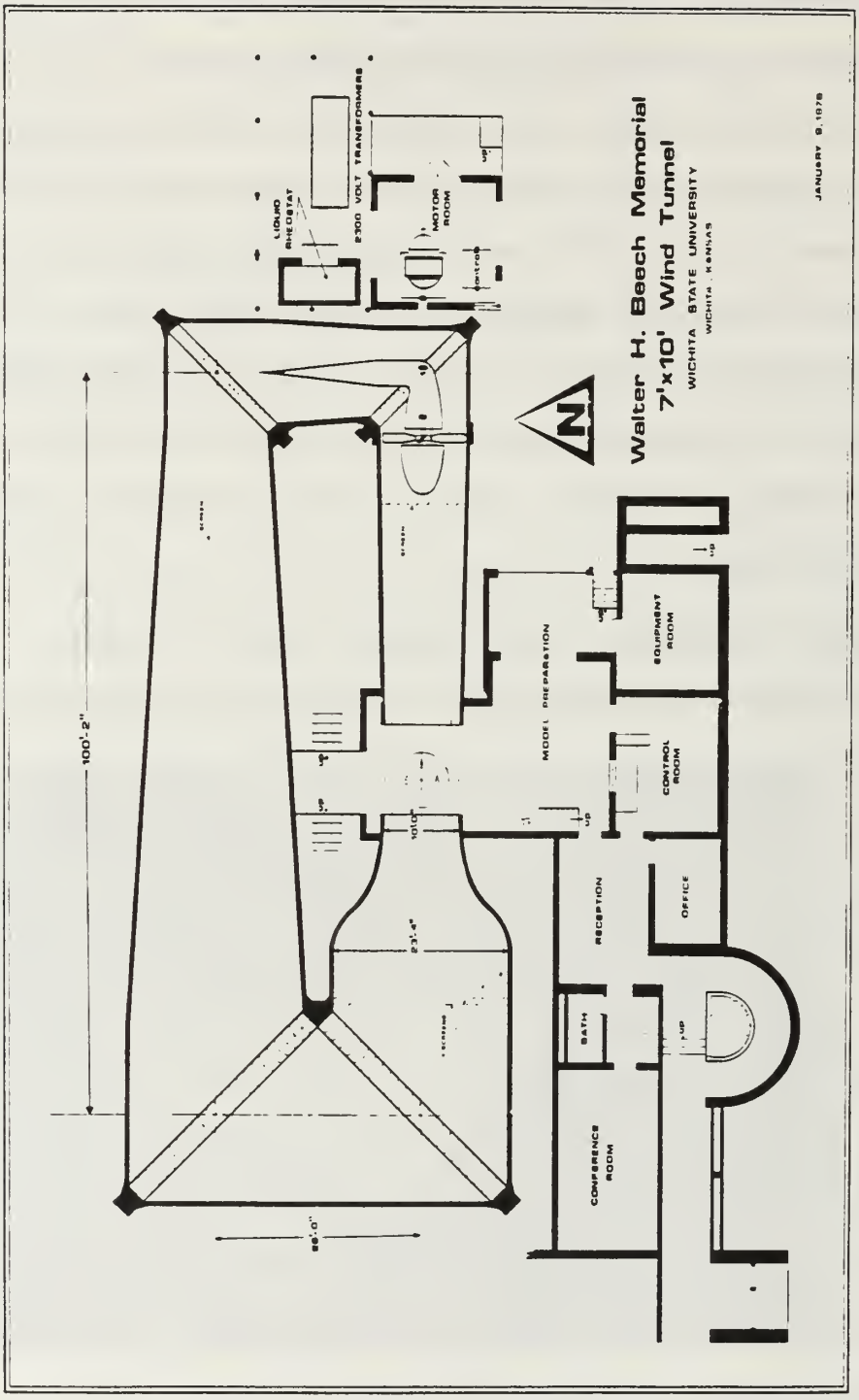

Figure 3.3 Wichita State 7 by 10 foot Wind Tunnel

The balance used was an external, six-component, truncated, pyramidal balance located below the test section turntable. This dynafocal type balance resolves the forces and moments about a virtual focus located on the tunnel center-line intersection with the support trunnion axis.

The two forward struts were attached to the wing trunnions and were partially shielded from the airflow by fairings attached to the test section turntable. The fairings were airfoil-shaped and remained aligned with the flow as the model was yawed. A diaphragm seal was not installed on the main supports to prevent flow through the fairings between the balance and the tunnel test section. Since no model changes were made that affected the flow near the forward strut attachments, it was assumed that the dynamic tares corrected for any misleading loads induced by the possible airflow through the fairings.

The aft strut was attached to the horizontal tail and was driven vertically to change the model angle of attack. Figure 3.4 shows the model in the test section. The balance set the model's angle of attack and angle of yaw and measured the six aerodynamic forces and moments. Angles were measured to the nearest 0.01 degree. Force and moment measuring units utilized full-range, strain gage load cells that were calibrated with motor-driven coarse weights of the individual force and moment units.

The balance output representing the three components of force and moment respectively (colloquially described as a six-component balance) was electrically sensed by strain gage load cells and remotely indicated in the control room. During the conduct of the test, a sequence of ten data samples were taken for each channel at a sample rate of ten per second and averaged

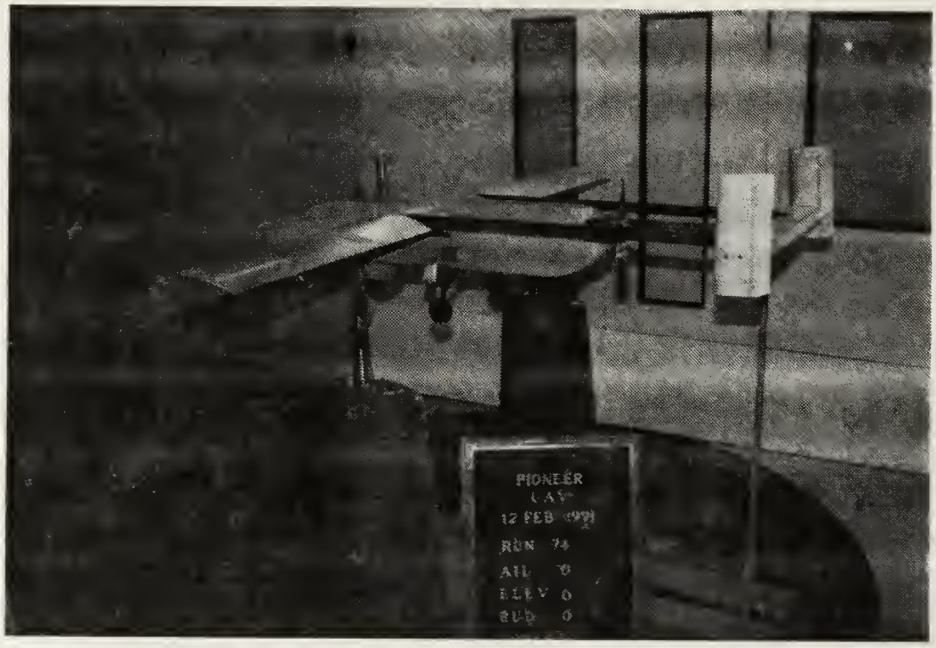

Figure 3.4 Pioneer Model in Test Section

for each test data point. Data was recorded on magnetic tape in both raw and coefficient form. Only two variables can be plotted during a run, such as lift coefficient versus angle of attack. The remaining variables can be plotted at the completion of the run. Force and moment measuring limits and resolutions are listed in Table 3.1.

TABLE 3.1 BALANCE LIMITS AND RESOLUTIONS

Component	Capacity	Resolution
Lift	±1,000 lbs.	0.20 lbs.
Drag	±250 lbs.	0.05 lbs.
Side Force	±500 lbs.	0.10 lbs.
Pitching Moment	±5,000 in-lbs.	2 in-lbs.
Rolling Moment	±5,000 in-lbs.	2 in-lbs.
Yawing Moment	±5,000 in-lbs.	2 in-lbs.

Force and moment coefficient resolutions for the 0.4-scale model at a q of 50 pounds per square foot are listed in Table 3.2, and calculated as follows:

$$\text{Force coefficient} = \frac{Force}{qS}$$

$$\text{Moment coefficient} = \frac{Moment}{qS(b \text{ or } \bar{c})}$$

TABLE 3.2 MOMENT RESOLUTION (q = 50 psf)

Coefficient	Resolution
C_L	0.0008
C_D	0.0002
C_Y	0.0004
C_m	0.0001
C_l	0.0001
C_n	0.0001

Dynamic pressure surveys showed a maximum variation across the test section area of ±0.75% at a dynamic pressure of 30 psf and of ±0.50% at a dynamic pressure of 60 psf [Ref. 8:p. 11].

A streamwise buoyancy survey showed a gradual decrease in static pressure. The static pressure difference along a model chord of one foot was 0.5% of dynamic pressure. [Ref. 8:p. 11]

The turbulence factor for the 7 by 10 foot test section was determined at three velocities using three different sizes of pressure turbulence spheres during a previous calibration. The turbulence factors were 1.42 at 61.6 fps, 1.26 at 137.9 fps and 1.015 at 262.5 fps. [Ref. 8:p. 11]

Using pressure turbulence spheres is a limited way to describe flow quality. Hot-wire anemometry is commonly used to measure turbulence intensity and frequency. The turbulence sphere method of defining an effective Reynolds number for this test should be sufficient since the test was conducted at flight Reynolds numbers where a turbulence factor of 1.13 will not significantly affect the test results for this low-airspeed non-laminar flow aircraft.

The turbulence factor was applied to the Reynolds numbers using the relationship

$$RN_{effective} = TF \times RN_{test}$$

with

$$TF = 1.42 - ((V - 61.6)(0.00202))$$

All wind-tunnel Reynolds numbers in this document have the turbulence factor applied. At the test dynamic pressure of 50 psf, the wind-tunnel velocity was about 205 fps yielding a turbulence factor of 1.13.

D. DATA REDUCTION

1. Overview

The forces and moments measured in a wind tunnel are not the same as those the aircraft experiences in free air. As stated earlier, moving the air over a still model produces the same aerodynamic forces as a model moving through the air. However, a longitudinal static pressure gradient results from boundary layer growth along the test section walls and the presence of the model and support apparatus in the closed test section. These extraneous forces that are produced were accounted for as described in this chapter. The wind-tunnel data reduction system corrected for the applicable boundary corrections as described by Rae and Pope [Ref. 6] and Ross [Ref. 9], applied

the model and balance corrections, and scaled the forces and moments to engineering units. The actual data reduction routine summarized below is described in detail in Aeronautical Report 80-1 [Ref. 10].

2. Balance Corrections

Initial wind off zeroes and static and dynamic tares for the model supports were subtracted. Tables of static and dynamic tares were input as functions of the appropriate angle (α or ψ). The interference effects were included in the dynamic tare values, and a correction for the balance interactions was applied.

3. Model Constants

The data reduction routine used the model constants shown in Figure 3.5. The model constants include areas and volumes of the model, boundary correction constants as described and calculated from Rae and Pope [Ref. 6], and the distances necessary to transfer the balance moments to the desired c.g. of the model. The three-dimensional boundary corrections for the Walter H. Beech Memorial 7 by 10 Foot low-speed wind tunnel are described in detail by Ross [Ref. 9].

4. Buoyancy Drag

Most wind tunnels with closed test sections have a static pressure that decreases in the streamwise direction due to the venturi effect caused by the thickening of the boundary layer in the test section. This static pressure gradient has a tendency to draw the model downstream, and hence it is called buoyancy drag. For the three-dimensional case the total correction (pressure

S_w 4.87 ft^2	$\bar{c}_w$ 0.722 ft	b_w 6.76 ft	AR_w 9.36	AR_t 5.74	e_w 0.913
V_b 0.811 ft^3	V_w 0.360 ft^3	t_{max} 0.880 ft	$\bar{V}_h$ 0.857	ε_{SB_s} .0064	τ_{1b} 0.860
λ_3 2.3	K_1 1.04	τ_{1w} 0.875	K_3 0.925	δ 0.118	TABLE 1
τ_{2w} 0.08	τ_{2t} 0.75	WL_{tr} 3.553 ft	FS_{tr} .4875 ft	WL_{ref} 3.331 ft	FS_{ref} .2225 ft

Figure 3.5 Model Constants Table

gradient and streamline squeezing effect) has been given by Glauert [Ref. 11] as

$$D_B = -\frac{\pi}{4}\lambda_3 (t_{\max})^3 \frac{dC_p}{dl} q_i$$

5. Solid Blockage

The presence of the model in the test section reduces the area through which the air must flow and by Bernoulli's equation the air velocity increases. This increase in air velocity over the model is called solid blockage. The solid blockage correction factors were computed for the wing and body as

$$\varepsilon_{SB_w} = k_1 \tau_1 V_w / C^{3/2}$$

and $$\varepsilon_{SB_b} = k_3 \tau_1 V_b / C^{3/2}$$

6. Wake Blockage

The wake behind the model has a lower velocity than the freestream. This causes the velocity outside the wake in a closed tunnel to be higher than the freestream velocity. This wake blockage causes an additional pressure gradient on the model. The wake blockage effect is accounted for as follows:

$$C_{L_u} = \frac{L}{q_i S}$$

$$C_{D_u} = \frac{D - D_B}{q_i S} - \text{dynamic tare}$$

$$\varepsilon_{WB} = \frac{S}{4C}(C_{D_u} - \frac{{C_{L_u}}^2}{\pi A_w})$$

7. Dynamic Pressure Correction

The dynamic pressure correction combines the effects of solid blockage of the wing and the body, the wake blockage calculated from the lift and drag of the model, and the solid blockage of the struts and fairings. The calculations are:

$$\varepsilon_{tb} = \varepsilon_{SB_w} + \varepsilon_{SB_b} + \varepsilon_{WB} + \varepsilon_{SB}$$

$$q_c = q_i(1 + \varepsilon_{tb})^2$$

8. Corrected Angles, Force and Moment Coefficients

The streamline curvature of the airflow over the model is affected by the walls and the support apparatus. Corrections as described in Reference 6 were applied to get the corrected angles, forces and moments. These values were calculated as follows:

$$C_{L_c} = \frac{L}{q_c S} - \text{dynamic tare}$$

$$\alpha_{in} = \delta(\frac{S}{C})(57.3)(1+\tau_{2_{wing}})C_{L_c}$$

$$\alpha_c = \alpha_i + \alpha_{in} + \alpha_{\text{flow angularity}}$$

$$C_{D_{in}} = \delta(\frac{S}{C})C_{L_c}{}^2$$

$$C_{D_c} = \frac{D - D_B}{q_c S} + C_{D_{in}} - \text{dynamic tare}$$

$$a = \frac{0.1 * AR}{2 + AR}$$

$$C_{m_{SC_w}} = 0.125\delta\tau_{2_{wing}}(\frac{S}{C})(57.3)a_w$$

$$C_{m_{SC_t}} = V_t\delta\tau_{2_{tail}}(\frac{S}{C})(57.3)C_{L_c}a_t$$

$$C_{m_c} = \frac{M}{q_c S\bar{c}} + C_{m_{SC_w}} + C_{m_{SC_t}} - \text{dynamic tare}$$

$$C_{l_c} = \frac{RM}{q_c Sb} - \text{dynamic tare}$$

$$C_{n_c} = \frac{YM}{q_c Sb} - \text{dynamic tare}$$

$$C_{Y_c} = \frac{Y}{q_c S} - \text{dynamic tare}$$

9. Forces and Moments Transferred to the Model Center of Gravity (Wind Axis)

The model reference center of gravity was set at 33% MAC on the thrust line for ease of comparison with prior analysis of the Pioneer RPV. The

current published c.g. range of the Pioneer RPV is from 32% to 33.5% MAC. The following coefficients are in the wind axis coordinate system of the tunnel test section, and were calculated as follows:

$$C_{L_w} = C_{L_c}$$

$$C_{D_w} = C_{D_c}$$

$$C_{m_w} = C_{m_c} + C_{L_c}\frac{(FS_{REF} - FS_{tr})}{\bar{c}} + C_{D_c}\frac{(WL_{tr} - WL_{REF})}{\bar{c}}$$

$$C_{l_w} = C_{l_c} + C_{Y_c}\frac{(WL_{tr} - WL_{REF})}{b}$$

$$C_{n_w} = C_{n_c} + C_{Y_c}\frac{(FS_{REF} - FS_{tr})}{b}$$

$$C_{Y_w} = C_{Y_c}$$

10. Forces and Moments Transferred to Stability Axis

All forces and moments referred to in this thesis are in the stability axis coordinate system. The stability axis rotates with the model in yaw, but not in pitch. Therefore lift is perpendicular to the relative wind or longitudinal centerline of the tunnel test section, and drag is perpendicular to the lift by definition and in line with the model centerline. The model coefficients in the stability axis coordinate system were calculated as follows:

$$C_L = C_{L_w}$$

$$C_D = C_{D_w}\cos\varphi - C_{Y_w}\sin\varphi$$

$$C_m = C_{m_w}\cos\varphi - C_{l_w}\sin\varphi\frac{b}{\bar{c}}$$

$$C_l = C_{l_w}\cos\varphi - C_{m_w}\sin\varphi\frac{\bar{c}}{b}$$

$$C_n = C_{n_W}$$

$$C_Y = C_{Y_W} \cos\varphi + C_{D_W} \sin\varphi$$

E. TARE AND INTERFERENCE

The balance struts that support the model affect the free air flow about the model and contribute drag. The effect of the model support system on the free air flow over the model is called interference, and the drag of the supports is called dynamic tare. The dynamic interference and drag of the support system were combined into the "dynamic tares" subtracted from the measured forces and moments.

Static weight tares are the non-aerodynamic forces and moments resulting both from the actual model center of gravity not being coincident with the balance moment center and from the weight of the model. Static weight tares were taken for each model configuration throughout the applicable pitch and yaw sweeps, and were subtracted from the balance data.

Dynamic tare drag was minimized by shielding the support struts. These aerodynamic shields did not shield the supports all the way to the wing, since their interference effects would increase and negate the potential gain from minimizing the tare drag.

Determining the tare and interference was essential to calculating the absolute magnitude of the forces and moments. Runs were made with and without dummy struts to determine the dynamic tare and interference of the model support system. Lacking a dummy pitch strut necessitated an additional two runs to determine the dynamic drag tare of the pitch strut. It was assumed

that the interference due to the pitch strut was negligible, since it could only affect a very small portion of the horizontal stabilizer.

The forward support strut dynamic tare and interference effects were found in two inverted runs. The runs were made inverted to allow removal of the lower pitch struts (top of the test section, but below the wing). First, a run was made with the model inverted and the dummy support struts installed as shown in Figure 3.6. The dummy support struts were soldered to the balance support struts at the wing trunnion attachment and floated free in the dummy shields attached to the ceiling of the test section, yielding

$$D_{meas} = D_{inv} + T_U + I_U + T_{PS} + T_L + I_L \tag{3.2}$$

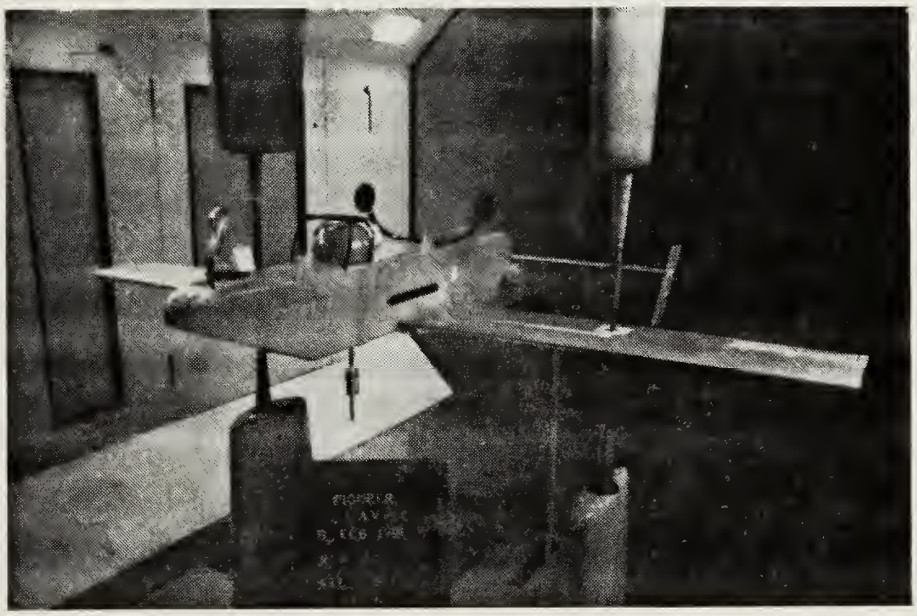

Figure 3.6 Model Inverted with Dummy Struts

Second, an inverted run was made without the dummy support struts below the wing (top of the test section) as shown in Figure 3.7, yielding

$$D_{meas} = D_{inv} + T_U + I_U + T_{PS} \tag{3.3}$$

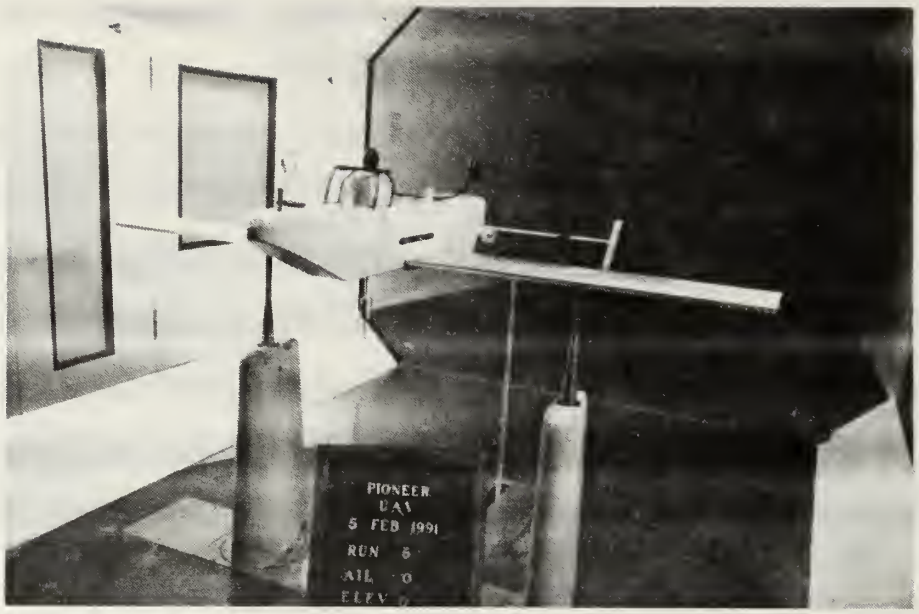

Figure 3.7 Model Inverted

Subtracting Equation 3.3 from Equation 3.2 yielded the dynamic tare and interference of the balance support struts.

To determine the dynamic drag tare of the pitch strut, two additional runs were made without the model. A run without the pitch strut was subtracted from a run with the pitch strut to yield the dynamic drag tare of the pitch strut throughout its range of motion.

Combining the above dynamic tare and interference effects yielded the "dynamic tares" that were subtracted from the measured forces and moments. These dynamic tares included the dynamic drag tare and interference of the wing struts, and the dynamic drag tare of the pitch strut. Dynamic tares were computed for the different model positions and applied by the data reduction routine.

F. DATA ACCURACY

1. Reynolds Effects

Many wind-tunnel tests are sensitive to Reynolds effects. Both the thickness of the boundary layer and the flow separation point are affected by the Reynolds number [Ref. 6:p. 447]. The variation of aerodynamic characteristics with Reynolds number is termed "scale effect" and is important in correlating wind-tunnel test data of scale models with the actual flight characteristics of the full-size aircraft. The two most important scale effects are drag and maximum lift [Ref. 12:p. 59]. Experimental data indicate that the section maximum lift coefficient will increase with increasing Reynolds number (from the higher energy turbulent boundary layer) and the section drag coefficient will decrease.

The test Reynolds number (Equation 3.1) varied primarily with the test section velocity. The characteristic length was fixed as the model's wing chord, and the kinematic viscosity, ρ/μ, subject to local ambient conditions, varied only slightly between runs.

Scale effects were minimized by carefully matching the test Reynolds number to the flight Reynolds number by increasing the test section velocity enough to compensate for the smaller 0.4-scale wing chord. Full-scale Reynolds numbers of the Pioneer in flight at 65 knots are 1.35 million and 0.98 million respectively at sea level and at 10,000 ft on a standard day. All unpowered wind-tunnel tests were run at a dynamic pressure of 50 pounds per square foot, resulting in a nominal effective Reynolds number of 1.06 million, a number within the range of full-scale flight Reynolds numbers.

Figure 3.8 compares the lift and drag at q values ranging from 10 to 50 pounds per square foot. Relatively small changes in the measured forces and moments were observed down to a q of 20 psf. The drag increased with lower Reynolds numbers as expected, but the total lift coefficient increased at high angles of attack as the Reynolds number decreased. This lift coefficient was for the entire Pioneer RPV and not just for an airfoil section lift coefficient. One possible explanation for the higher maximum lift coefficient at Reynolds numbers below 1 million is that the Pioneer RPV wing uses an NACA 4415 airfoil, which can exhibit an increased maximum lift coefficient below a Reynolds number of 1 million. A two-dimensional wind-tunnel test of the NACA 4415 airfoil in the NACA Low Turbulence Tunnel in 1945 showed an increase in maximum lift coefficient at a Reynolds number of 700,000 when compared to lift coefficients at Reynolds numbers from 1 million to 2 million [Ref. 13:p. A-426].

The q comparison was done to check for any unexpectedly large Reynolds effects. The flow transition point of the struts was assumed fixed both due to sharp corners near their leading edges, and the surface roughness of their cross-hatched sides. The data reduction of all runs in the q comparison used the dynamic tares for a q of 50 psf.

2. Balance Aerodynamic Alignment

Ideally the airflow would be parallel to the test section centerline. To check for any downflow the model was tested both upright and inverted with dummy struts attached. The data from both runs were plotted in Figure 3.9 with the negative lift plotted as though it was positive. The variation in the flow

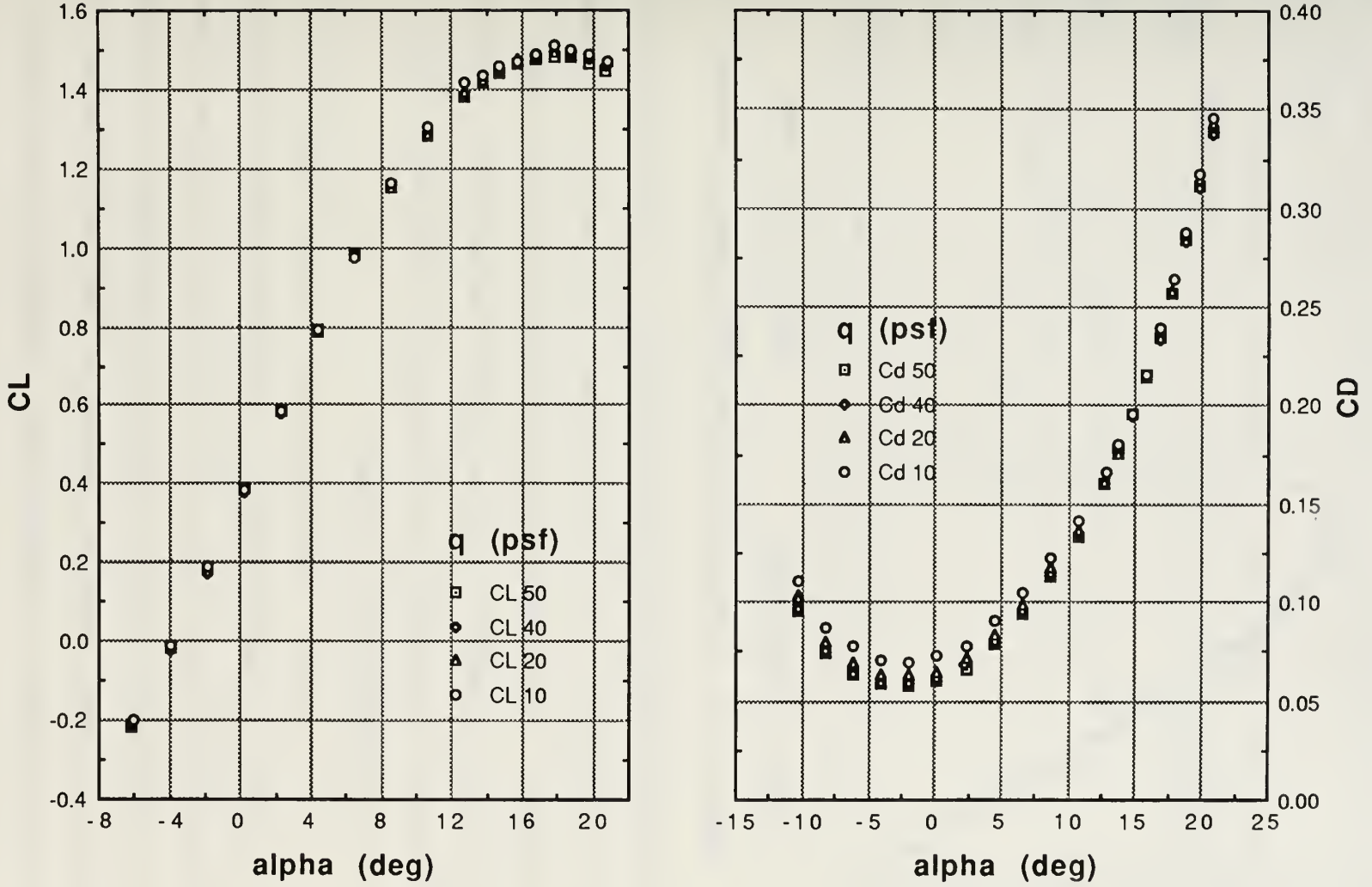

Figure 3.8 Dynamic Pressure Effects

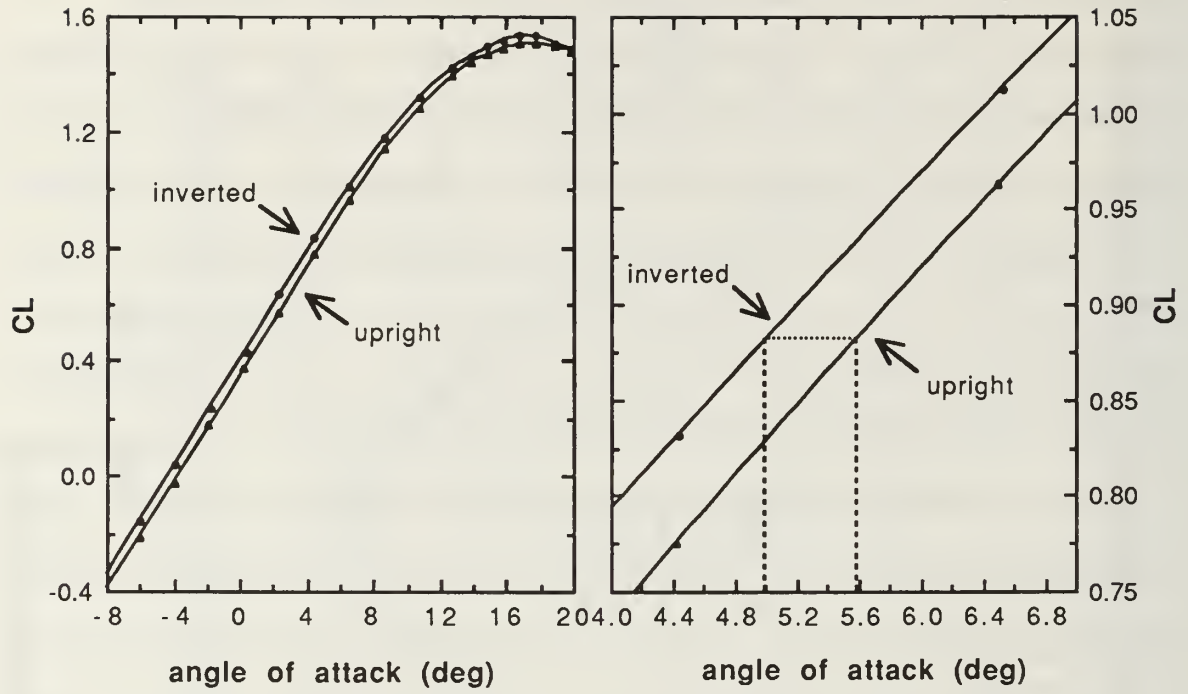

Figure 3.9 Tunnel Downflow (With Image System)

is half the angle difference between the two curves. As shown by Figure 3.9 there was a downflow of less than 0.3 degrees. The crossflow was measured as 0.2 degrees. The downflow was not corrected for in the final results. The crossflow was corrected for by subtracting the values recorded at zero sideslip for the sideforce, yaw moment and roll moment from the measured values.

3. Repeatability and Accuracy

Runs in identical configurations were repeated throughout the test, both sequentially without any changes, to check the reproducible accuracy of the balance and the speed control, and with several runs between repeats to verify the reproducible accuracy of setting the control surfaces. No significant variations were noted. Periodically the wind-off zeros were rechecked at the end of a run, exhibiting no indication of drift. The first data point of each run

was repeated at the end of the run to test for drift or hysteresis. No significant discrepancies were noted.

The baseline run was computed by hand from the raw data to verify that all corrections were being applied correctly by the data reduction system.

IV. STABILITY AND CONTROL

A. INTRODUCTION

Aircraft stability, control and handling qualities drive an aircraft's design process as much as the desired performance. Location of the center of gravity, control surface sizing and location, and control input sensitivity play key roles in determining the responsiveness and stability of an aircraft.

The static stability and control described in this thesis is for the Pioneer RPV air vehicle alone. Normal operation of the Pioneer RPV involves an on-board, computer-controlled autopilot driving the control surfaces. As demonstrated by current generation fighters, computer control can turn an unstable aircraft into a highly maneuverable stable aircraft, or similarly, a poorly-designed, or slowly-responding autopilot can degrade an aircraft's handling qualities.

If an aircraft in steady flight (resultant forces and moments about the aircraft's center of gravity are zero) tends to return to its original state when disturbed by an air gust or control input, that aircraft possesses static stability. Controls must be adequate to move the aircraft into and maintain desired flight conditions (angles of attack, airspeeds or bank angles). Handling qualities are a subjective assessment of the way an aircraft responds to control inputs.

B. BACKGROUND

The Pioneer RPV is currently designated as the short-range, remotely-piloted air vehicle for both the Navy and Marine Corps. PMA-205 at NAVAIR contracted the Simulation Support Branch (Code 1074), Cruise Missile Division

at the Point Mugu Pacific Missile Test Center (PMTC) to develop a real-time flight simulation for training Pioneer RPV system operators. This flight simulation will be integrated into and incorporate the Ground Control Station (GCS) for internal pilot training. External pilot training will be visually based utilizing a large screen display driven by a Hewlett-Packard graphics work station. Future enhancements including digitized terrain features will permit training of the payload operators. The entire simulation for training will be in real time.

Adequate aerodynamic coefficients describing the Pioneer's flight characteristics were unavailable. The wind-tunnel testing was conceived and structured to acquire the necessary stability-and-control coefficients to produce this real-time simulation. This wind-tunnel test additionally provided the information necessary for flight performance predictions. Performance predictions in Chapter V can be used as a baseline for formulating future flight test plans. Since the shapes of the Pioneer RPV's performance curves are now defined, selective flight testing can be used to verify and shift the predicted performance curves to agree with actual flight test data. This can significantly reduce the number of test flights necessary. An accurate airspeed calibration must also be performed on the Pioneer RPV to correctly correlate flight speeds with predicted speeds.

C. COORDINATE SYSTEM

Aircraft stability and control are governed by forces and moments acting about the aircraft's center of gravity. These wind-tunnel test results are in the aircraft stability axis coordinate system as shown in Figure 4.1. The stability axis is centered at the aircraft's center of gravity. The stability axis rotates with

the aircraft in yaw, but not in pitch. All angles of attack in this thesis are referenced to the fuselage waterline, which is parallel to the fuselage lower surface. The center of gravity was set at 33% MAC on the thrust line, unless otherwise stated. The center of gravity is the point through which the entire weight of the aircraft acts.

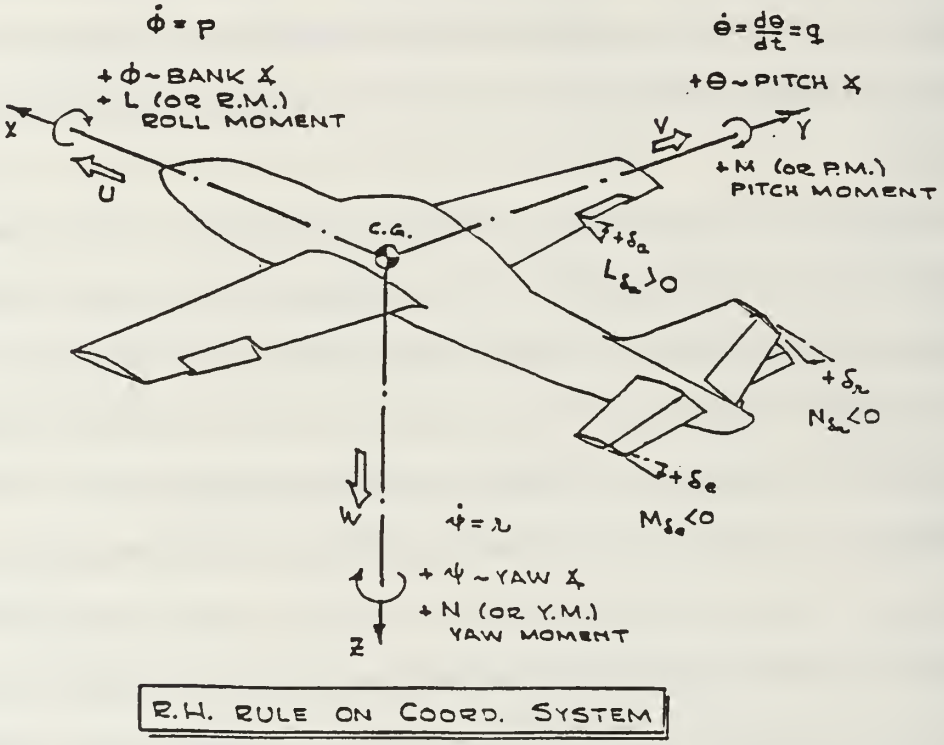

Figure 4.1 Coordinate System

D. AIRCRAFT DIMENSIONS AND STABILITY AND CONTROL COEFFICIENTS

The option 2, large-tail Pioneer RPV (Figure 3.1) was tested at an effective Reynolds number of 1.06 million, within the range of full-scale flight Reynolds numbers. Physical dimensions of the Pioneer RPV as tested are listed in Table 4.1. The model was pitched and yawed throughout its full flight range of motion. Control surfaces were set using custom protractors as shown in Figure 3.2. All

single-value flight coefficients are for 6 degrees angle of attack (66 knots cruise speed for a 420-pound Pioneer RPV), with the c.g. located at 33% MAC on the thrust line. The stability and control coefficients obtained from the wind-tunnel testing of the Pioneer RPV model indicate that the aircraft should have good stability and control characteristics throughout its flight regime.

TABLE 4.1 PIONEER DIMENSIONS AS TESTED

Wing	
Area	30.42 ft^2
Span	16.90 ft
Aspect Ratio	9.36
Mean Aerodynamic Chord	1.80 ft
Airfoil	NACA 4415
Incidence	2.0 deg
Aileron Deflection	±20 deg
Horizontal Stabilizer	
Area	6.07 ft^2
Span	6.07 ft
Aspect Ratio	6.07
Chord	1.00 ft
Airfoil	NACA 0012
Incidence	-3 deg
Elevator Deflection	±20 deg
Vertical Stabilizers	
Area	2.17 ft^2
Span	2.17 ft
Aspect Ratio	2.17
Chord	1.00 ft
Airfoil	NACA 0012
Rudder Deflection	±20 deg

Nondimensional coefficients in the stability axis coordinate system were used to describe the Pioneer RPV's flight characteristics. Nondimensional force coefficients are defined by dividing the force by the dynamic pressure (q) and the wing area (S). Since moments include a length (moment arm), they are further divided by a characteristic length. The MAC ($\bar{c}$) of the wing is used for

calculating the pitching moment coefficient, and the wing span (b) is used for calculating the yawing and rolling moment coefficients. For example, the pitching moment coefficient is defined as

$$C_m = \frac{M}{qS\bar{c}}$$

Responses of stability coefficients to angular orientations (i.e., angle of attack) or control surface deflections are indicated by subscripts. C_{m_α} indicates a change in pitching moment due to angle of attack; $C_{m_{\delta_e}}$ is the pitching moment response to an elevator deflection. [Ref. 14:p. 410]

Responses of stability coefficients to angular rates are standardized as partial derivatives with respect to the angular rate, a characteristic length and the freestream velocity to keep them nondimensional [Ref. 15:pp. 250-251]. For example, the change in the pitching moment due to pitch rate is defined as

$$C_{m_q} = \frac{\partial C_m}{\partial(\frac{q\bar{c}}{2V})}$$

Changes in force and moment coefficients with Mach number were not investigated for the Pioneer RPV's low-speed (incompressible) flight regime.

Table 4.2 lists the Pioneer RPV's stability and control coefficients at 6 degrees angle of attack for an option 2, large-tail Pioneer RPV. The methods used to obtain these coefficients are described in detail in this chapter.

E. LONGITUDINAL STATIC STABILITY AND CONTROL

Longitudinal stability implies that the pitching moment about the aircraft's center of gravity is zero and will return to zero when disturbed. For a given aircraft configuration, an aircraft's pitching moment is normally a function of

TABLE 4.2 PIONEER RPV STABILITY AND CONTROL COEFFICIENTS

Name	Description	Wind Tunnel
S	surface area of wing, ft^2	30.42
b	wingspan, ft	16.90
c	chord, ft	1.80
A	wing aspect ratio	9.4
W	gross weight, lbs_f	420
α	angle of attack (fuselage), deg	6
V	velocity, knots TAS	66
C.G.	33% MAC on thrust line	
CL	lift coefficient	.945
CL_0	lift coefficient at $\alpha = 0$	.385
CD	drag coefficient	.090
CD_0	drag coefficient at $\alpha = 0$	.060
CL_α	lift curve slope	4.78
CD_α	drag curve slope	.430
Cm	pitch moment	.012
Cm_0	pitch moment at $\alpha = 0$	.194
Cm_α	pitch moment due to angle of attack	-2.12
CL_q	lift due to pitch rate	8.05
Cm_q	pitch moment due to pitch rate	-36.6
$CL_{\alpha dot}$	lift due to angle of attack rate	2.42
$Cm_{\alpha dot}$	pitch moment due to angle of attack rate	-11.0
Cy_β	side force due to sideslip	-.819
Cl_β	dihedral effect	-.023
Cl_p	roll damping	-.450
Cl_r	roll due to yaw rate	.265
Cn_β	weathercock stability	.109
Cn_p	adverse yaw	-.110
Cn_r	yaw damping	-.200
$CL_{\delta e}$	lift due to elevator	.401
$CD_{\delta e}$	drag due to elevator	.0180
$Cm_{\delta e}$	pitch control power	-1.76
$Cl_{\delta a}$	roll control power	.161
$Cn_{\delta a}$	aileron adverse yaw	-.0200
$Cn_{\delta r}$	yaw control power	-.0917
$Cy_{\delta r}$	sideforce due to rudder	.191
$Cl_{\delta r}$	roll due to rudder	-.00229

All coefficients are per radian.

angle of attack. If the pitching moment decreases with increasing angle of attack, the aircraft will have positive static stability.

1. Effect of Elevator Deflection

Elevator deflection is used to change the pitching moment about the aircraft's center of gravity to enable trimmed flight at different angles of attack (flight speed). Figure 4.2 shows the Pioneer RPV's pitching moment coefficient versus

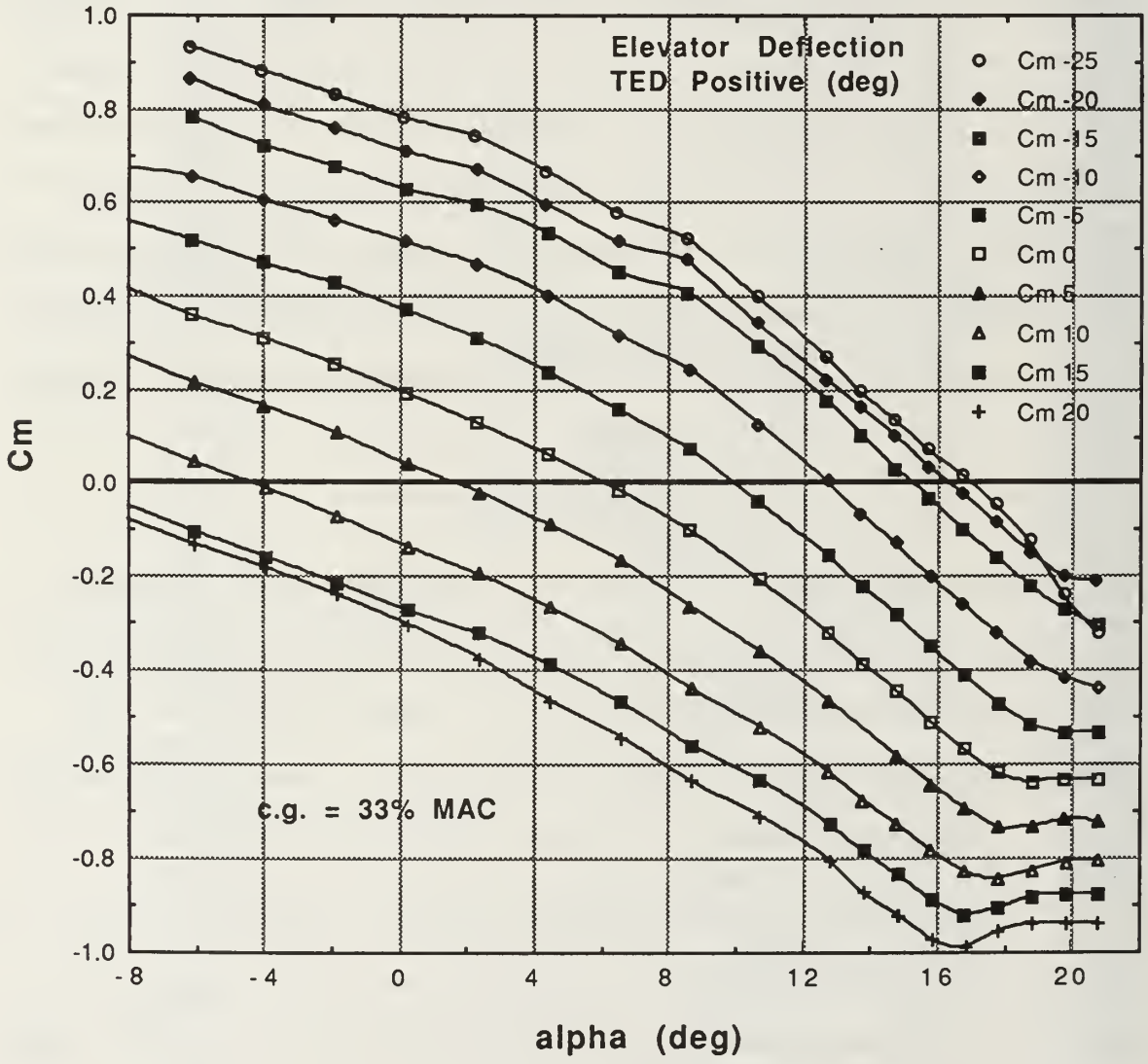

Figure 4.2 Pitching Moment Coefficient with Elevator Deflection

angle of attack for elevator deflections from 25 degrees trailing-edge up (-25°) to 20 degrees down (20°). Elevator deflection shifts the pitching moment curve with minimal changes in slope at moderate angles of attack.

Figure 4.3 shows the change in pitching moment coefficient with elevator deflection at 6.5 degrees angle of attack. The Pioneer's elevator produces an average change in pitching moment coefficient with elevator deflection of -0.0308 per degree of elevator deflection up to 15 degrees of elevator deflection. From 15 to 25 degrees of elevator deflection, the average change in pitching moment is -0.0128 per degree elevator deflection.

The elevator deflection required to trim the Pioneer RPV at a desired angle of attack can be found by interpolating between the curves in Figure 4.2 at the desired angle of attack on the C_m equals zero line. The aircraft has positive static stability at the angles of attack where the curves exhibit a negative slope. Note that the aircraft is trimmed ($C_m = 0$) at only one aircraft angle of attack for a given elevator deflection. Deflecting the elevator up (negative change in elevator deflection) trims the aircraft at a higher angle of attack (lower airspeed). The Pioneer RPV with zero elevator deflection has a trimmed angle of attack of 6.2 degrees (65.3 knots for a 420 lb Pioneer), which corresponds to a lift coefficient of 0.96.

Figure 4.4 shows the Pioneer RPV's lift coefficient versus angle of attack for elevator deflections from 25 degrees up (-25°) to 20 degrees down (20°). Elevator deflection shifts the lift curve slope vertically by an amount corresponding to the lift created by the deflected elevator. The maximum lift of a trimmed aircraft is less than the lift of the same aircraft at the same angle of attack with no elevator deflection. The elevator deflection necessary to trim

the aircraft at high angles of attack produces a download which reduces the aircraft's total lift. Figure 4.5 shows the trimmed aircraft's angle of attack and lift coefficient versus elevator deflection. Construction of the Pioneer RPV's trimmed lift curve will be described in the performance chapter.

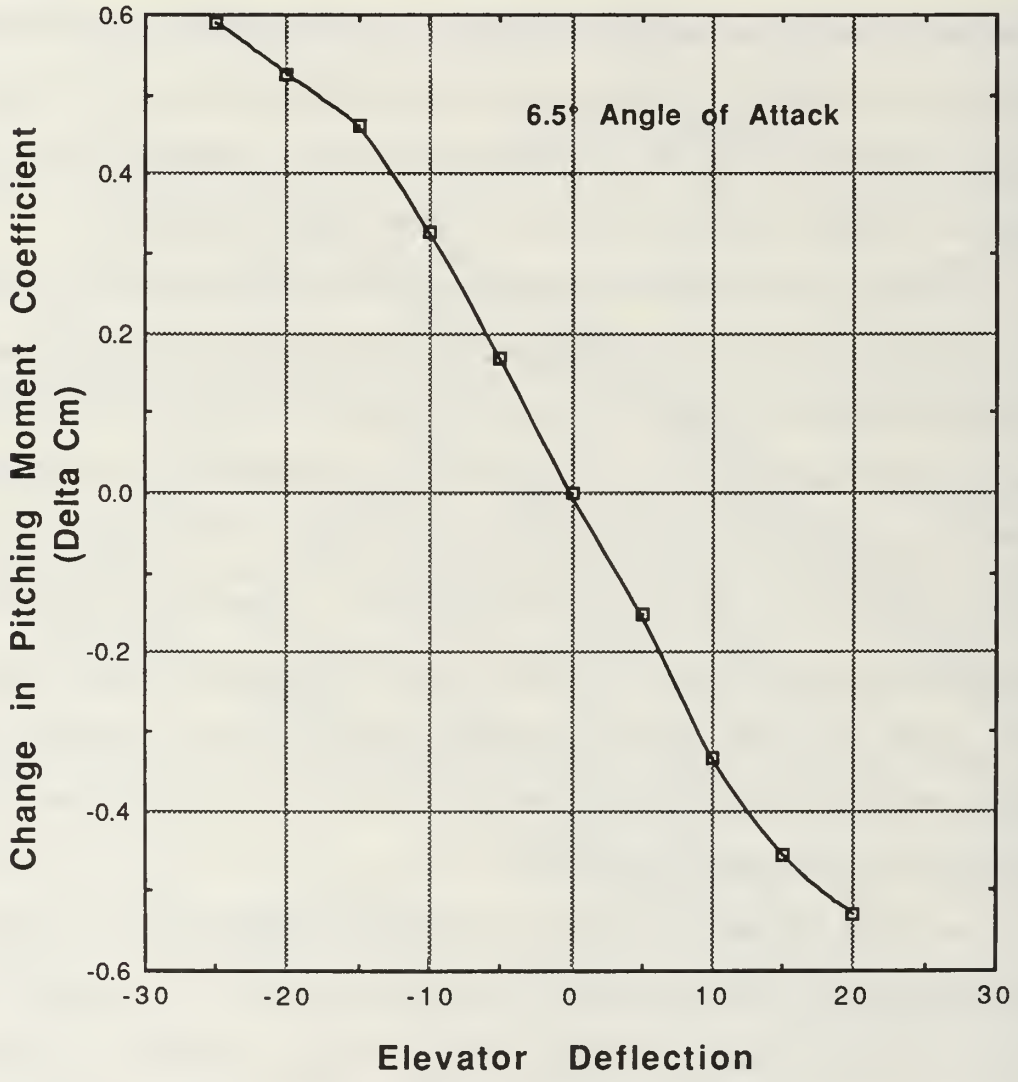

Figure 4.3 Change in Pitching Moment Coefficient with Elevator Deflection

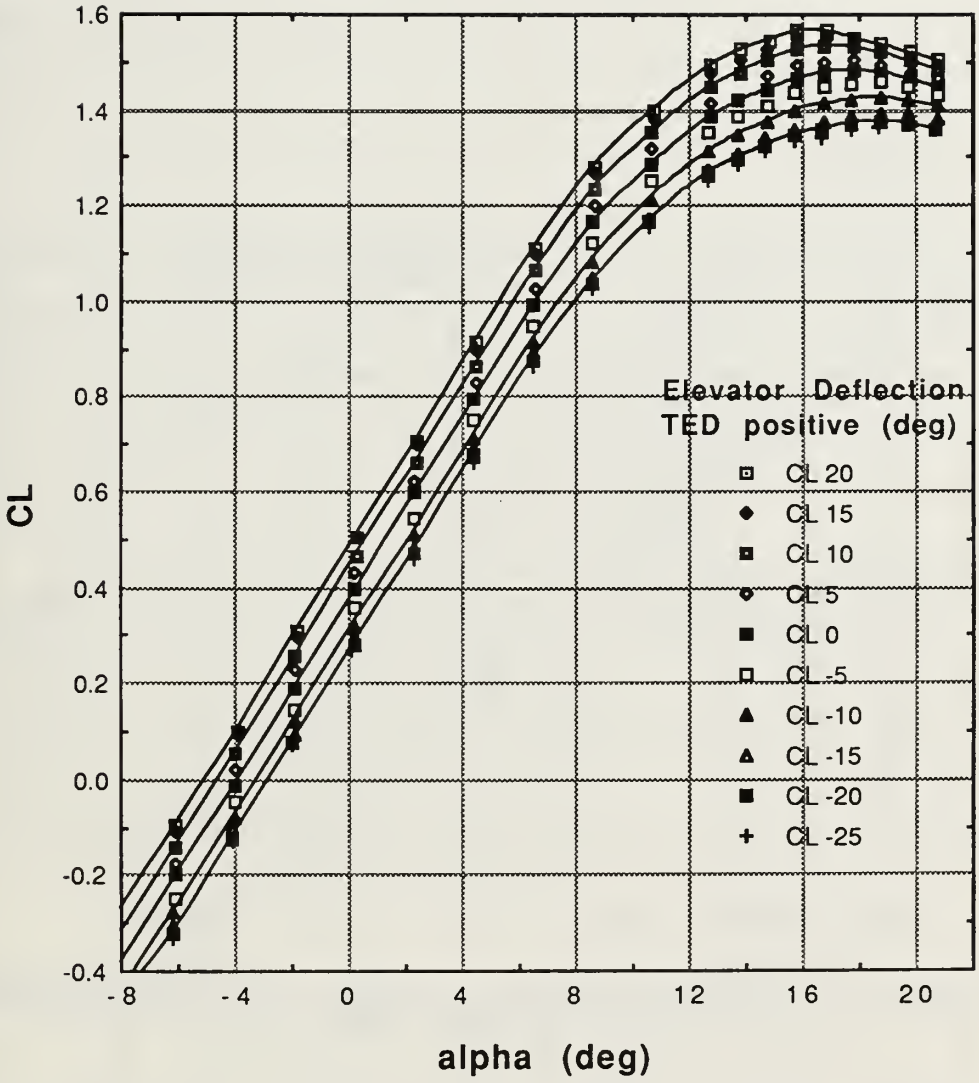

Figure 4.4 Change in Lift Coefficient with Elevator Deflection

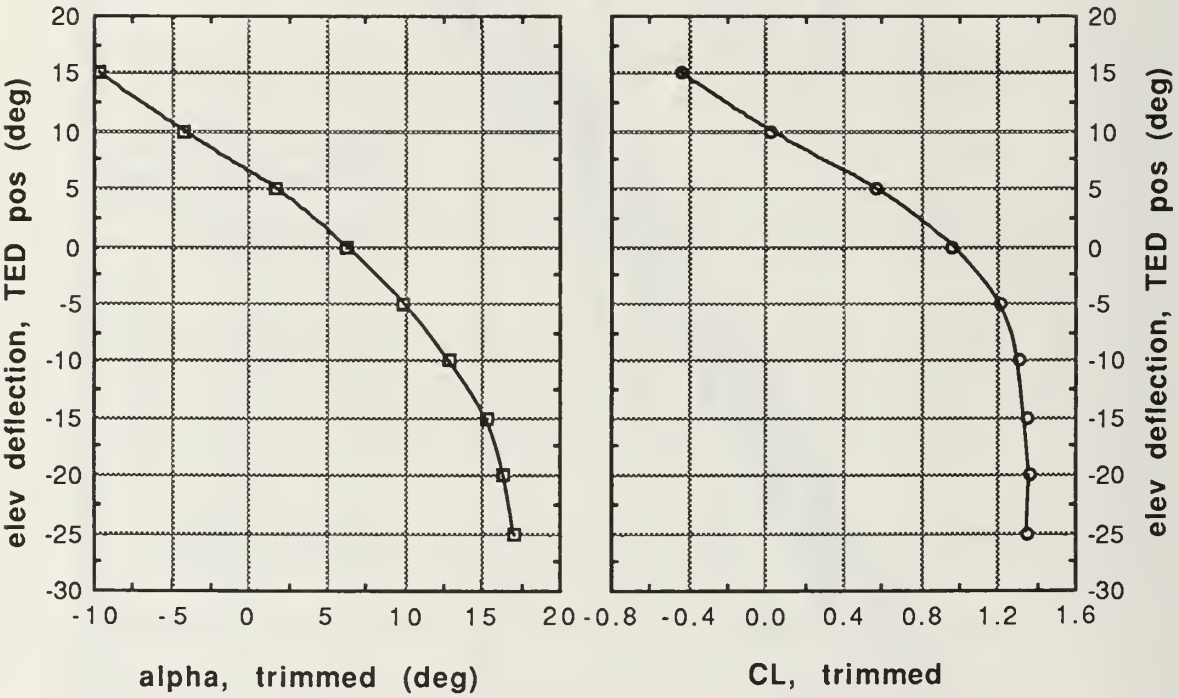

Figure 4.5 Trimmed Angle of Attack and Lift Coefficient versus Elevator Deflection

An exploded view of the change in lift coefficient due to elevator deflection is shown in Figure 4.6. Table 4.3 lists the Pioneer RPV's total lift coefficient for elevator deflections from -25° to 20°. The change in lift coefficient with elevator deflection is listed in Table 4.4.

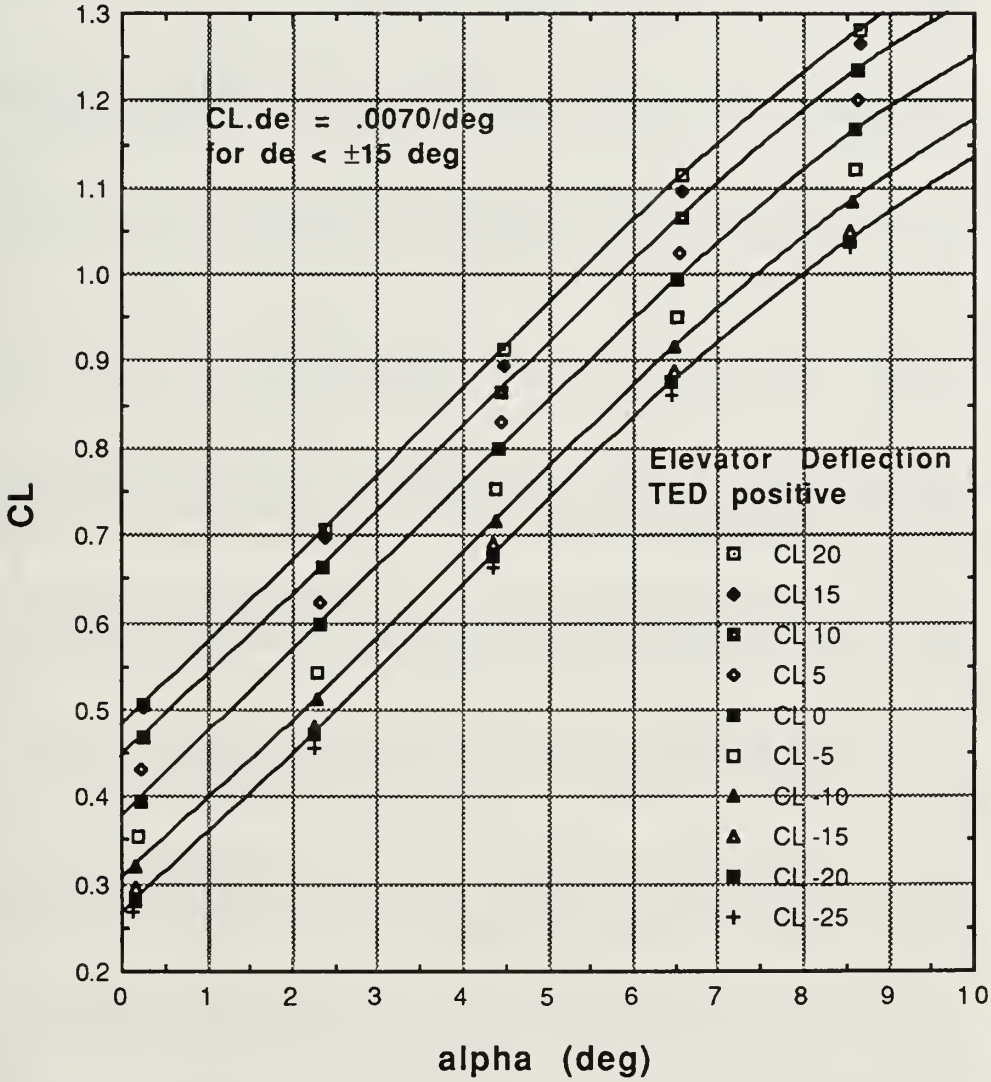

Figure 4.6 Change in Lift Coefficient with Elevator Deflection

TABLE 4.3 TOTAL LIFT COEFFICIENT

α deg	δe=0	δe=20	δe=15	δe=10	δe=5	δe=-5	δe=-10	δe=-15	δe=-20	δe=-25
-7	-0.294	-0.194	-0.202	-0.236	-0.269	-0.330	-0.351	-0.369	-0.382	-0.385
-6	-0.202	-0.101	-0.108	-0.143	-0.176	-0.240	-0.262	-0.281	-0.295	-0.298
-5	-0.107	-0.006	-0.012	-0.047	-0.080	-0.146	-0.171	-0.190	-0.205	-0.208
-4	-0.010	0.092	0.086	0.051	0.018	-0.051	-0.077	-0.097	-0.112	-0.117
-3	0.088	0.191	0.185	0.150	0.117	0.046	0.019	-0.002	-0.018	-0.023
-2	0.187	0.291	0.284	0.250	0.216	0.144	0.115	0.093	0.077	0.071
-1	0.286	0.392	0.384	0.350	0.316	0.242	0.212	0.189	0.173	0.166
0	0.385	0.492	0.484	0.450	0.415	0.340	0.309	0.285	0.270	0.261
1	0.483	0.591	0.582	0.549	0.514	0.438	0.406	0.381	0.365	0.356
2	0.580	0.689	0.679	0.646	0.611	0.534	0.501	0.475	0.460	0.450
3	0.674	0.785	0.774	0.741	0.706	0.629	0.595	0.567	0.553	0.542
4	0.766	0.878	0.866	0.834	0.798	0.721	0.686	0.658	0.644	0.632
5	0.855	0.968	0.955	0.923	0.887	0.811	0.775	0.745	0.733	0.719
6	0.940	1.054	1.040	1.008	0.973	0.897	0.860	0.830	0.818	0.803
7	1.022	1.135	1.121	1.090	1.054	0.980	0.942	0.911	0.899	0.884
8	1.098	1.212	1.196	1.166	1.131	1.057	1.019	0.987	0.976	0.960
9	1.170	1.282	1.266	1.237	1.202	1.130	1.092	1.059	1.048	1.032
10	1.235	1.347	1.330	1.302	1.267	1.197	1.159	1.125	1.115	1.099
11	1.295	1.404	1.387	1.360	1.326	1.258	1.220	1.185	1.175	1.159
12	1.347	1.455	1.437	1.411	1.377	1.312	1.274	1.240	1.229	1.214
13	1.392	1.497	1.478	1.455	1.422	1.359	1.322	1.287	1.276	1.262
14	1.430	1.530	1.512	1.490	1.458	1.398	1.362	1.326	1.316	1.302
15	1.458	1.554	1.536	1.516	1.485	1.429	1.393	1.358	1.347	1.334
16	1.478	1.568	1.551	1.533	1.503	1.451	1.416	1.381	1.369	1.358
17	1.488	1.572	1.556	1.541	1.512	1.463	1.430	1.396	1.382	1.373

TABLE 4.4 CHANGE IN LIFT COEFFICIENT WITH ELEVATOR DEFLECTION

α deg	δe=0	δe=20	δe=15	δe=10	δe=5	δe=-5	δe=-10	δe=-15	δe=-20	δe=-25
-7	0	0.100	0.093	0.058	0.025	-0.036	-0.057	-0.075	-0.088	-0.091
-6	0	0.101	0.093	0.059	0.026	-0.038	-0.061	-0.079	-0.093	-0.096
-5	0	0.101	0.094	0.060	0.027	-0.040	-0.064	-0.083	-0.098	-0.102
-4	0	0.102	0.095	0.061	0.027	-0.041	-0.067	-0.087	-0.103	-0.107
-3	0	0.103	0.096	0.062	0.028	-0.043	-0.070	-0.091	-0.106	-0.112
-2	0	0.104	0.097	0.063	0.029	-0.044	-0.072	-0.094	-0.110	-0.116
-1	0	0.106	0.098	0.064	0.030	-0.045	-0.074	-0.097	-0.113	-0.120
0	0	0.107	0.099	0.065	0.030	-0.045	-0.076	-0.100	-0.116	-0.124
1	0	0.108	0.099	0.066	0.031	-0.045	-0.078	-0.102	-0.118	-0.127
2	0	0.110	0.100	0.066	0.031	-0.045	-0.079	-0.105	-0.119	-0.130
3	0	0.111	0.100	0.067	0.032	-0.045	-0.079	-0.107	-0.121	-0.132
4	0	0.112	0.100	0.067	0.032	-0.045	-0.080	-0.108	-0.122	-0.134
5	0	0.113	0.100	0.068	0.032	-0.044	-0.080	-0.110	-0.122	-0.136
6	0	0.113	0.100	0.068	0.032	-0.043	-0.080	-0.111	-0.123	-0.137
7	0	0.114	0.099	0.068	0.032	-0.042	-0.080	-0.111	-0.123	-0.138
8	0	0.113	0.098	0.068	0.032	-0.041	-0.079	-0.111	-0.122	-0.138
9	0	0.113	0.096	0.067	0.032	-0.040	-0.078	-0.111	-0.122	-0.138
10	0	0.111	0.094	0.066	0.032	-0.038	-0.077	-0.110	-0.121	-0.137
11	0	0.110	0.092	0.065	0.031	-0.037	-0.075	-0.109	-0.119	-0.135
12	0	0.107	0.089	0.064	0.030	-0.035	-0.073	-0.108	-0.118	-0.133
13	0	0.104	0.086	0.062	0.029	-0.033	-0.071	-0.106	-0.116	-0.131
14	0	0.100	0.082	0.061	0.028	-0.031	-0.068	-0.103	-0.114	-0.128
15	0	0.096	0.078	0.058	0.027	-0.029	-0.065	-0.100	-0.112	-0.124
16	0	0.090	0.073	0.055	0.025	-0.027	-0.062	-0.097	-0.109	-0.120
17	0	0.084	0.068	0.052	0.024	-0.025	-0.058	-0.093	-0.107	-0.115

The drag of the air vehicle also changes with elevator deflection. For any given angle of attack there is only one elevator deflection for minimum aircraft drag. Since the drag change due to elevator deflection is a function of angle of attack, no single value for $CD_{\delta e}$ can be given. Figure 4.7 plots the drag coefficient for elevator deflections from -25° to 20° versus angle of attack. Table 4.5 list the total drag coefficient for different elevator deflections, and Table 4.6 lists the change in drag coefficient from the aircraft's drag with a zero elevator deflection. It is interesting to note that the aircraft's minimum drag at any given angle of attack is only slightly less than the aircraft's drag with the elevator set to trim the aircraft at that angle of attack.

The pitching moment curve versus angle of attack shown in Figure 4.2 for a c.g. located at 33% MAC had a negative slope throughout most of the Pioneer's range of angles of attack. This negative slope of the change in pitching moment with angle of attack is necessary for longitudinal static stability. Since all forces and moments act through the center of gravity, a shift in the aircraft's center of gravity will change the moments. Shifting the c.g. fore or aft changes the pitching moment as a result of changing the moment arm between the lift vector and the new c.g.. The new pitching moment would be calculated for a c.g. at 50% MAC as follows.

$$C_{m(c.g.=50\%MAC)} = C_{m(c.g.=33\%MAC)} + .17C_L$$

For moderate angles of attack, the contribution to the pitching moment due to the moment arm from the new c.g. to the drag vector is small in comparison to the contribution due to the lift vector.

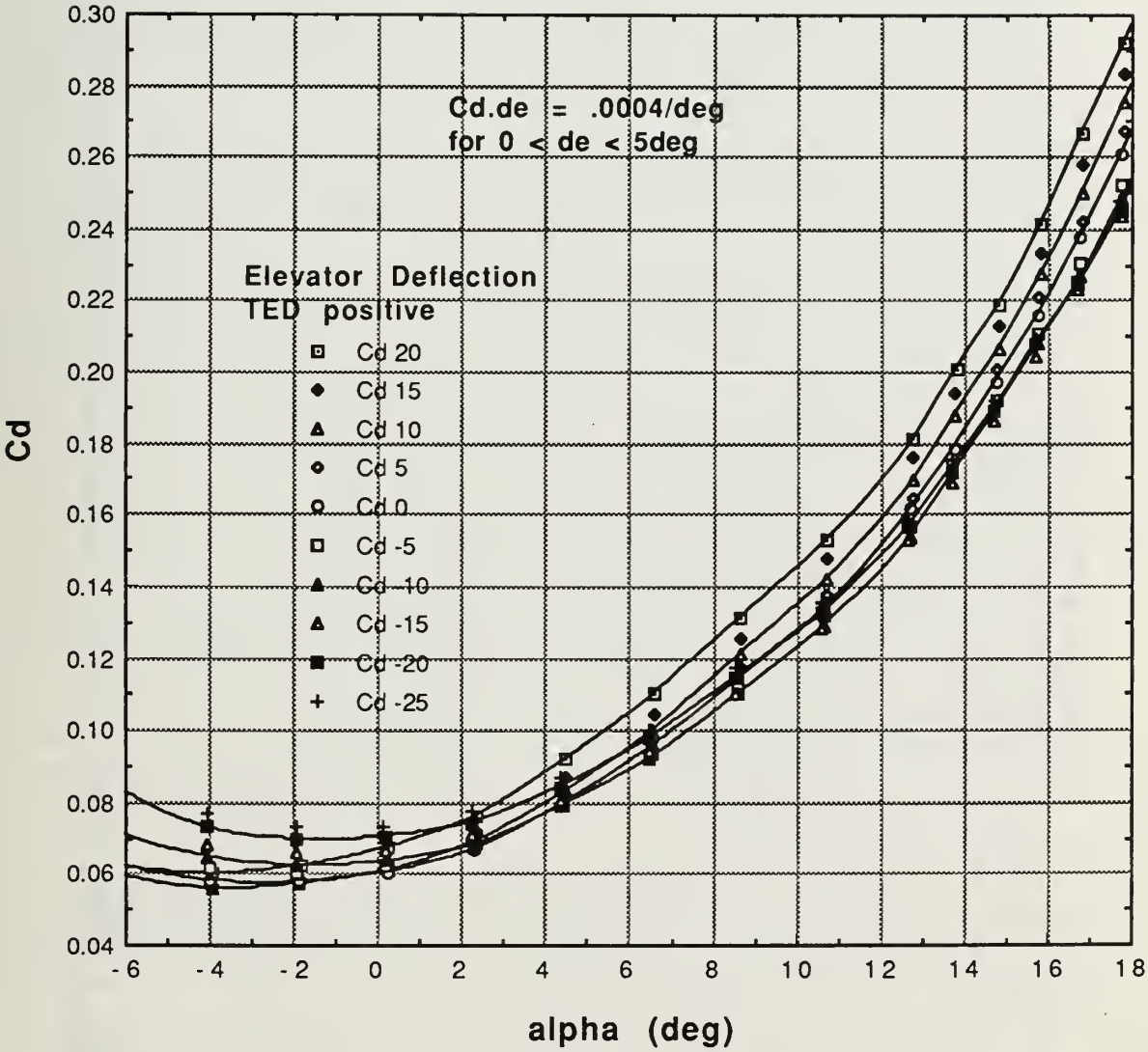

Figure 4.7 Drag Coefficient for Various Elevator Deflections

TABLE 4.5 PIONEER RPV'S DRAG COEFFICIENT

α deg	δe=0	δe=20	δe=15	δe=10	δe=5	δe=-5	δe=-10	δe=-15	δe=-20	δe=-25
- 7	0.0674	0.0645	0.0611	0.0621	0.0646	0.0732	0.0785	0.0852	0.0905	0.0966
- 6	0.0629	0.0622	0.0586	0.0591	0.0608	0.0679	0.0724	0.0784	0.0837	0.0890
- 5	0.0597	0.0608	0.0571	0.0572	0.0581	0.0640	0.0678	0.0732	0.0784	0.0830
- 4	0.0576	0.0604	0.0566	0.0563	0.0566	0.0613	0.0645	0.0694	0.0743	0.0786
- 3	0.0568	0.0609	0.0570	0.0563	0.0562	0.0598	0.0625	0.0669	0.0714	0.0757
- 2	0.0569	0.0623	0.0582	0.0571	0.0567	0.0595	0.0617	0.0656	0.0698	0.0739
- 1	0.0580	0.0645	0.0603	0.0589	0.0581	0.0601	0.0619	0.0654	0.0693	0.0734
0	0.0601	0.0674	0.0632	0.0614	0.0604	0.0617	0.0631	0.0662	0.0699	0.0739
1	0.0630	0.0712	0.0669	0.0648	0.0635	0.0641	0.0652	0.0680	0.0716	0.0754
2	0.0668	0.0759	0.0714	0.0689	0.0675	0.0675	0.0682	0.0707	0.0742	0.0779
3	0.0713	0.0813	0.0766	0.0739	0.0723	0.0716	0.0721	0.0743	0.0777	0.0813
4	0.0767	0.0875	0.0828	0.0797	0.0779	0.0766	0.0768	0.0787	0.0820	0.0855
5	0.0830	0.0946	0.0897	0.0864	0.0843	0.0824	0.0823	0.0840	0.0872	0.0906
6	0.0900	0.1026	0.0976	0.0939	0.0916	0.0891	0.0887	0.0901	0.0931	0.0965
7	0.0980	0.1116	0.1064	0.1024	0.0998	0.0966	0.0960	0.0970	0.0997	0.1033
8	0.1069	0.1215	0.1161	0.1118	0.1089	0.1051	0.1041	0.1048	0.1069	0.1111
9	0.1167	0.1325	0.1269	0.1223	0.1190	0.1145	0.1133	0.1136	0.1147	0.1197
10	0.1276	0.1446	0.1388	0.1339	0.1302	0.1249	0.1234	0.1234	0.1231	0.1294
11	0.1397	0.1579	0.1519	0.1467	0.1425	0.1365	0.1347	0.1343	0.1318	0.1401
12	0.1530	0.1725	0.1663	0.1608	0.1561	0.1493	0.1472	0.1463	0.1410	0.1520
13	0.1676	0.1885	0.1820	0.1763	0.1711	0.1634	0.1609	0.1596	0.1505	0.1652
14	0.1837	0.2060	0.1993	0.1932	0.1875	0.1789	0.1762	0.1743	0.1603	0.1798
15	0.2014	0.2250	0.2181	0.2118	0.2056	0.1960	0.1930	0.1905	0.1704	0.1959
16	0.2209	0.2459	0.2386	0.2320	0.2253	0.2149	0.2116	0.2084	0.1806	0.2137
17	0.2423	0.2685	0.2610	0.2542	0.2470	0.2356	0.2320	0.2282	0.1880	0.2334

TABLE 4.6 CHANGE IN DRAG COEFFICIENT WITH ELEVATOR DEFLECTION

α deg	δe=0	δe=20	δe=15	δe=10	δe=5	δe=-5	δe=-10	δe=-15	δe=-20
- 7	0	-0.0029	-0.0063	-0.0053	-0.0028	0.0058	0.0111	0.0178	0.0231
- 6	0	-0.0007	-0.0043	-0.0037	-0.0021	0.0050	0.0095	0.0155	0.0209
- 5	0	0.0012	-0.0025	-0.0024	-0.0015	0.0043	0.0081	0.0135	0.0187
- 4	0	0.0028	-0.0010	-0.0014	-0.0010	0.0037	0.0069	0.0117	0.0166
- 3	0	0.0042	0.0002	-0.0005	-0.0006	0.0031	0.0057	0.0101	0.0147
- 2	0	0.0053	0.0013	0.0002	-0.0003	0.0025	0.0047	0.0086	0.0129
- 1	0	0.0064	0.0022	0.0008	0.0000	0.0020	0.0038	0.0073	0.0113
0	0	0.0074	0.0031	0.0013	0.0003	0.0016	0.0030	0.0061	0.0098
1	0	0.0082	0.0039	0.0018	0.0005	0.0011	0.0022	0.0050	0.0086
2	0	0.0091	0.0046	0.0022	0.0007	0.0007	0.0015	0.0040	0.0074
3	0	0.0099	0.0053	0.0026	0.0010	0.0003	0.0008	0.0030	0.0063
4	0	0.0108	0.0060	0.0030	0.0012	-0.0001	0.0001	0.0020	0.0053
5	0	0.0117	0.0068	0.0034	0.0014	-0.0005	-0.0006	0.0010	0.0043
6	0	0.0126	0.0076	0.0039	0.0016	-0.0009	-0.0013	0.0000	0.0031
7	0	0.0136	0.0084	0.0044	0.0018	-0.0013	-0.0020	-0.0010	0.0017
8	0	0.0147	0.0093	0.0050	0.0020	-0.0018	-0.0027	-0.0020	0.0001
9	0	0.0158	0.0102	0.0056	0.0023	-0.0022	-0.0035	-0.0031	-0.0020
10	0	0.0170	0.0112	0.0063	0.0025	-0.0027	-0.0042	-0.0042	-0.0046
11	0	0.0182	0.0122	0.0070	0.0028	-0.0032	-0.0050	-0.0054	-0.0079
12	0	0.0195	0.0133	0.0078	0.0031	-0.0037	-0.0058	-0.0067	-0.0120
13	0	0.0209	0.0144	0.0086	0.0035	-0.0043	-0.0067	-0.0080	-0.0171
14	0	0.0222	0.0155	0.0095	0.0038	-0.0048	-0.0075	-0.0094	-0.0234
15	0	0.0236	0.0167	0.0103	0.0041	-0.0054	-0.0084	-0.0109	-0.0311
16	0	0.0250	0.0177	0.0111	0.0045	-0.0060	-0.0093	-0.0125	-0.0403
17	0	0.0263	0.0188	0.0119	0.0048	-0.0066	-0.0102	-0.0141	-0.0543

2. Pitching Moment Changes due to C.G. Location

The stick-fixed neutral point is the c.g. location where the slope of the pitching moment versus angle of attack curve is equal to zero. The center of gravity must always be forward of the stick-fixed neutral point for longitudinal, stick-fixed static stability. Figure 4.8 shows the pitching moment coefficient versus angle of attack for centers of gravity ranging from 33% to 70% MAC. The location and size of the horizontal tail are the primary contributors to the Pioneer RPV's stick-fixed neutral point. The neutral point can be seen to be a function of angle of attack for the Pioneer RPV. Note that the Pioneer RPV's longitudinal stability increases with increasing angle of attack. The Pioneer RPV's stick-fixed neutral point is aft of 70% MAC at angles of attack greater than 5 degrees. Figure 4.9 shows the Pioneer RPV's neutral point as a function of angle of attack.

3. Variations of Coefficients due to Angle of Attack

To find the longitudinal stability coefficients due to changes in angle of attack, polynomial curves were fit to the wind-tunnel data with correlation coefficients of 1.000. Both C_L and C_D were plotted versus angle of attack and were fitted with fourth-order polynomials as a function of angle of attack. A fifth-order curve fit was used for C_m versus alpha. These polynomial curve fits were differentiated to find their change due to angle of attack. Figures 4.10 through 4.12 show the longitudinal coefficients and their change due to angle of attack. The changes due to angle of attack appear somewhat exaggerated by use of the full-range vertical scale of the graphs. Table 4.7 lists the longitudinal coefficients. These stability coefficients are for an untrimmed aircraft with the elevator deflection equal to zero.

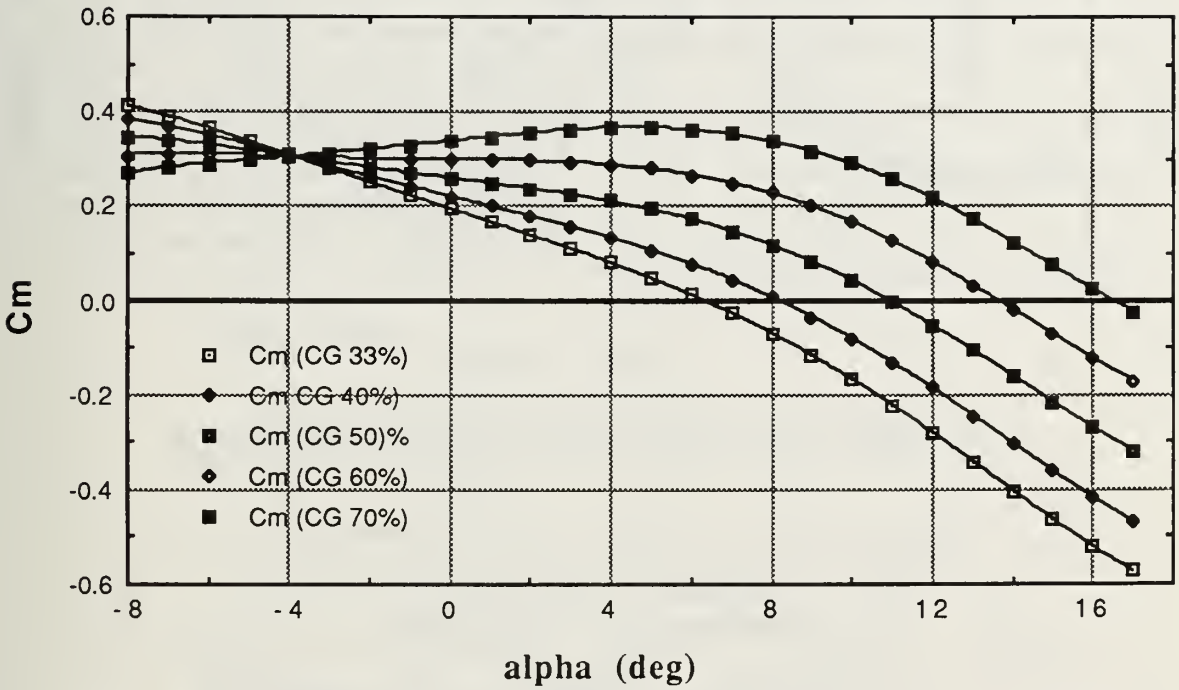

Figure 4.8 Pitching Moment Coefficient with C.G. Shifts

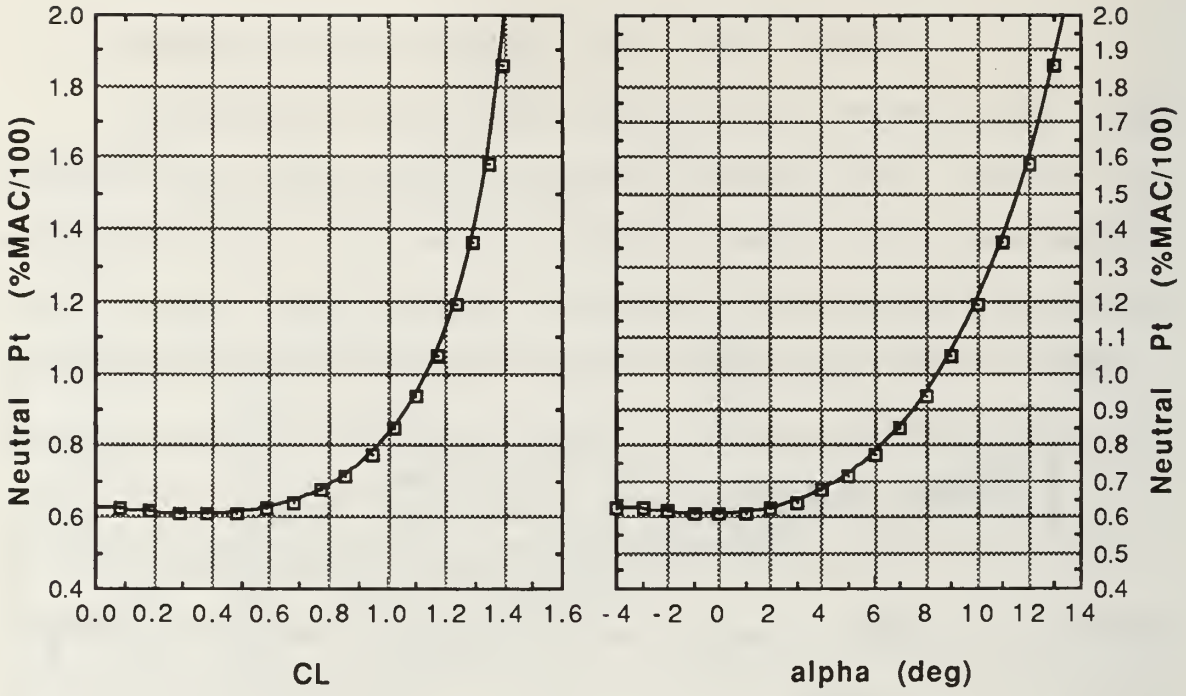

Figure 4.9 Stick Fixed Neutral Point

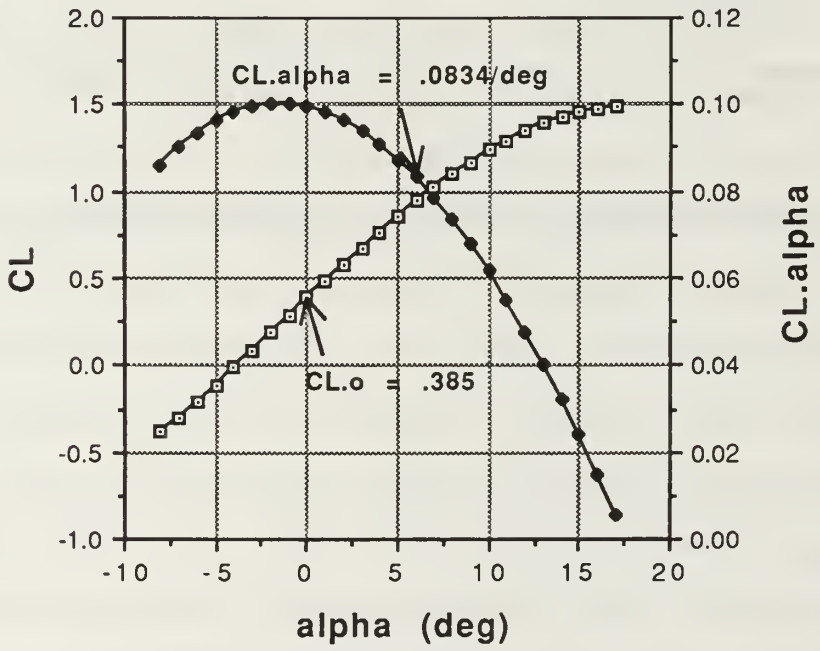

Figure 4.10 Lift Curve and Lift Curve Slope

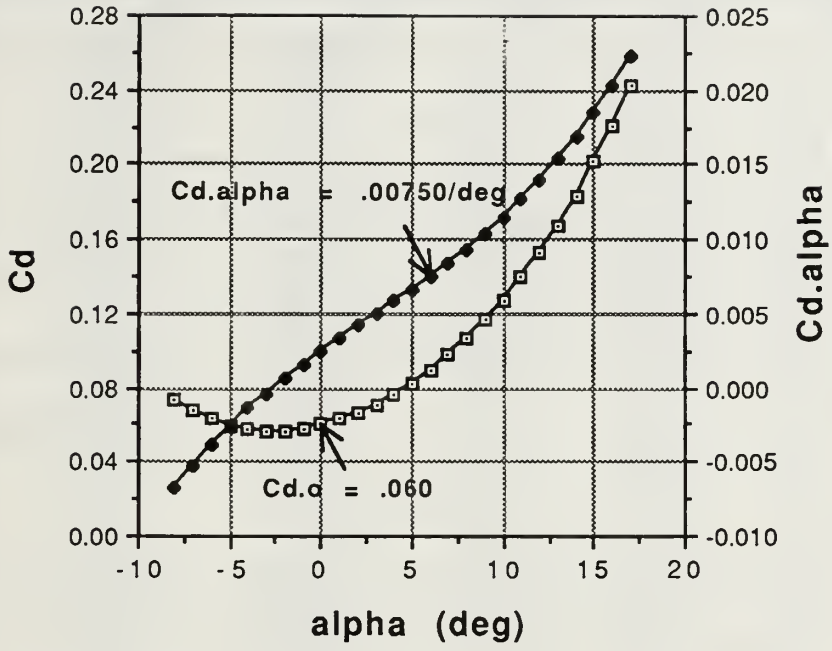

Figure 4.11 Drag Curve and Drag Curve Slope

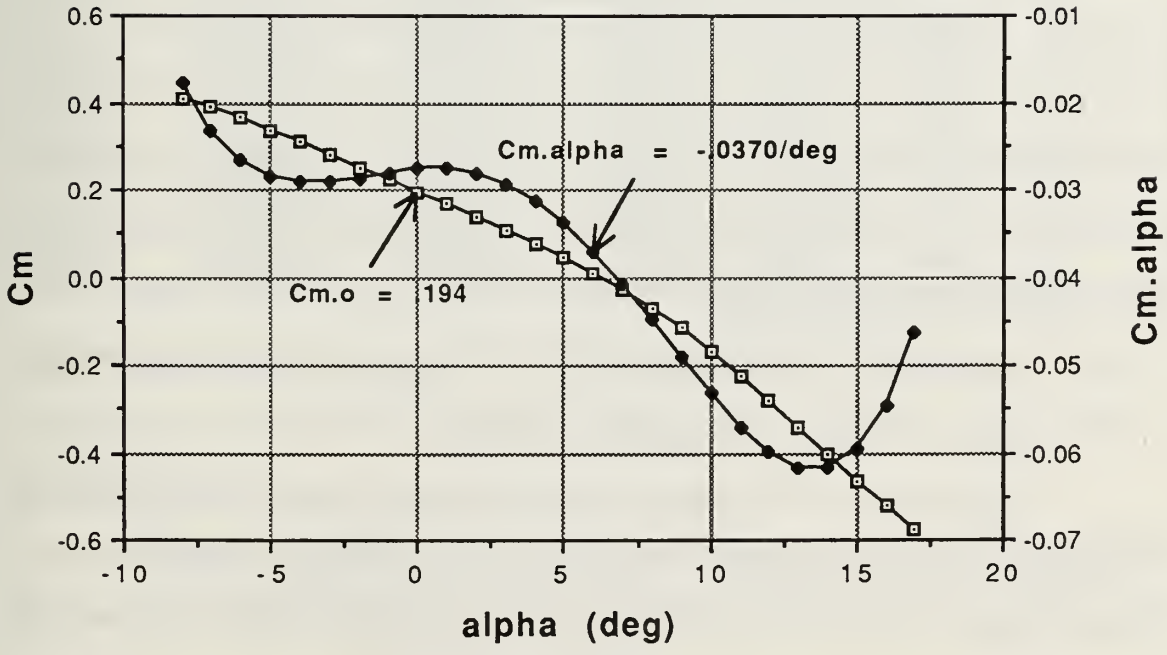

Figure 4.12 Pitching Moment Coefficient and Slope

TABLE 4.7 LONGITUDINAL COEFFICIENTS

α(deg)	CL	CD	Cm	CL_α	CD_α	Cm_α
-8	-0.384	0.0734	0.411	0.0860	-0.0067	-0.0175
-7	-0.294	0.0674	0.390	0.0901	-0.0052	-0.0232
-6	-0.202	0.0629	0.365	0.0935	-0.0039	-0.0267
-5	-0.107	0.0597	0.338	0.0962	-0.0026	-0.0285
-4	-0.010	0.0576	0.309	0.0983	-0.0014	-0.0292
-3	0.088	0.0568	0.279	0.0996	-0.0004	-0.0291
-2	0.187	0.0569	0.251	0.1002	0.0007	-0.0286
-1	0.286	0.0580	0.222	0.1003	0.0016	-0.0281
0	0.385	0.0601	0.194	0.0996	0.0025	-0.0277
1	0.483	0.0630	0.167	0.0984	0.0033	-0.0277
2	0.580	0.0668	0.139	0.0965	0.0042	-0.0282
3	0.674	0.0713	0.110	0.0941	0.0050	-0.0294
4	0.766	0.0767	0.080	0.0911	0.0058	-0.0313
5	0.855	0.0830	0.047	0.0875	0.0066	-0.0338
6	0.940	0.0900	0.012	0.0834	0.0075	-0.0370
7	1.022	0.0980	-0.027	0.0787	0.0084	-0.0407
8	1.098	0.1069	-0.070	0.0735	0.0094	-0.0448
9	1.170	0.1167	-0.116	0.0678	0.0104	-0.0491
10	1.235	0.1276	-0.168	0.0616	0.0115	-0.0532
11	1.295	0.1397	-0.223	0.0549	0.0127	-0.0569
12	1.347	0.1530	-0.281	0.0478	0.0139	-0.0599
13	1.392	0.1676	-0.342	0.0402	0.0154	-0.0616
14	1.430	0.1837	-0.404	0.0322	0.0169	-0.0616
15	1.458	0.2014	-0.465	0.0238	0.0186	-0.0595
16	1.478	0.2209	-0.522	0.0150	0.0204	-0.0546
17	1.488	0.2423	-0.573	0.0058	0.0224	-0.0462

All coefficients are per degree.

4. Variations of Coefficients due to Pitching Velocity and Time Rate of Change of Angle of Attack

Calculations of the change of the longitudinal control coefficients due to either pitching velocity (q) or the time rate of change of angle of attack (αdot) depend on the lift curve slope of the horizontal stabilizer (a_t), the tail efficiency (η), and horizontal tail volume ratio (V_H). The tail efficiency is the

ratio of the dynamic pressure at the tail to the freestream dynamic pressure such that

$$\eta = \frac{q_t}{q}$$

The tail volume ratio is fixed by the aircraft's geometry and c.g. location.

The product, ηa_t, was determined at 0.21° angle of attack by changing the tail incidence angle on otherwise identical runs. If only the tail incidence is changed between runs

$$\Delta C_L S = (\eta a_t)\Delta i_t S_t$$

Runs were made with and without the vertical stabilizers at tail incidence angles of ±3°. ηa_t equaled 0.082 per degree with the vertical stabilizers on and 0.074 per degree with the vertical stabilizers removed. The vertical stabilizers increased ηa_t by 10%. This increase is primarily due to their end-plate effect.

Pitching moment coefficient versus angle of attack was plotted in Figure 4.13 for tail incidence angles of ±3° with and without the vertical stabilizers. The decreased lifting efficiency of the horizontal stabilizer with the vertical stabilizers removed rotated the aircraft's pitching moment coefficient versus angle of attack curve about the point where the tail's contribution to the pitching moment was zero. The horizontal stabilizer's lift, and therefore its contribution to the aircraft's pitching moment, is zero when its local angle of attack is zero.

Drawing a straight line through the intersection points of the curves in Figure 4.13 yields a pitching moment coefficient due to angle of attack curve equivalent to having removed the tail. The premise is that the tail-off pitching moment coefficient curve would be linear at moderate angles of attack.

If the tail-on pitching moment equals the tail-off pitching moment, the tail is at zero lift and

$$\alpha_t = \alpha_w + i_t - \varepsilon_w = 0$$

[Ref. 6:p 289]. Since α_W and i_t are known, the change in downwash with angle of attack ($d\varepsilon_W/d\alpha_W$) was determined by calculating the slope of ε_W as a function of α_W. $d\varepsilon_W/d\alpha_W$ equals 0.30.

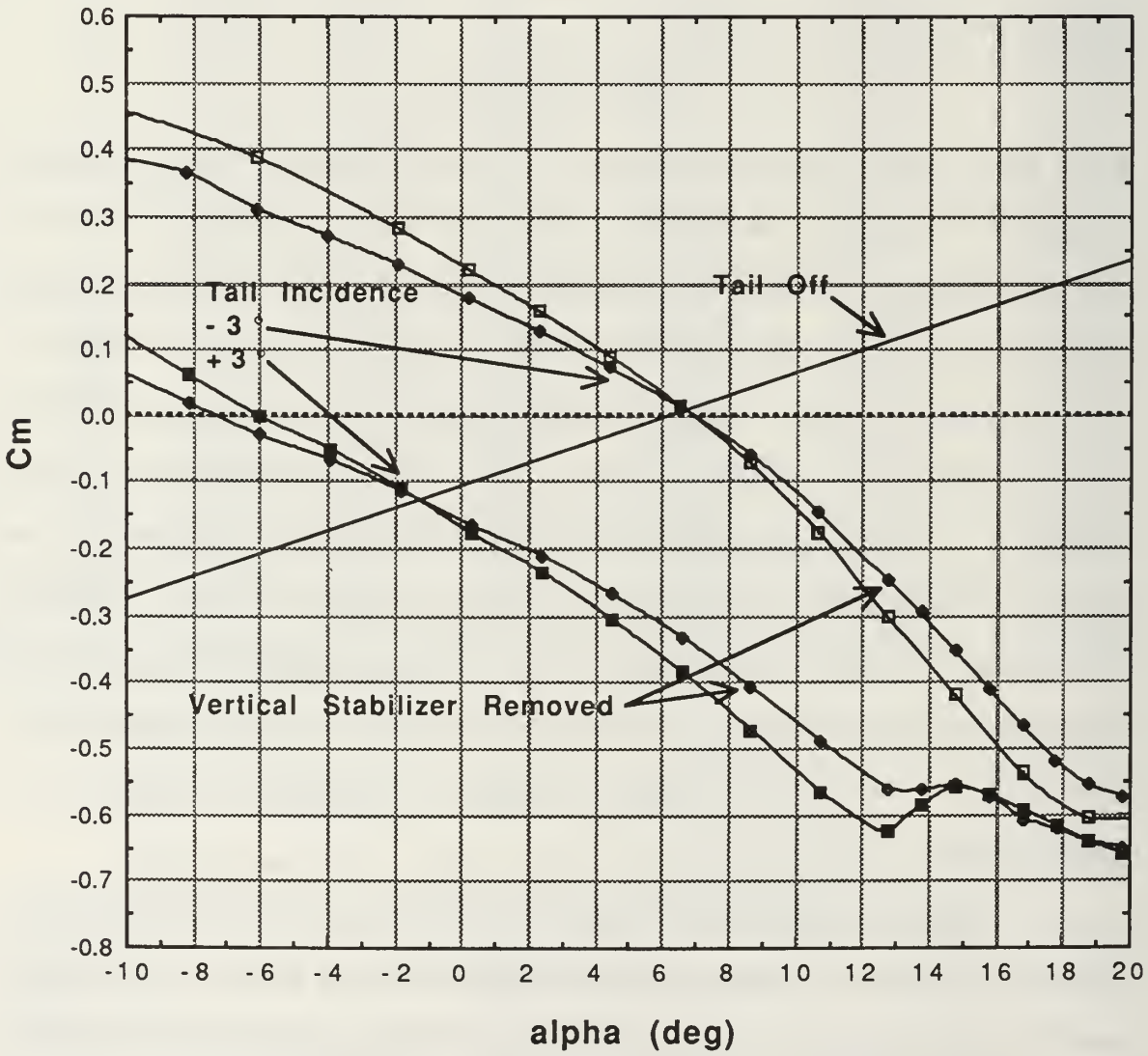

Figure 4.13 Finding Horizontal Tail Zero Angle of Attack

The equations derived by Nelson [Ref. 15: pp 103-106] were used to calculate the change in longitudinal stability coefficients due to both pitching velocity (q) and the time rate of change of the angle of attack (αdot) at 6 degrees angle of attack as follows:

$$C_{L_q} \cong -C_{Z_q} = 2\eta a_t V_H$$

$$C_{L_q} = 0.141 per \deg$$

$$C_{m_q} = -C_{L_q} \frac{l_t}{\bar{c}}$$

$$C_{m_q} = -0.639 per \deg$$

$$C_{L_{\dot{\alpha}}} = C_{L_q} \frac{d\varepsilon_w}{d\alpha_w}$$

$$C_{L_{\dot{\alpha}}} = -0.0423 per \deg$$

$$C_{m_{\dot{\alpha}}} = C_{m_q} \frac{d\varepsilon_w}{d\alpha_w}$$

$$C_{m_{\dot{\alpha}}} = -0.192 per \deg$$

These are nondimensional partial derivatives as defined on page 32 and cannot simply be multiplied by the angular rate. The above equations used only the tail contribution. Sometimes 10% is added to these estimates to account for the wing and fuselage contributions.

F. LATERAL-DIRECTIONAL STATIC STABILITY AND CONTROL

Lateral and directional static stability and control are closely coupled. Lateral refers to roll about the x axis and directional refers to yaw about the z axis. A sideslip (β) produces both rolling and yawing moments. Similarly,

aileron or rudder deflection produces moments about both the x and z axes. The lateral-directional stability and control coefficients due to flight conditions and control input are considered separately. These individual stability and control coefficients can be combined to predict the aircraft's motion.

1. Variations of Coefficients due to Sideslip

Sideslip produces yawing and rolling moments and a sideforce on the aircraft. The Pioneer RPV model was yawed in the wind tunnel from -20° to 20° at 6° angle of attack.

For static directional stability, an aircraft placed in a sideslip should develop a yawing moment that tends to decrease the sideslip. The vertical stabilizers are the primary contributors to positive directional stability. A sideslip produces a sideforce on the vertical tail that creates the restoring moment about the aircraft's center of gravity. Directional or weathercock stability can be increased by increasing the vertical tail area or lengthening its moment arm from the aircraft's center of gravity. The Pioneer RPV displayed good directional stability: Cn_β is greater than 0 up to 15° sideslip (Figure 4.14). A least squares curve fit in the linear region of Figure 4.14 ($-15° < \beta < 15°$) of the yaw moment coefficient versus sideslip yielded a Cn_β equal to 0.0019 per degree sideslip.

The sideforce versus sideslip was plotted from a fourth order polynomial equation as a function of sideslip with a correlation coefficient of 0.999 in Figure 4.15. This polynomial curve fit was differentiated to find its change due to sideslip.

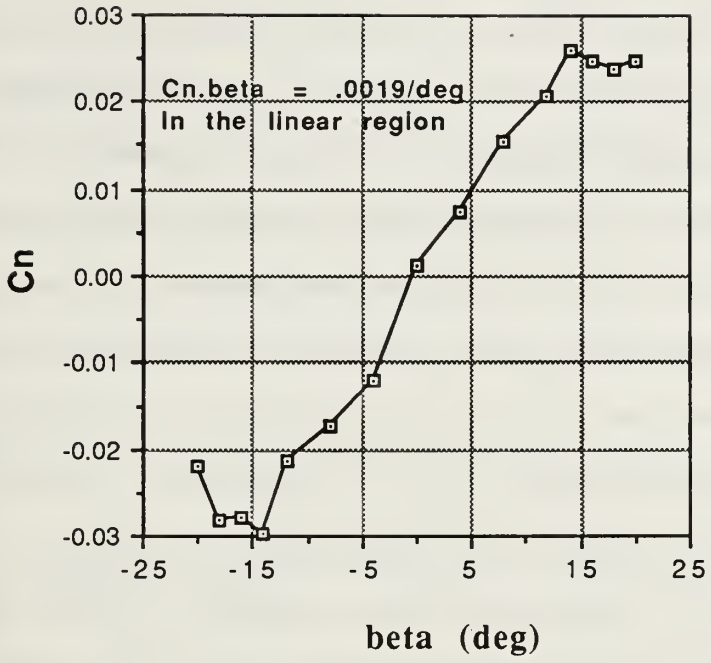

Figure 4.14 Yaw Moment Coefficients at 6° AOA

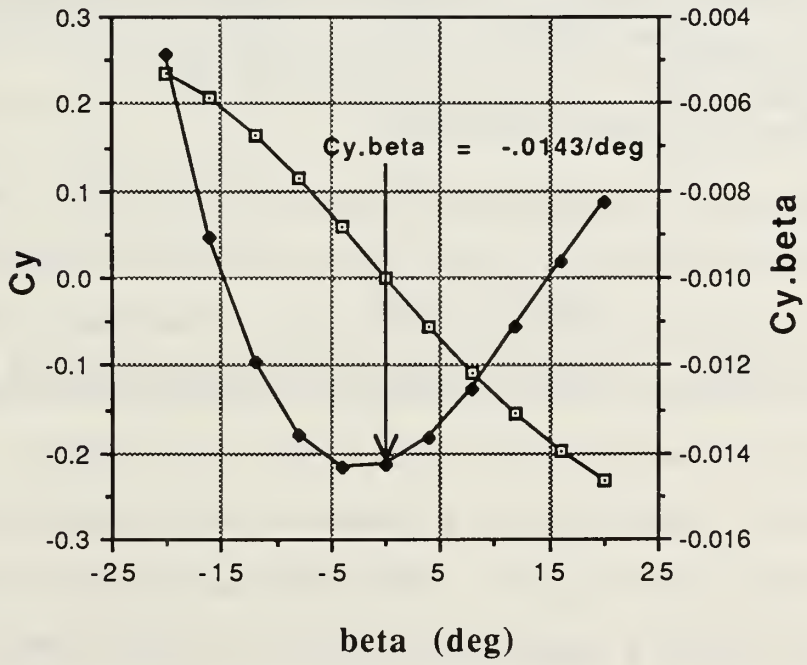

Figure 4.15 Side Force Coefficients at 6° AOA

Static roll stability is defined such that a disturbance from equilibrium produces a restoring roll moment ($Cl_\beta<0$). The major contributors to roll moment due to sideslip of the Pioneer RPV are the wing position on top of the fuselage and the vertical tail, neither of which produces a strong restoring roll moment due to sideslip. The roll moment contribution due to wing position results from the higher local angle of attack of the upwind wing near the fuselage. The roll moment due to the vertical tail is a consequence of the sideforce on the tail and its moment arm from the center of gravity in the z direction. This moment arm is small for moderate angles of attack. The roll-moment coefficient due to sideslip at 6° angle of attack is -0.0004 per degree. The Pioneer RPV is nearly neutrally stable in roll due to sideslip. The magnitude and sign of the roll-moment coefficient due to sideslip partly depends on the moment arm between the center of pressure of the vertical tail and the aircraft's center of gravity. At normal flight speeds $Cl_\beta < 0$.

2. Effect of Aileron Deflection

Roll control is produced by deflection of the ailerons. An undesired effect of deflecting the ailerons is the adverse yaw produced, which is normally corrected by simultaneous deflection of the rudders. The Pioneer RPV autopilot automatically deflects the rudders one-half the commanded aileron deflection to compensate for adverse yaw when in the autopilot mode of flight.

Aileron control power is a function of angle of attack; sideslip has negligible effect on aileron power. Aileron deflection produces an aerodynamic force which produces a rolling moment about the aircraft's center of gravity. Figure 4.16 shows that aileron power decreases at angles of attack greater than

about 8 degrees. The actual roll coefficient versus aileron deflection is listed in Table 4.8.

Figure 4.17 shows that adverse yaw due to aileron deflection increases with angle of attack and is zero at -4° angle of attack (corresponding to C_L equal to 0). The yawing moment coefficients versus angle of attack listed in Table 4.9 were calculated from the curve fits shown in Figure 4.18. These polynomial curve fits were used to smooth the apparent scatter in the data.

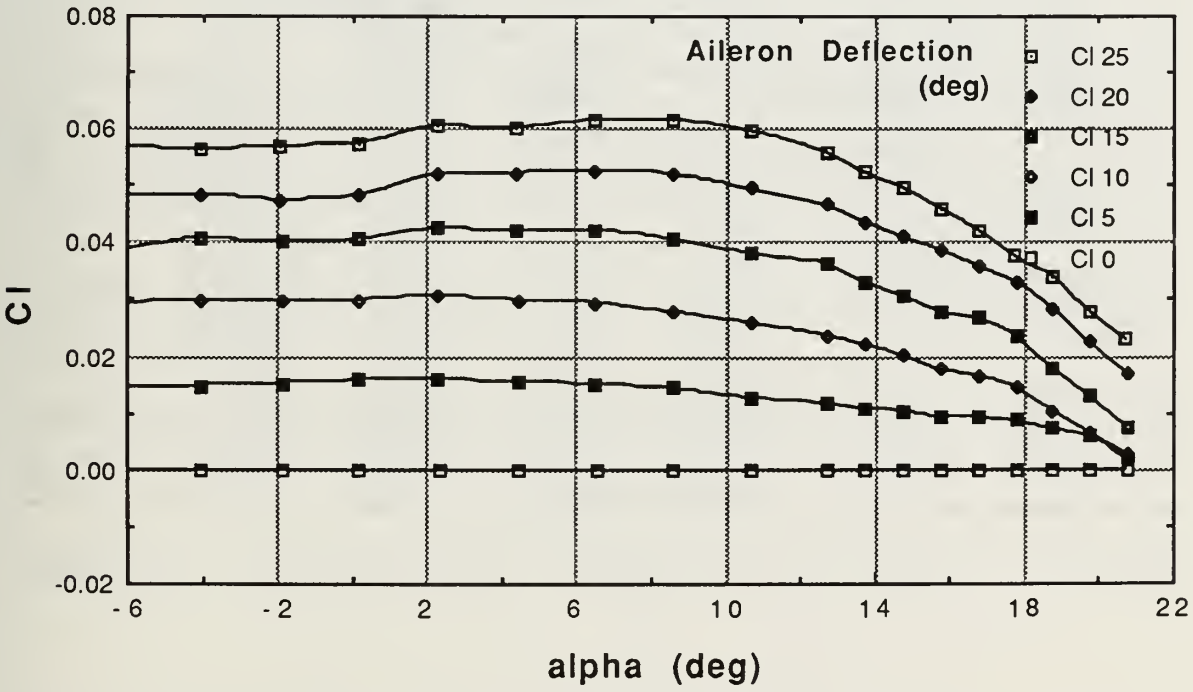

Figure 4.16 Roll Moment Coefficient due to Aileron Deflection

TABLE 4.8 ROLL MOMENT COEFFICIENT (C_l) DUE TO AILERON DEFLECTION

α (deg)	δa=25	δa=20	δa=15	δa=10	δa=5	δa=0
-10.31	0.0533	0.0446	0.0366	0.0280	0.0140	0
-8.22	0.0553	0.0463	0.0375	0.0281	0.0143	0
-6.12	0.0568	0.0482	0.0386	0.0292	0.0148	0
-4.01	0.0563	0.0484	0.0408	0.0299	0.0148	0
-1.91	0.0568	0.0475	0.0400	0.0296	0.0153	0
0.20	0.0573	0.0482	0.0405	0.0299	0.0158	0
2.29	0.0604	0.0519	0.0424	0.0308	0.0160	0
4.40	0.0601	0.0522	0.0422	0.0300	0.0156	0
6.50	0.0614	0.0527	0.0422	0.0295	0.0152	0
8.59	0.0616	0.0521	0.0407	0.0279	0.0144	0
10.65	0.0597	0.0495	0.0382	0.0260	0.0128	0
12.71	0.0558	0.0466	0.0364	0.0238	0.0118	0
13.72	0.0524	0.0437	0.0332	0.0222	0.0109	0
14.73	0.0497	0.0411	0.0307	0.0202	0.0105	0
15.74	0.0461	0.0388	0.0280	0.0177	0.0093	0
16.75	0.0423	0.0360	0.0267	0.0167	0.0093	0
17.75	0.0376	0.0333	0.0238	0.0147	0.0087	0
18.75	0.0342	0.0285	0.0179	0.0105	0.0073	0
19.74	0.0280	0.0226	0.0130	0.0066	0.0061	0
20.73	0.0229	0.0170	0.0077	0.0028	0.0016	0

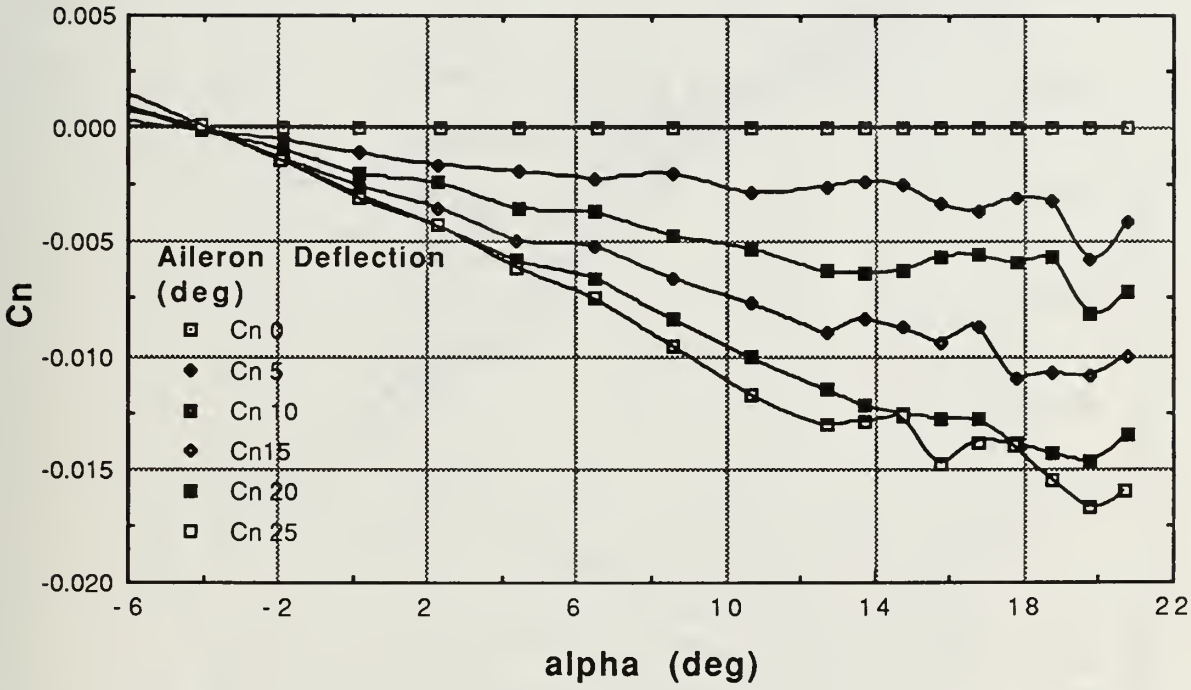

Figure 4.17 Yaw Moment Coefficient due to Aileron Deflection

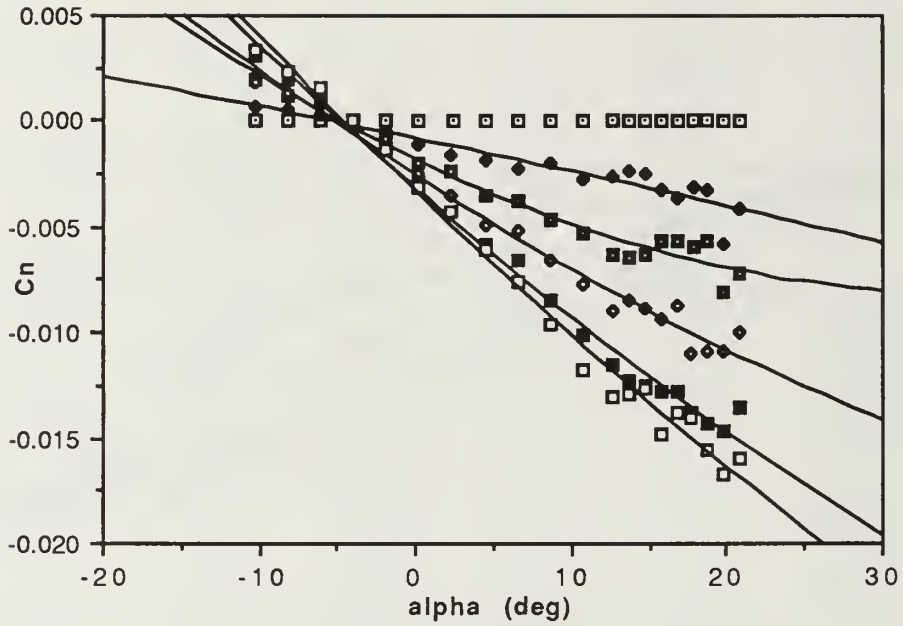

Cn 0	y = 0x + 0x^2	R^2 = Undefined
Cn 5	y = - 8.3326e-4 - 1.5281e-4x - 3.7905e-7x^2	R^2 = 0.892
Cn 10	y = - 1.8456e-3 - 3.5155e-4x + 4.8416e-6x^2	R^2 = 0.968
Cn15	y = - 2.5822e-3 - 4.6999e-4x + 2.8274e-6x^2	R^2 = 0.984
Cn 20	y = - 3.1528e-3 - 6.4130e-4x + 3.1082e-6x^2	R^2 = 0.991
Cn 25	y = - 3.3035e-3 - 7.0646e-4x + 2.6845e-6x^2	R^2 = 0.990

Figure 4.18 Yaw Moment Coefficient due to Aileron Deflection Curve Fit

TABLE 4.9 ADVERSE YAW MOMENT COEFFICIENT (C_n) DUE TO AILERON DEFLECTION

α (deg)	δa=25	δa=20	δa=15	δa=10	δa=5	δa=0
-8	0.0025	0.0022	0.0014	0.0013	0.0004	0
-7	0.0018	0.0015	0.0008	0.0009	0.0002	0
-6	0.0010	0.0008	0.0003	0.0004	0.0001	0
-5	0.0003	0.0001	-0.0002	0.0000	-0.0001	0
-4	-0.0004	-0.0005	-0.0007	-0.0004	-0.0002	0
-3	-0.0012	-0.0012	-0.0011	-0.0007	-0.0004	0
-2	-0.0019	-0.0019	-0.0016	-0.0011	-0.0005	0
-1	-0.0026	-0.0025	-0.0021	-0.0015	-0.0007	0
0	-0.0033	-0.0032	-0.0026	-0.0018	-0.0008	0
1	-0.0040	-0.0038	-0.0030	-0.0022	-0.0010	0
2	-0.0047	-0.0044	-0.0035	-0.0025	-0.0011	0
3	-0.0054	-0.0050	-0.0040	-0.0029	-0.0013	0
4	-0.0061	-0.0057	-0.0044	-0.0032	-0.0015	0
5	-0.0068	-0.0063	-0.0049	-0.0035	-0.0016	0
6	-0.0074	-0.0069	-0.0053	-0.0038	-0.0018	0
7	-0.0081	-0.0075	-0.0057	-0.0041	-0.0019	0
8	-0.0088	-0.0081	-0.0062	-0.0043	-0.0021	0
9	-0.0094	-0.0087	-0.0066	-0.0046	-0.0022	0
10	-0.0101	-0.0093	-0.0070	-0.0049	-0.0024	0
11	-0.0107	-0.0098	-0.0074	-0.0051	-0.0026	0
12	-0.0114	-0.0104	-0.0078	-0.0054	-0.0027	0
13	-0.0120	-0.0110	-0.0082	-0.0056	-0.0029	0
14	-0.0127	-0.0115	-0.0086	-0.0058	-0.0030	0
15	-0.0133	-0.0121	-0.0090	-0.0060	-0.0032	0
16	-0.0139	-0.0126	-0.0094	-0.0062	-0.0034	0
17	-0.0145	-0.0132	-0.0098	-0.0064	-0.0035	0

3. Effect of Rudder Deflection

Rudder deflection creates an aerodynamic sideforce that acts at a fixed distance from the aircraft's center of gravity. This sideforce produced by rudder deflection has a linear slope up to about 13 degrees sideslip. As shown

in Figure 4.19, the sideforce coefficient due to rudder deflection is 0.0033 per degree rudder deflection for rudder deflections less than 15 degrees and 0.0014 per degree rudder deflection for rudder deflections from 15 to 25 degrees.

Figure 4.20 shows the yawing moment coefficient versus sideslip for rudder deflections from 0° to 25°. The yawing moment coefficient due to rudder deflection is -0.0016 per degree rudder deflection for rudder deflections less than 15 degrees and -0.0007 per degree rudder deflection for rudder deflections from 15 to 25 degrees. The sideslip angle and crosswind capabilities due to rudder power will be discussed in the performance chapter.

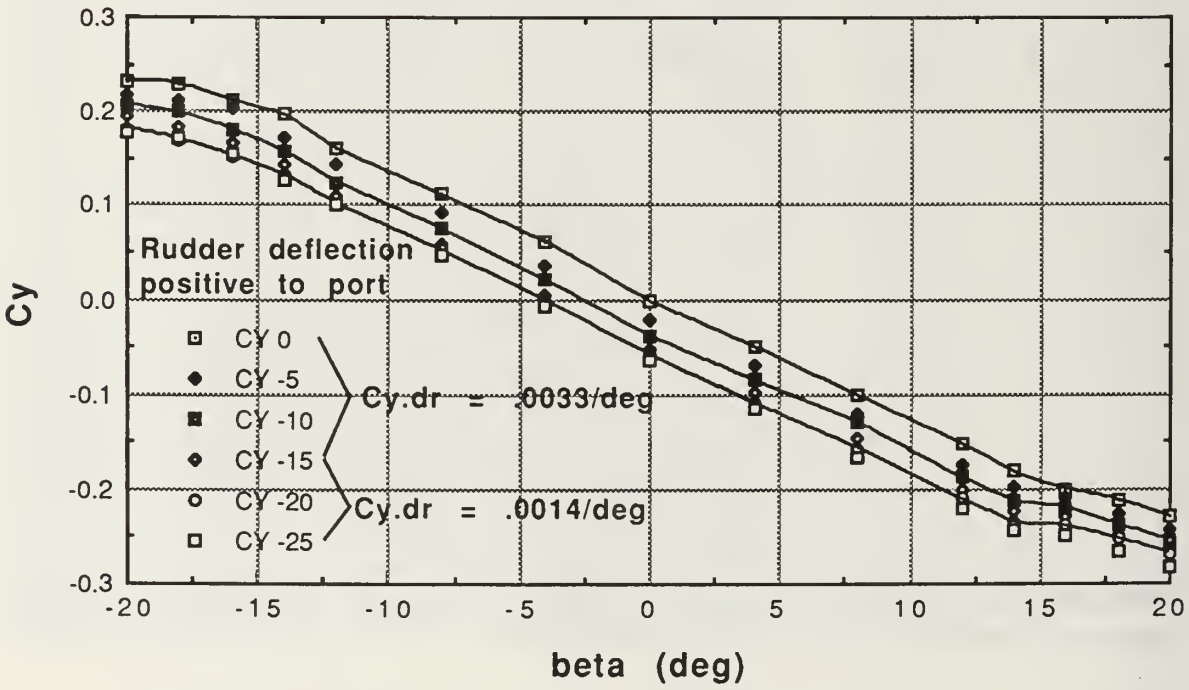

Figure 4.19 Side Force Coefficient at 6° AOA

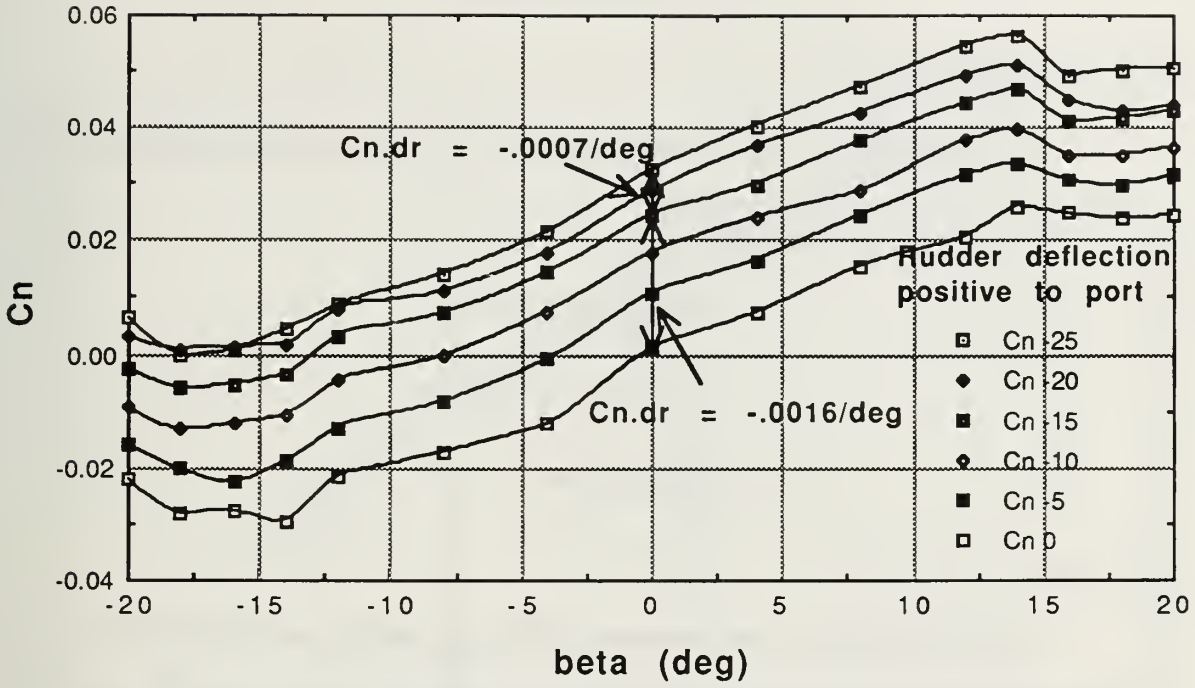

Figure 4.20 Yaw Moment Coefficient at 6° AOA

4. Variations of Coefficients due to Roll and Yaw Rates

The change in the lateral-directional control coefficients due to roll rate and yaw rate were estimated using the methods outlined in the USAF Stability and Control Datcom [Ref. 16] at an aircraft angle of attack of 6 degrees.

The variation of roll moment coefficient with roll rate is a function of the wing lift-curve slope, the wing drag and geometric dihedral. The Pioneer RPV wing has no dihedral, giving

$$C_{l_p} = (C_{l_p})_{winglift} + (\Delta C_{l_p})_{drag}$$

$$C_{l_p} = -0.443 - 0.0075 = -0.450 \text{ per rad}$$

[Ref. 16:p. 7.1.2.2-2]

The variation of yaw moment coefficient with roll rate is due to the asymmetrical lift distribution:

$$C_{n_p} = -0.110 \text{ per rad}$$

[Ref. 16:p. 7.1.2.3-2]

The variation of roll moment coefficient with yaw rate is due to the lift differential between the wing panels:

$$C_{l_r} = C_L(\frac{C_{l_r}}{C_L})_{C_L=0} + (\Delta C_{l_r})_{C_L}$$

$$C_{l_r} = 0.945 * 0.28 + 0.00127$$

$$C_{l_r} = 0.265 \text{ per rad}$$

[Ref. 16:p. 7.1.3.2-2]

The variation of yaw moment coefficient with yaw rate is due to the antisymmetrical lift and drag distributions over the wing resulting from the yawing velocity.

$$C_{n_r} = -.0200 \text{ per rad}$$

[Ref. 16:p. 7.1.3.3-2]

G. FUSELAGE EFFECTS

The fuselage was removed and the wing and tail surfaces, connected together by the tail booms, were tested. The fuselage created a slight reduction in lift except at high angles of attack (Figure 4.21). At high angles of attack, where most of the airflow had separated from the upper wing surfaces, the fuselage contributed to the lift due to its airflow remaining attached to the its flat upper surface. The fuselage responds to angle of attack changes in a manner similar to a very low aspect ratio wing. The fuselage has a destabilizing effect on the pitching moment curve as expected (Figure 4.21).

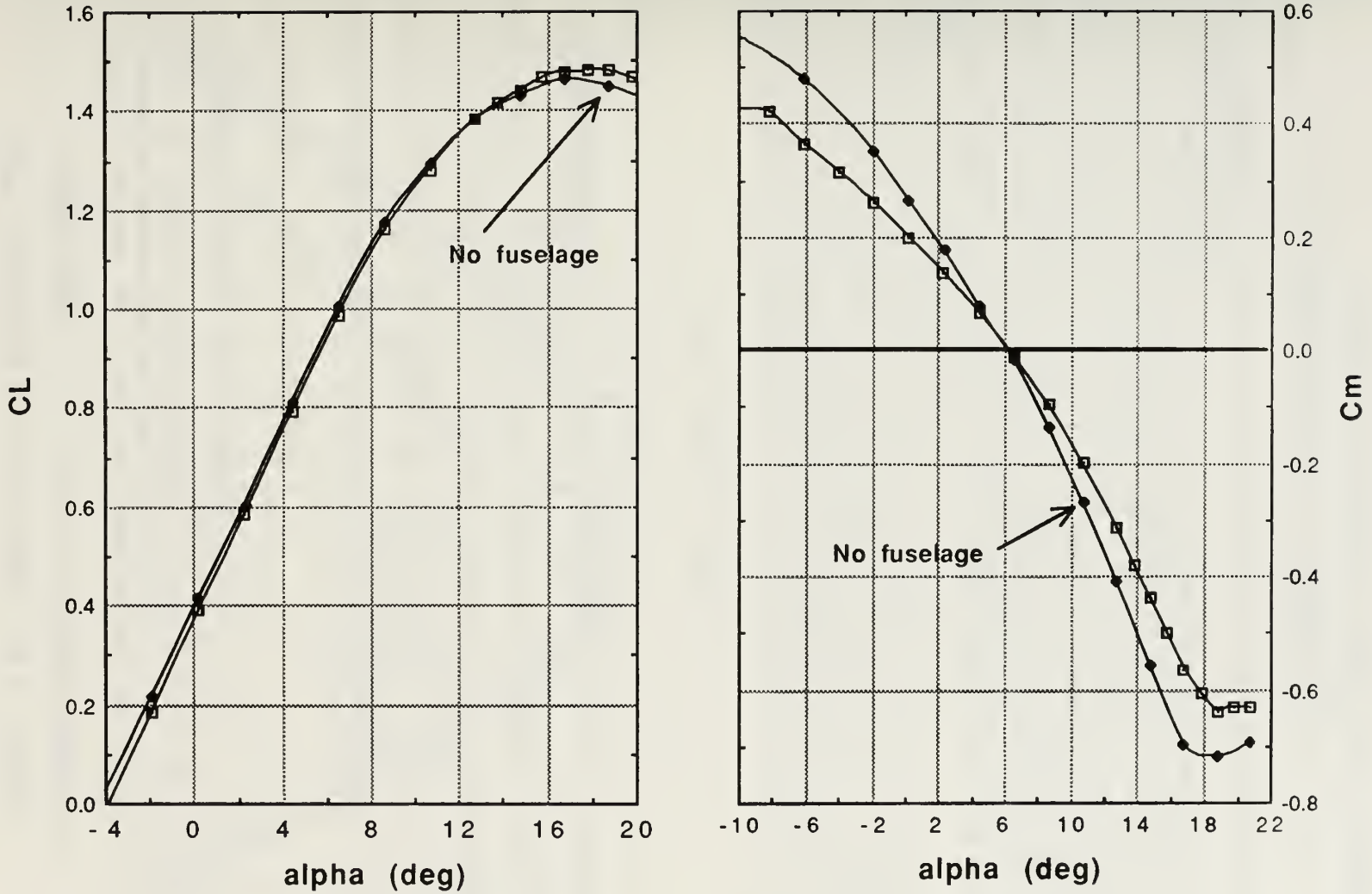

Figure 4.21 Fuselage Effects on Lift and Pitching Moment

H. EFFECTS OF TAIL INCIDENCE ANGLE

Figure 4.22 is included to illustrate the importance of choosing the correct tail incidence angle when designing an aircraft. The pitching moment coefficient versus angle of attack curve in the right half of Figure 4.22 shows that the aircraft as designed with a tail incidence angle of -3° will trim ($C_m = 0$) at about 6 degrees angle of attack, which is close to the predicted maximum range angle of attack of 6.5 degrees. Additionally, the minimum trim drag occurs if the elevator deflection is zero at the desired flight speed. It appears that the Pioneer RPV's horizontal tail incidence angle was chosen correctly for its mission. If it is desired to optimize flight at a different airspeed, the trim angle of attack would change by one degree per degree change in tail incidence angle.

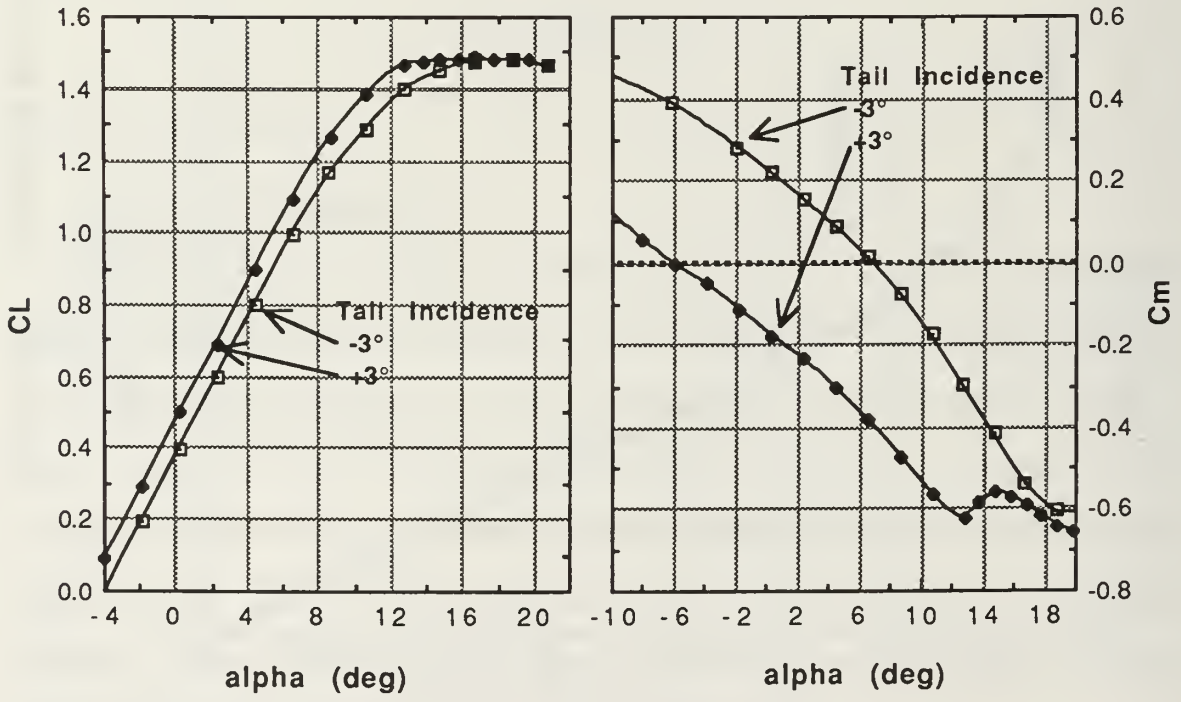

Figure 4.22 Effect of Tail Incidence Angle

V. PERFORMANCE ANALYSIS

A. INTRODUCTION

Aircraft performance is a primary criterion in aircraft selection. Data acquired from the Pioneer RPV wind-tunnel test were used to describe its flight characteristics. Performance calculations were made by combining this newly acquired aerodynamic data with previously predicted power available, known weights, and atmospheric conditions.

Performance calculations assumed standard day conditions as defined by the 1959 U.S. Air Force Air Research and Development Command (ARDC) Model Atmosphere. Standard sea level values of density and temperature are

$$\rho_S = 0.002377 \text{ slug/ft}^3$$

and

$$T_S = 58.69°F$$

Power available data were extracted from the Naval Air Propulsion Center's Pioneer RPV Propulsion System Test of 27 May 1988. This propulsion test used the Sachs SF 2-350, 26 hp, air-cooled, two-cycle engine installed on the full-scale vehicle in an atmospheric altitude chamber. The installed engine turned a two-bladed, 29-inch prop and had a 600-watt alternator load. [Ref. 17]

B. AIRSPEED MEASUREMENT

Velocity or airspeed can be measured several ways. In most flight conditions, the Pioneer's airspeed indicator does not indicate true airspeed (V_t), but indicated airspeed (V_i). Indicated airspeed may vary from actual flight speed due to such factors as an air density different than standard sea level

density, instrument calibration errors, pitot-static system position errors, and compressibility effects.

Calibrated airspeed (V_c) results from correcting indicated airspeed for errors in calibration and errors due to the location of the pitot and static sources. Normally, instrument calibration errors are small since the gages and pressure transducers are easily calibrated. Position errors can be significant when the aircraft is operated throughout a large range of angles of attack. Most position errors result from the static pressure port sensing a static pressure different from the freestream static pressure due to a locally disturbed flowfield. The Pioneer RPV probably has additional position errors due to the use of a short pitot tube located on the nose of the aircraft, where it is probably within the induced pressure field of the aircraft and subject to local angles of attack greater than those of the aircraft.

Equivalent airspeed (V_e) is calibrated airspeed corrected for compressibility effects. Compressibility effects are relatively small in the slow-airspeed, low-altitude flight regime of the Pioneer RPV.

True airspeed (V_t) is equivalent airspeed corrected for density altitude. On a windless day, true airspeed would be the aircraft's ground speed. Since the airspeed indicator is calibrated for the dynamic pressures corresponding to airspeeds at standard sea level conditions, corrections must be applied for different air densities.

The graphs in this report use calibrated airspeed unless otherwise stated. Calibrated airspeed was chosen for ease of comparison with the indicated airspeeds seen by the internal pilots when flying the Pioneer RPV. Although calibrated airspeeds will be the closest to the indicated airspeeds seen by the

internal pilot, an accurate flight-test-based airspeed calibration is required for accurate correlation of predicted performance airspeeds to indicated airspeeds.

At standard sea level conditions, true airspeed and calibrated airspeed are the same if we disregard the relatively insignificant compressibility effects at the Pioneer's flight speeds. An airspeed indicator will indicate true airspeed only at sea level (assuming that there are no position, instrument calibration or compressibility errors). At altitude, or when the air density is less than standard sea level density, the airspeed indicator will read lower than the aircraft's true airspeed.

Like the aircraft, the airspeed indicator responds to the dynamic air pressure. In other words, the air speed indicator acts as a flight condition (angle of attack) indicator at a given aircraft weight. As an example, an aircraft will stall at the angle of attack for maximum lift regardless of altitude, and similarly, for a given weight, the indicated stall speed will not change with altitude.

Drag also depends on dynamic pressure and not true airspeed. Therefore, at higher altitudes an aircraft will have the same drag at a given indicated airspeed as it did at sea level, but the true airspeed will be higher. The penalty paid is that although the drag is the same, the power required increases as true airspeed increases.

$$P_{req} = T_{req} V_t \frac{1.6878}{550} \tag{5.1}$$

where $T_{req} = Drag$

for level unaccelerated flight.

C. PERFORMANCE CALCULATIONS

All performance calculations were based on a trimmed flight condition, where the pitching moment equaled zero. The center of gravity was set at 33% MAC on the thrust line. Angles of attack were referenced to the fuselage water line. To determine the trimmed flight condition, angle of attack sweeps were performed with elevator settings from -25 to 20 degrees deflection in five-degree increments. For each elevator setting there was only one angle of attack that gave a zero pitching moment.

1. Lift

Figure 5.1 shows the construction of the trim lift curve shown in Figure 5.2. Items of interest are the slope of the lift curve, the maximum lift, the angle of zero lift and the stall characteristics. The lift curve slope in the linear region was 0.0834 per degree. Figure 5.2 shows a maximum lift coefficient of 1.36. Zero lift occurs at -4.6 degrees angle of attack. The gradual change in the slope of the lift curve near C_{Lmax} indicates gentle stall characteristics. A conventional stall is characterized by a progressive loss of lift normally accompanied by a nose-down pitching moment caused by the change in downwash at the horizontal stabilizer due to flow separation on the wing. The trimmed lift curve in Figure 5.2 indicates that the Pioneer RPV will probably not have an abrupt stall break. Elevator deflection is limited to ±20 degrees. Figure 5.2 shows that the maximum lift occurs at about 16 degrees angle of attack as the elevator reaches its maximum deflection of -20 degrees. Note that the elevator power decreases at high angles of attack.

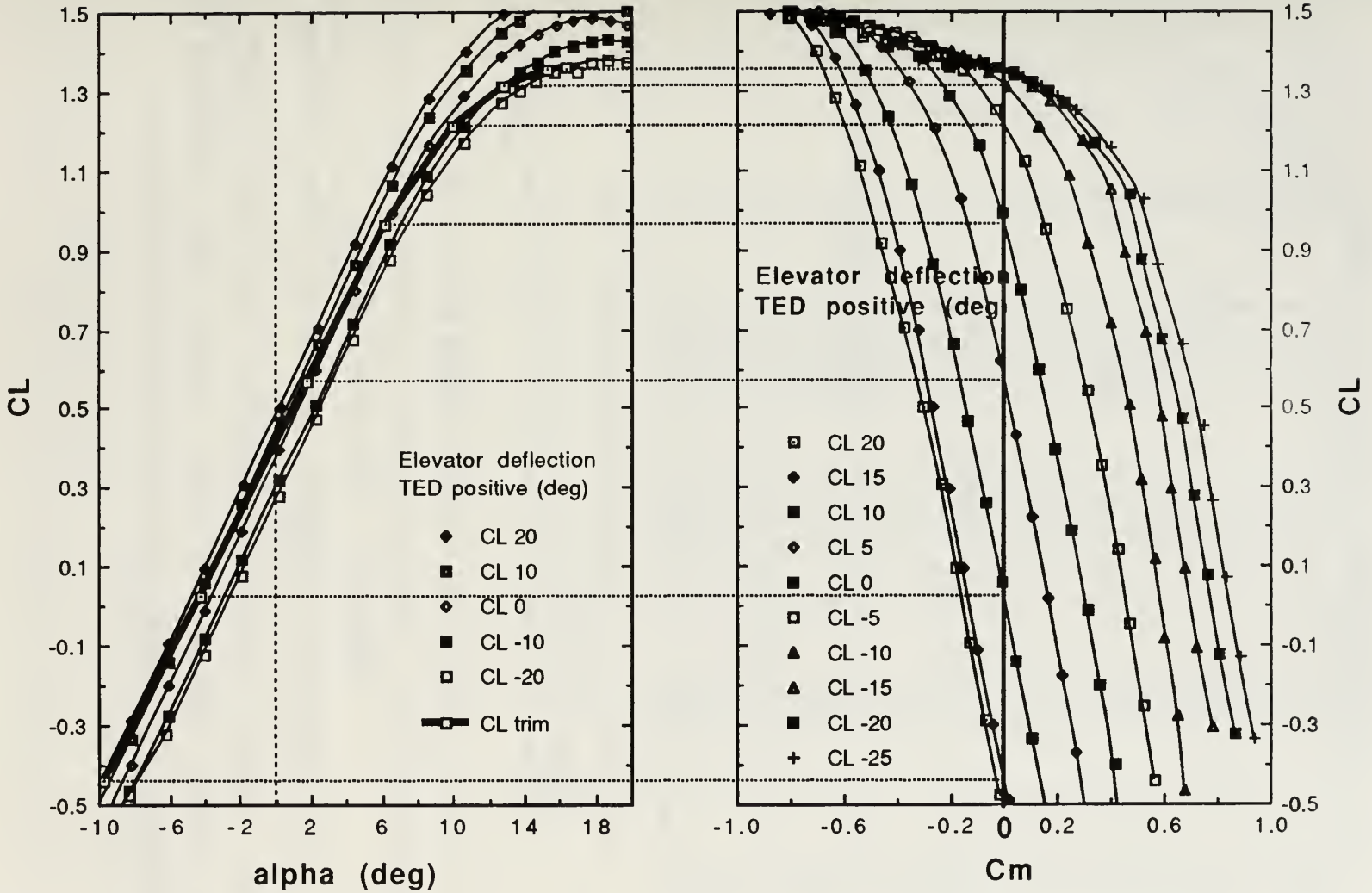

Figure 5.1 Construction of Trim Lift Curve

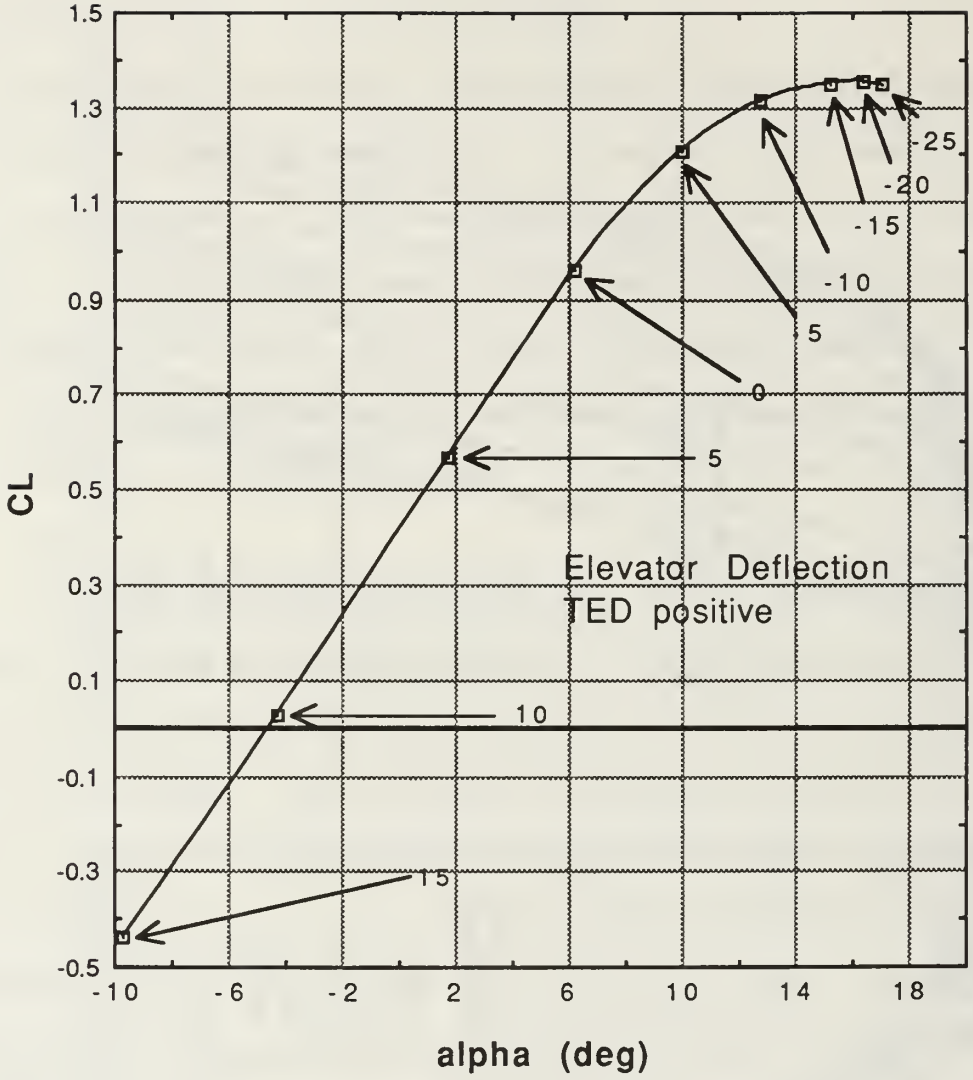

Figure 5.2 Trim Lift Curve

For performance calculations, lift and drag were calculated as functions of angle of attack from polynomial curve fits of the wind-tunnel data with correlation coefficients of 0.999. Trimmed values of lift and drag coefficients are listed in Table 5.1.

TABLE 5.1 TRIM COEFFICIENTS

alpha (deg)	CL trimmed	CD trimmed	CL/CD	$CL^{1.5}/CD$
- 2	0.234	0.0571	4.09	1.98
- 1	0.327	0.0591	5.54	3.17
0	0.420	0.0617	6.81	4.42
1	0.513	0.0650	7.89	5.65
2	0.604	0.0688	8.77	6.82
3	0.693	0.0733	9.46	7.87
4	0.779	0.0783	9.95	8.78
5	0.862	0.0840	10.27	9.53
6	0.941	0.0903	10.42	10.11
7	1.016	0.0974	10.43	10.51
8	1.085	0.1053	10.31	10.73
9	1.148	0.1140	10.07	10.79
10	1.204	0.1238	9.73	10.68
11	1.253	0.1346	9.31	10.42
12	1.293	0.1468	8.81	10.02
13	1.325	0.1603	8.26	9.51
14	1.347	0.1755	7.67	8.91
15	1.358	0.1924	7.06	8.22
16	1.357	0.2113	6.42	7.48
17	1.344	0.2324	5.78	6.71

2. Drag

Drag has a large effect on aircraft performance and the drag at C_{Lmax} is used for takeoff and landing calculations. Drag increases as the square of the true velocity:

$$D = .5\rho V_t^2 S C_D$$

with V_t in fps.

A drag polar is a visual representation of the drag characteristics of the aircraft in a trimmed flight condition. The Pioneer RPV's drag polar is shown in Figure 5.3. The plot of C_D versus angle of attack in the right half of

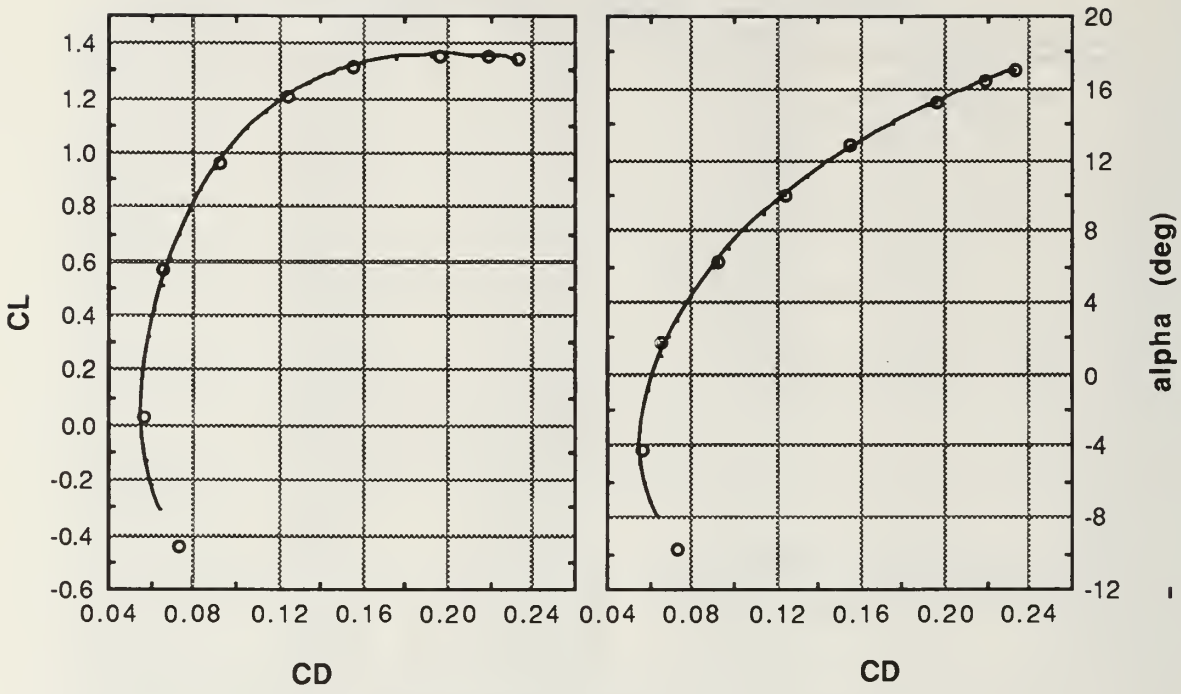

Figure 5.3 Drag Polar

Figure 5.3 shows that the minimum drag was at an angle of attack of -4 degrees which was close to the Pioneer RPV's zero lift angle of attack of -4.6 degrees.

The drag coefficient is often approximated by the parabolic approximation

$$C_D = C_{D_o} + \frac{C_L^2}{\pi e A} \tag{5.2}$$

Equation 5.2 can be used to simplify performance calculations by separating the drag into parasite (profile, friction and pressure drag) and induced (lift related) components. The effect of configuration changes can then be calculated by changing C_{Do} (by the incremental change due to the configuration change) in

Equation 5.2 to reflect the new zero-lift drag. All performance calculations in this report used actual values for the lift and drag coefficients and were not calculated using Equation 5.2. Equation 5.2 is provided for comparison purposes and to aid calculations of future configuration changes. Equation 5.2 is only valid for the Pioneer RPV at moderate angles of attack (less than 6°) where there is no large separation of airflow over the air vehicle.

C_{Do} is the zero lift parasite drag coefficient of the air vehicle. The Oswald efficiency factor (e) in Equation 5.2 would be equal to 1.0 for an airfoil with an elliptic lift distribution, which has been found to produce the smallest induced drag due to lift. The values for Equation 5.2 were found by plotting $C_L{}^2$ versus C_D in the linear region as shown in the right half of Figure 5.4. C_{Do} was determined to be 0.055, with an Oswald efficiency factor of 0.886.

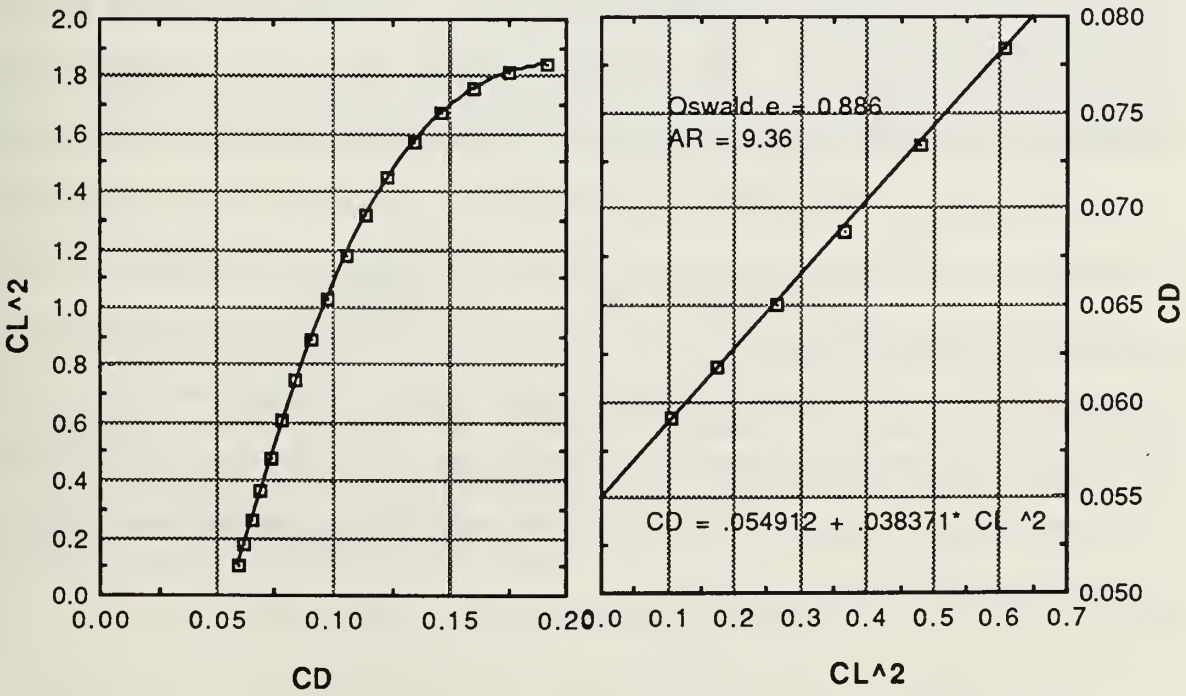

Figure 5.4 C_D versus $C_L{}^2$

The theoretical drag calculated by Equation 5.2 and its individual components were plotted in Figure 5.5 alongside the actual air vehicle drag measured in the wind tunnel for a 420-lb Pioneer RPV. Minimum drag occurs at only one airspeed (angle of attack). Flying faster or slower will create an increase in the drag of the aircraft. As the airplane's speed increases, the parasite drag (a sum of the friction drag and the form or pressure drag due to airflow separation at relatively low angles of attack) of the fuselage, wings, payload bubble etc., increases as the square of the speed. If the airplane's speed is decreased the parasite drag decreases, but both the induced drag (drag resulting from lift) and that portion of the form or pressure drag due to flow separation at high angles of attack increase rapidly as the aircraft's speed decreases (angle of attack increases).

Equation 5.2 was derived from and is only valid in the linear portion of CL^2 versus CD in Figure 5.4. This corresponded to the linear portion of the lift curve slope in Figure 5.2. The Oswald Efficiency Factor (e) of Equation 5.2 included the variation of parasite drag with lift at moderate angles of attack, but does not account for the sharp increase in drag and loss of lift due to airflow separation at high angles of attack. Figure 5.5 shows that Equation 5.2 has significant error outside of the linear region of the lift curve slope and therefore should not be used for drag predictions near the stall. A significant portion of the drag at high angles of attack is probably a result of flow separation instead of induced drag. Equation 5.2 should not be used for drag calculations at angles of attack greater than six degrees.

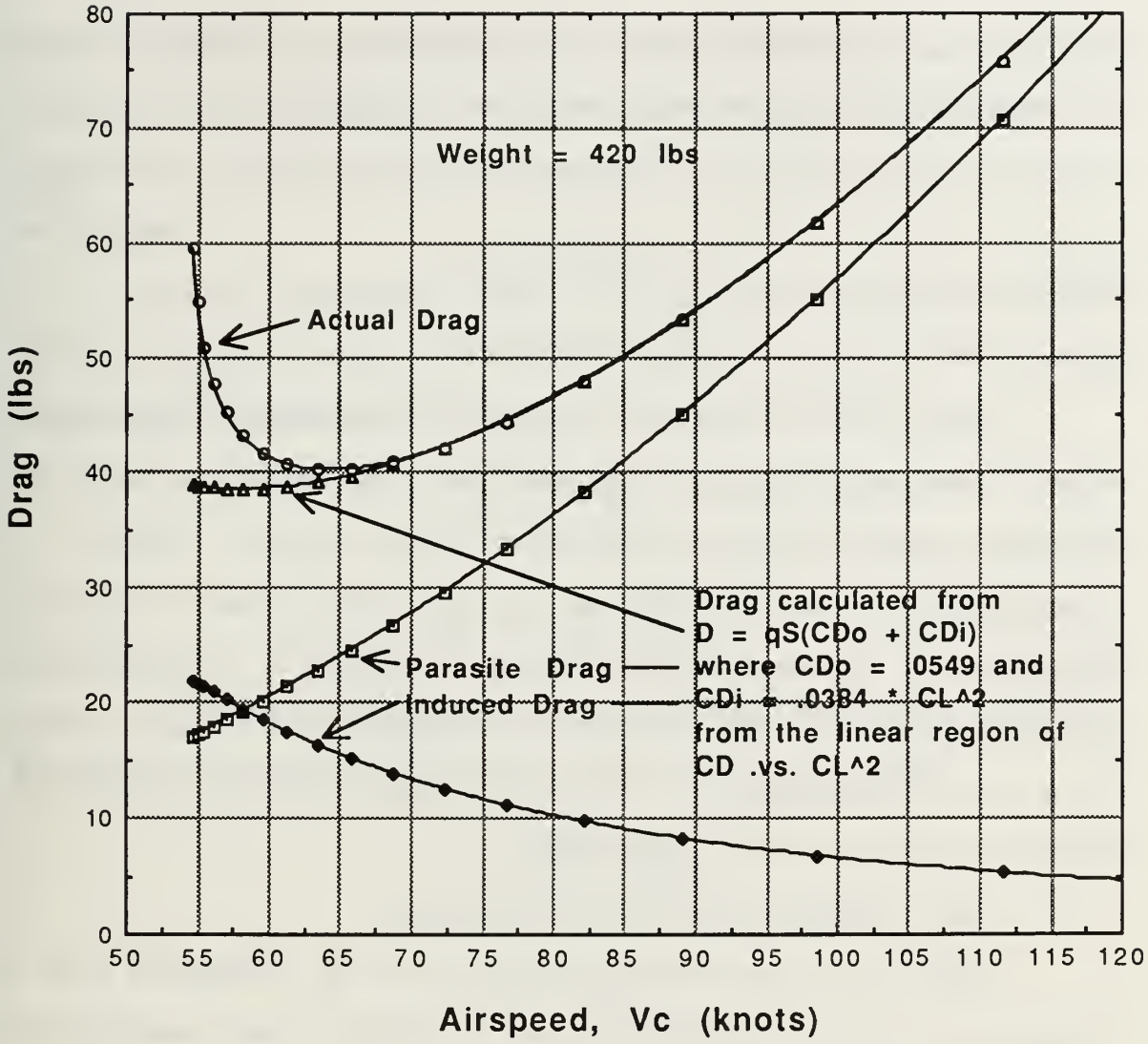

Figure 5.5 Drag at Sea Level

The mimimum drag and its corresponding velocity cannot be accurately calculated from the theoretical parabolic drag equation (Equation 5.2). Theoretically, the minimum drag would have occurred at the intersection of the induced drag and parasite drag.

The plots in figure 5.5 used the Pioneer RPV's actual trimmed lift coefficients for calculation of both the airspeed and the induced drag. It is interesting to note that a nearly identical curve for the induced drag would

result from use of the lift coefficients calculated from the Pioneer RPV's lift curve slope ($C_{L\alpha}$) in its linear region using the relationship

$$C_L = C_{L_\alpha}(\alpha - \alpha_{\text{zero lift}}) \tag{5.3}$$

with $$C_{L_\alpha} = 0.0834 / \text{deg}$$

and $$\alpha_{\text{zero lift}} = -4.6 \text{deg}$$

Using the lift coefficients calculated from Equation 5.3 results in a higher induced drag at high angles of attack due to the assumption that the lift coefficient increases linearly with increasing angle of attack. However, the corresponding airspeed calculated from the higher lift coefficient at angles of attack above the linear region of the lift curve slope results in a correspondingly lower airspeed to create the lift necessary to support the Pioneer RPV's weight. These two effects combine to give the same drag curves as using the air vehicle's actual measured lift coefficients.

3. Power Required and Power Available

Much of an airplane's performance can be determined from a comparison of power available with power required. Power available was calculated from the thrust available listed in the Naval Air Propulsion Center's (NAPC) Altitude Chamber Test Report [Ref. 17] of the installed Sachs SF 2-350, 26 hp engine using the relationship

$$P_{avail} = T_{avail} V_t \frac{1.6878}{550}$$

Plots of the power available show the actual data points calculated from the thrust listed in the NAPC test report. The power available data points were fit with polynomial curves. The thrust available listed in the NAPC test

report was from an engine installed on a Pioneer air vehicle with a 600-watt alternator load and turning a two-bladed, 29-inch propeller. The test was conducted in a pressurized cell enabling test runs at various density altitudes and airspeeds.

In level, unaccelerated flight, thrust equals drag and lift equals weight. These relationships enabled calculation of the power required from the wind-tunnel results as follows:

$$T_{req} = \frac{W}{C_L / C_D} \tag{5.4}$$

$$P_{req} = T_{req} V_t \frac{1.6878}{550} \tag{5.1}$$

Calibrated airspeed in knots was calculated by assuming a trimmed level flight condition with the lift equal to the weight. By definition

$$V_t = \sqrt{\frac{2W}{C_L \rho S}} \frac{1}{1.6878}$$

and

$$V_c \cong V_e = V_t \sqrt{\frac{\rho}{\rho_s}},$$

for the low-airspeed, low-altitude flight regime of the Pioneer RPV.

Therefore,

$$V_c = \sqrt{\frac{2W}{C_L \rho_s S}} \frac{1}{1.6878} \tag{5.5}$$

Equation (5.5) shows that calibrated airspeed does not vary with altitude.

Figures 5.6 to 5.8 show the power required and power available throughout the Pioneer's flight regime at various altitudes and weights. Maximum level flight velocity is the upper intersection where the power available equals the power required. The predicted maximum sea level flight

velocity of 104 knots for a 430-pound air vehicle agrees with the designer's published maximum airspeed [Ref. 18:p. 122]. Succeeding sections will describe various performance aspects that can be derived from knowledge of the power available and the power required.

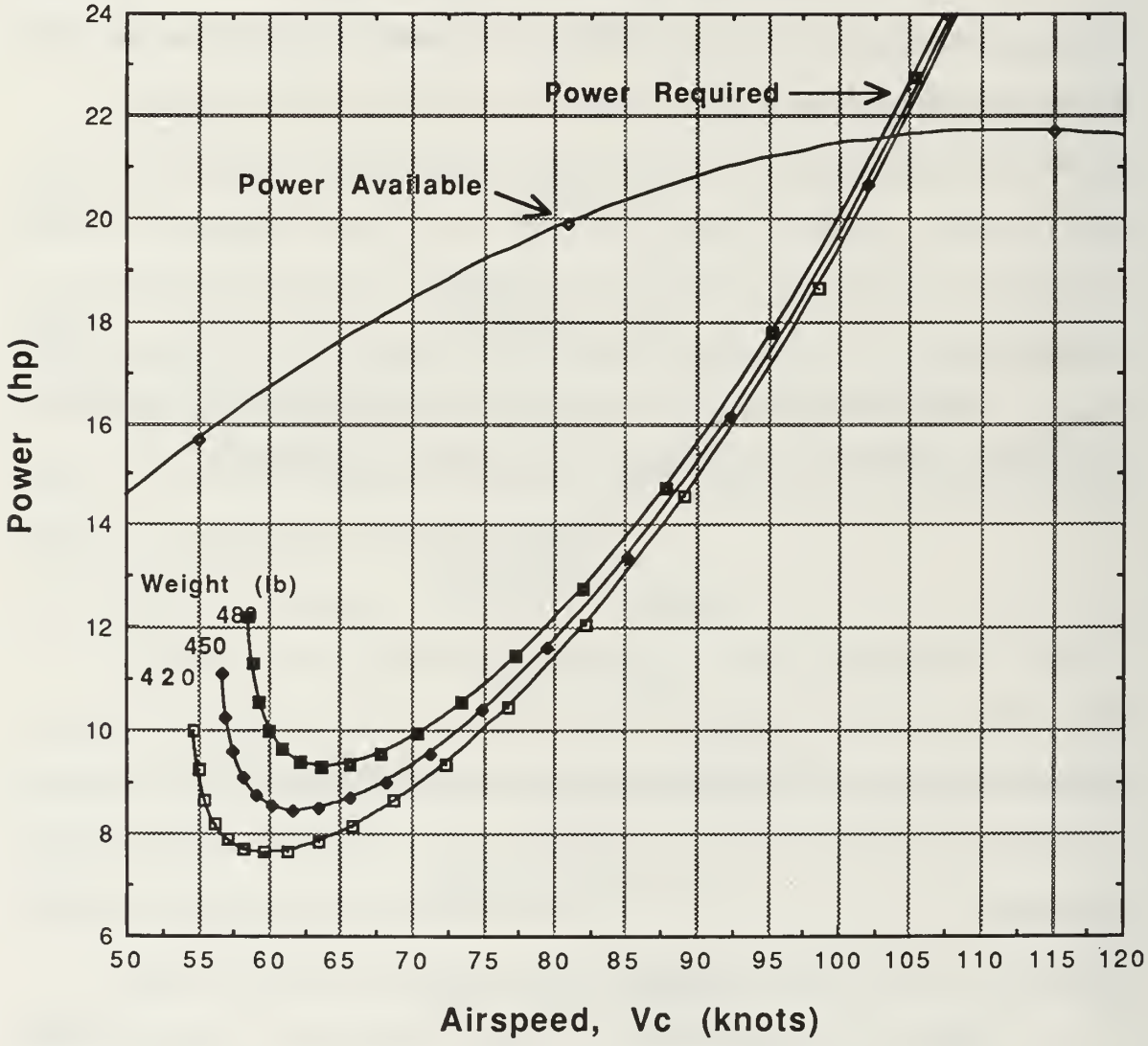

Figure 5.6 Power Curve (Sea Level)

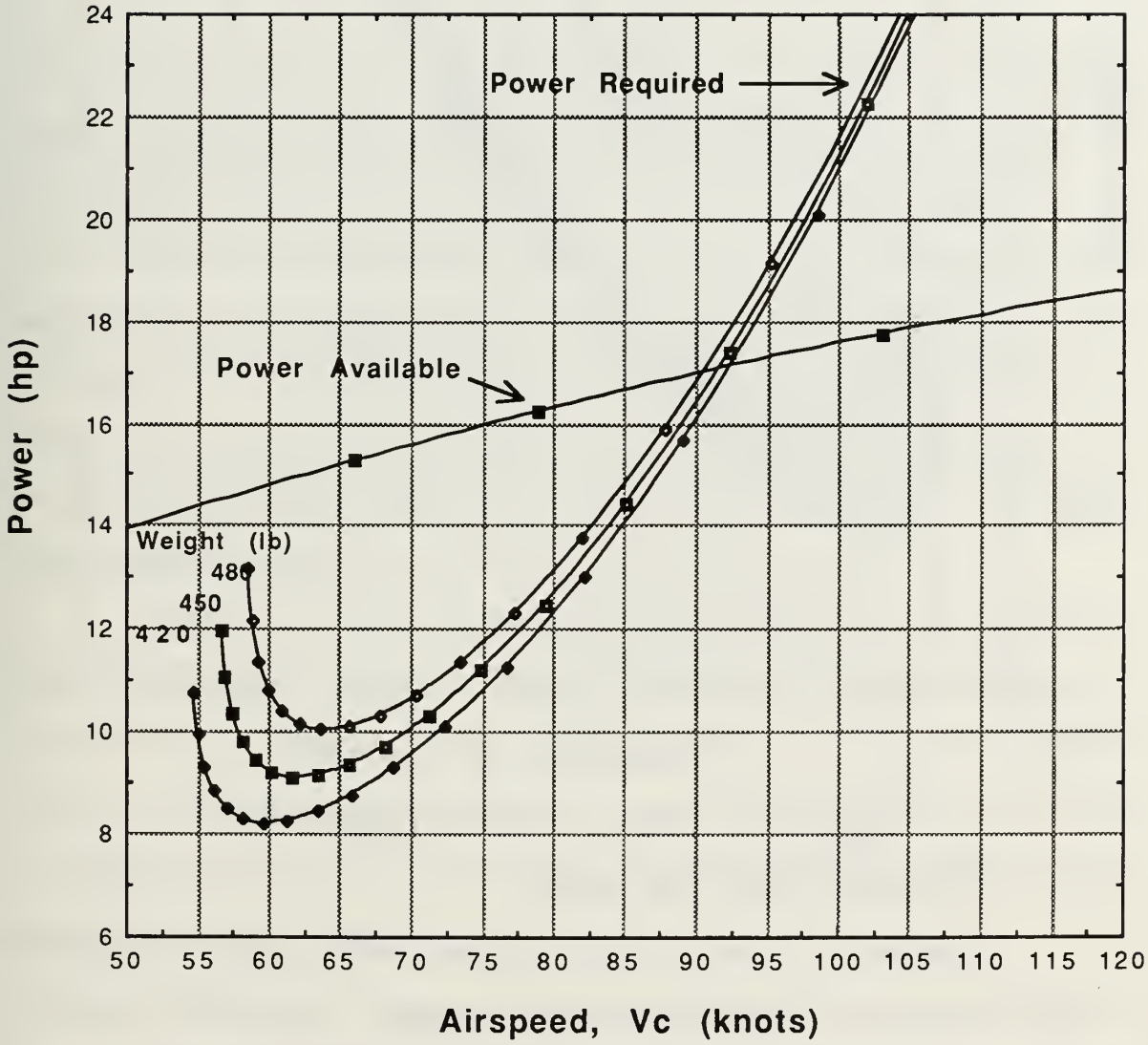

Figure 5.7 Power Curve (5000 Feet)

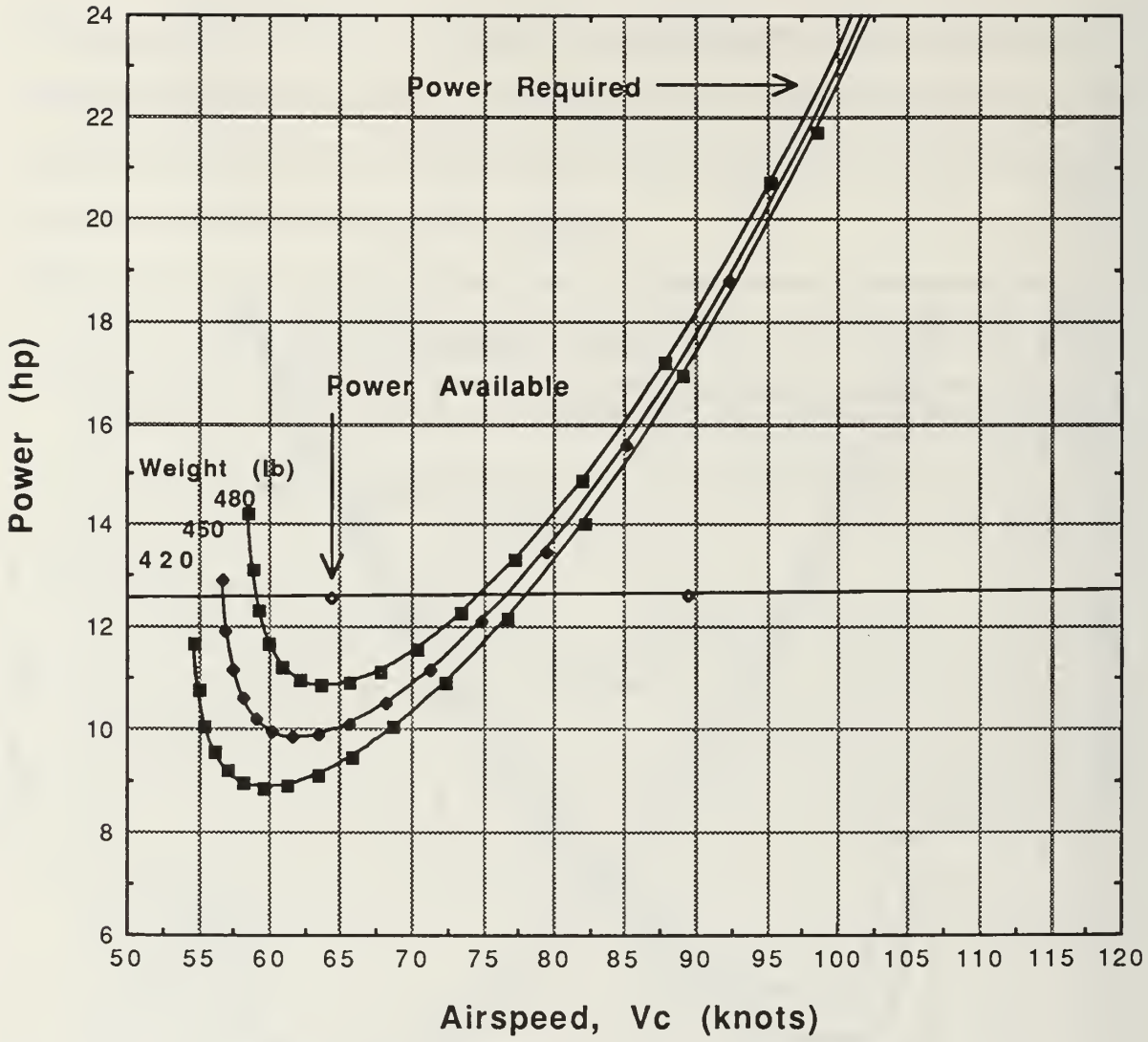

Figure 5.8 Power Curve (10000 Feet)

4. Maximizing Miles per Gallon

Equation 5.4 shows that the minimum thrust required for a given weight corresponds to the maximum lift to drag ratio. Additionally, maximum range for a propeller-driven aircraft occurs near a velocity such that C_L/C_D is a maximum. This can be shown as follows:

$$\frac{\text{lb of fuel}}{\text{distance}} \propto \frac{(SFC)P_R}{V_t} \propto T_{req} \propto \frac{1}{C_L / C_D}$$

where SFC is almost constant for normally-aspirated, reciprocating engines, and the propeller efficiency was assumed constant throughout the flight speeds of interest.

The classic formula for estimating range, the Breguet range formula

$$Range \propto \frac{\eta}{SFC}\frac{C_L}{C_D} \tag{5.6}$$

shows that range is maximized by optimizing a combination of C_L/C_D, propeller efficiency (η), and specific fuel consumption (SFC). [Ref. 19:pp. 304-307]

The maximum C_L/C_D occurs at only one angle of attack that corresponds to the minimum drag (minimum thrust required) of the aircraft (Equation (5.4)). Assuming that propeller efficiency and the specific fuel consumption do not vary over the range of flight speeds of interest, the maximum-range angle of attack for the Pioneer RPV is 6.5 deg at any aircraft weight or density altitude.

C_L/C_D, a measure of the aerodynamic efficiency of an aircraft, is plotted versus angle of attack in Figure 5.9 and versus calibrated airspeed in Figure 5.10. The maximum value of C_L/C_D of about 10.5 occurs at 6.5 degrees angle of attack regardless of air density. Power-off glide distance could easily be computed from this C_L/C_D information if the windmilling propeller was not creating any thrust or drag, since

$$\text{gliding distance} = \text{altitude}\frac{C_L}{C_D}$$

if gliding distance and altitude are in the same units. [Ref. 19:pp. 294-295]

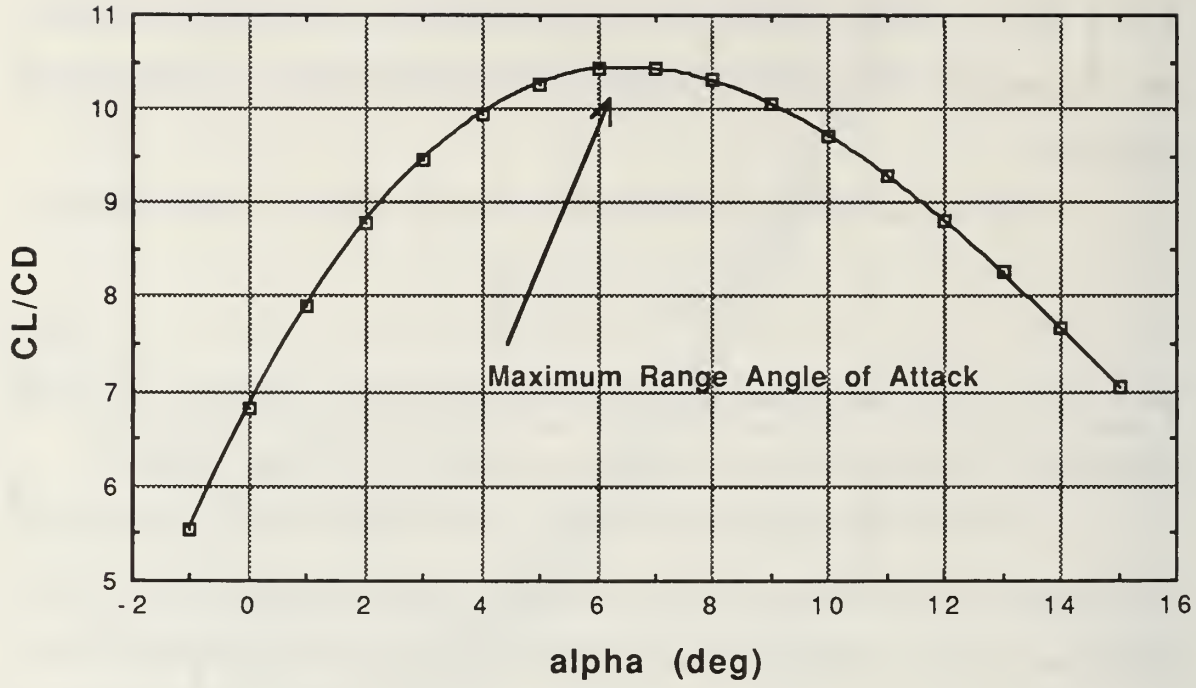

Figure 5.9 C_L / C_D versus Angle of Attack

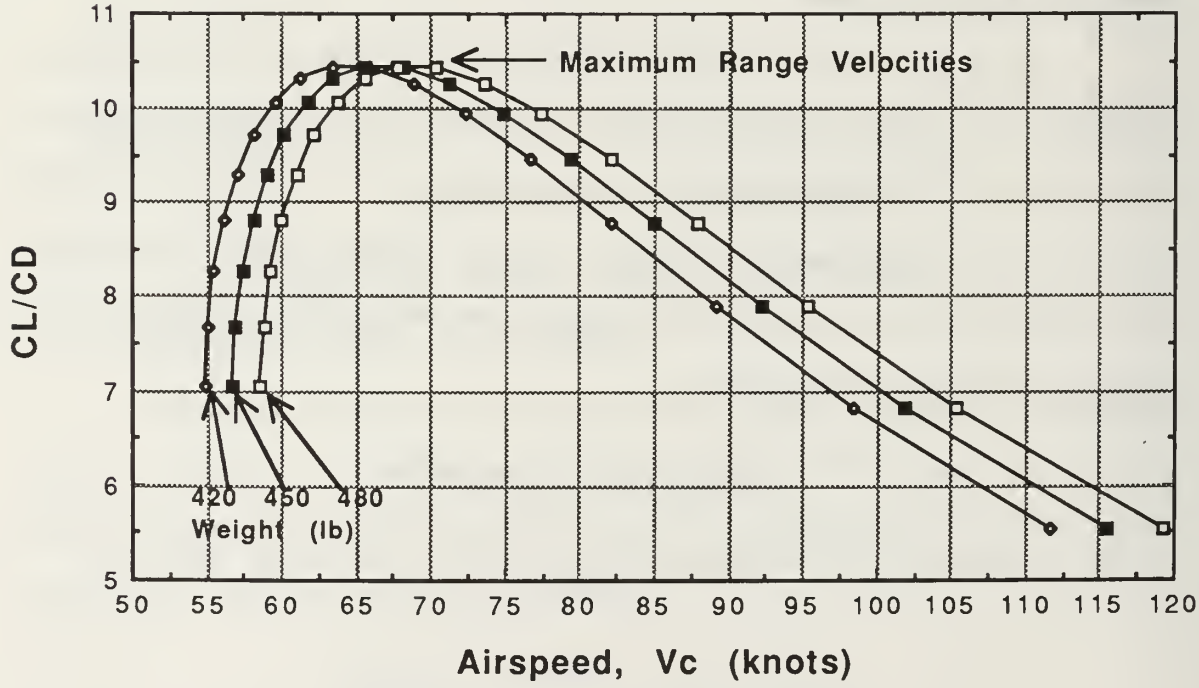

Figure 5.10 C_L / C_D versus Airspeed

5. Flight Endurance

Maximum endurance for a propeller-driven airplane occurs when the airplane is flying at its minimum power required, assuming that the specific fuel consumption is constant over the range of airspeeds of interest.

The maximum endurance airspeed is slower than the maximum range airspeed and at a correspondingly higher angle of attack. Flight endurance is a function of fuel consumption; fuel can be thought of as a store of potential energy. To maximize flight time we want to minimize fuel consumption per unit time by flying at the minimum power required, since

$$\frac{\text{gal of fuel}}{\text{hr}} \propto (SFC)P_{req}$$

and SFC is nearly constant for normally aspirated reciprocating engines.

Similar to the classical range calculations, endurance can be calculated using the classical Breguet endurance equation where

$$Endurance \propto \frac{\eta}{SFC}\frac{C_L^{3/2}}{C_D}\sqrt{\rho}$$

The Breguet endurance equation shows that maximizing endurance will involve optimizing a combination of $C_L^{3/2}/C_D$, propeller efficiency (η) and specific fuel consumption (SFC). Maximum flight endurance results from optimizing the above flight parameters at sea level. Endurance will be maximized at sea level since air density is the greatest at sea level, and

$$Endurance \propto \sqrt{\rho}$$

It is interesting to note, that unlike endurance, range was not directly dependent on altitude, but the true airspeed for maximum range did increase with altitude. [Ref. 19:p. 308]

The airspeed for maximum $C_L^{3/2}/C_D$ corresponds to the airspeed for minimum power required shown in Figures 5.6 through 5.8, since

$$P_R = T_{req} V_t = \frac{W}{C_L / C_D} \sqrt{\frac{2W}{C_L \rho S}} \frac{1}{1.6878}$$

resulting in

$$P_R \propto \frac{1}{C_L^{3/2} / C_D}$$

Since lift and drag coefficients are functions of angle of attack, minimum power required will occur at only one angle of attack. The maximum endurance angle of attack is 8.5 degrees regardless of the air vehicle's weight or density altitude. Figure 5.11 shows $C_L^{3/2}/C_D$ versus angle of attack, and Figure 5.12 shows $C_L^{3/2}/C_D$ versus calibrated airspeed.

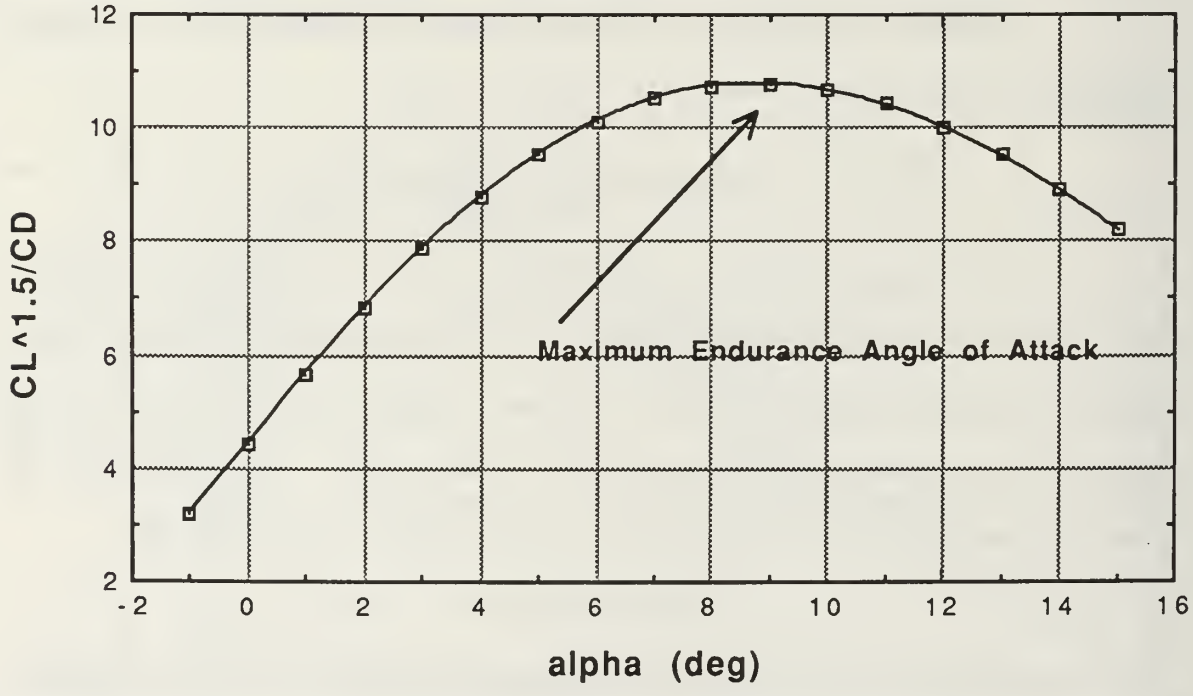

Figure 5.11 $C_L^{3/2} / C_D$ versus Angle of Attack

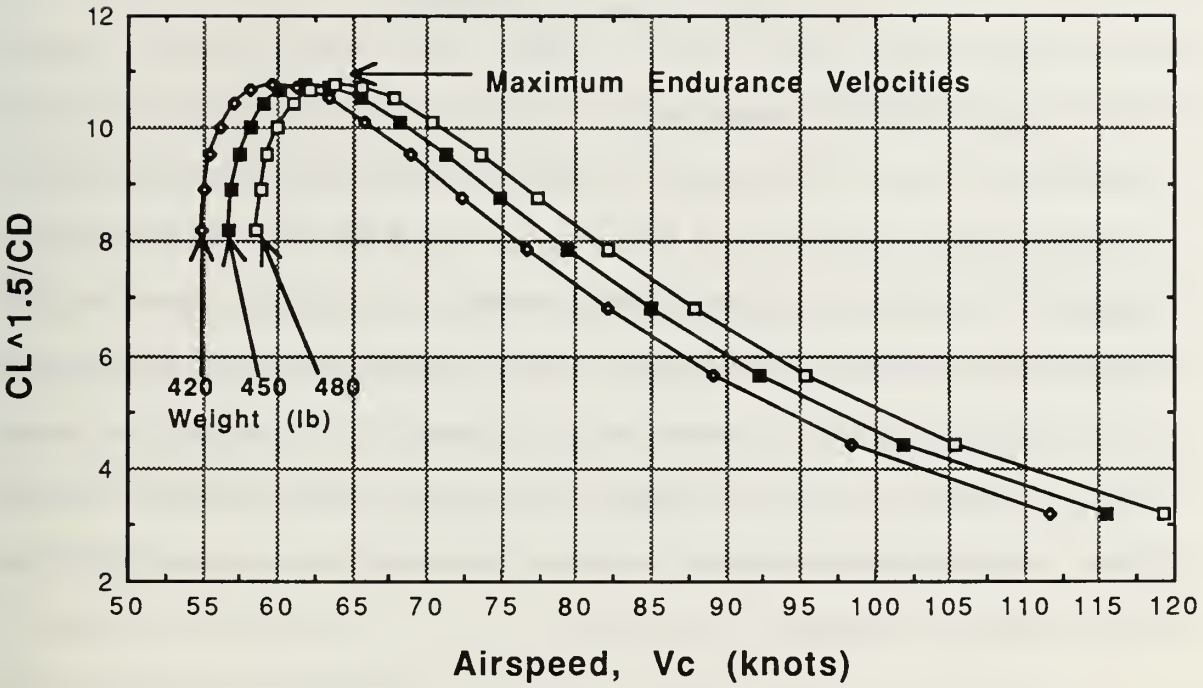

Figure 5.12 $CL^{3/2}$ / CD versus Airspeed

Rate of descent is also a minimum at the airspeed for minimum power required, since

$$\text{Rate of Descent} \propto \frac{C_D}{C_L^{3/2}} \sqrt{\frac{2W}{\rho}}$$

6. Rate of Climb

Rate of climb is important for determining time to climb, fuel used in a climb and the service ceiling of the aircraft. The maximum rate of climb airspeed would be used to minimize the time required to climb to a desired altitude. An aircraft's service ceiling is often defined as the altitude for which the rate of climb has been reduced to 100 fpm.

Rate of climb depends on the aircraft's excess power and weight:

$$R/C = \frac{(P_{avail} - P_R)550 * 60}{W} \tag{5.7}$$

[Ref. 19:pp. 287-289]. Equation 5.7 indicates that if the propulsive power available for thrust was constant over the aircraft's speed range, then the maximum rate of climb would occur at the speed for the minimum power required. The Pioneer's actual speed for the best rate of climb is faster than the speed for minimum power required. The engine cannot produce maximum power available for thrust at slow airspeeds due to a combination of lower propeller efficiency and the inability of the engine to produce full rpm. Excess power is the difference between power available and power required curves at a given airspeed in Figures 5.6 through 5.8.

Equation 5.7 shows that one way to increase the aircraft's rate of climb is to reduce the weight of the aircraft. The rate of climb could also be increased by increasing the power available by use of a more powerful engine. The use of a more powerful engine would add weight due both to the added weight of the larger engine and the stronger aircraft structure necessary to support the more powerful and heavier engine. Reducing the airframe drag would be another approach to decreasing the power required.

Rate of climb decreases with altitude, since both the power available decreases and the minimum power required increases. Climb rates for sea level and 10,000 feet are shown in Figure 5.13. These rates of climb assume power available calculated from the thrust available given in the Naval Air Propulsion Center test report of the 26 hp Sachs engine at sea level and 10,000 feet [Ref. 17]. Figure 5.14 shows the maximum rates of climb, extrapolated from the data points shown, as functions of altitude. Actual engines may

produce less propulsive power due to wear with age, lower propeller efficiency, or an increased alternator load. Rates of climb are significantly lower on hot days due to the increased density altitude (i.e., lower air density than for the standard atmosphere at a given altitude).

7. Angle of Climb

Angle of climb is important for obstacle clearance purposes. Flying at the best angle-of-climb speed will result in the best altitude gain in the shortest distance traveled. The best angle-of-climb speed is slower than the best rate-of-climb speed and will result in a lower rate of climb than the optimum. Angle of climb versus airspeed is shown in Figure 5.15. The altitude gained in a given distance is calculated by

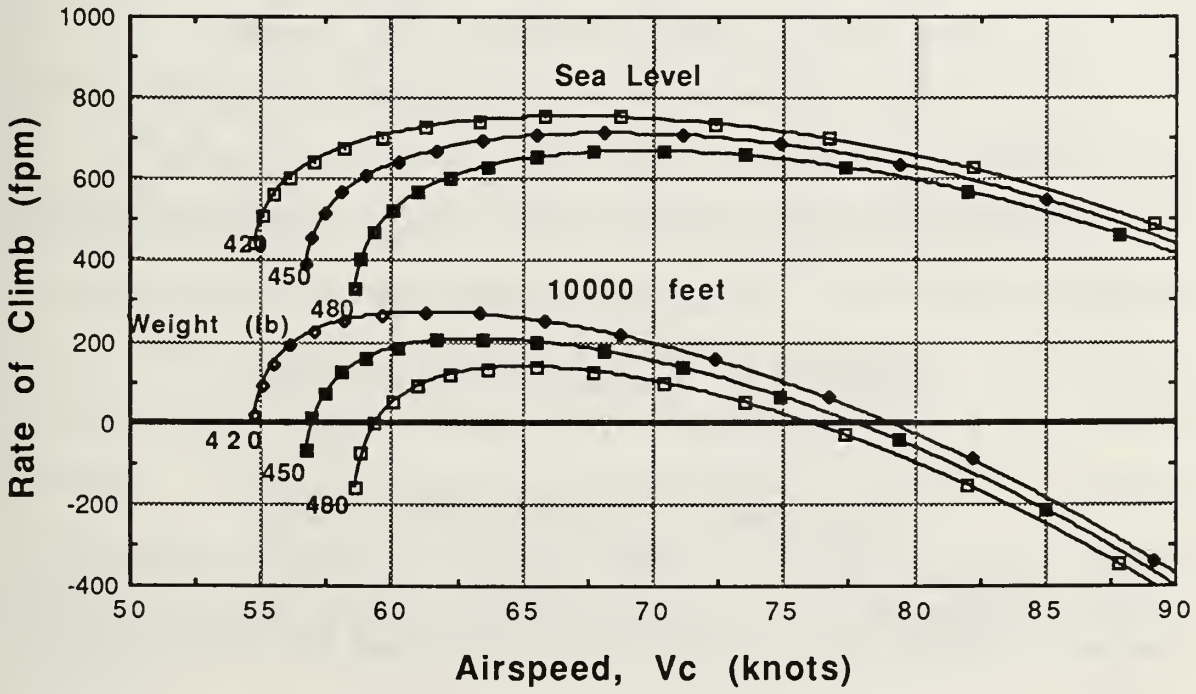

Figure 5.13 Rate of Climb

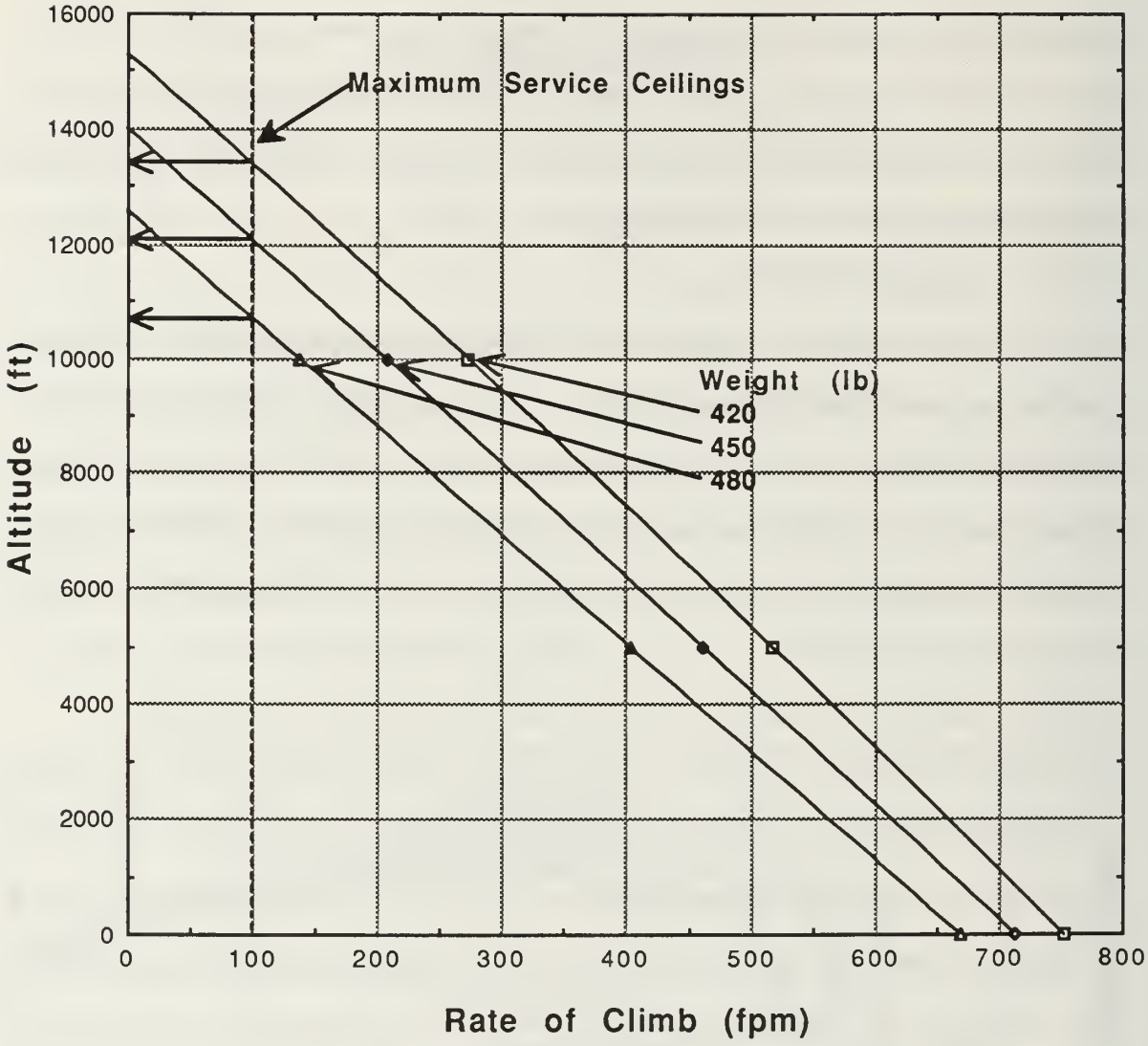

Figure 5.14 Maximum Rate of Climb

$$\text{Verticle Distance} = \text{Horizontal Distance} * \tan\gamma$$

with γ taken from Figure 5.15 at the applicable speed. Just as rate of climb decreases with altitude, the angle of climb will decrease with density altitude as well.

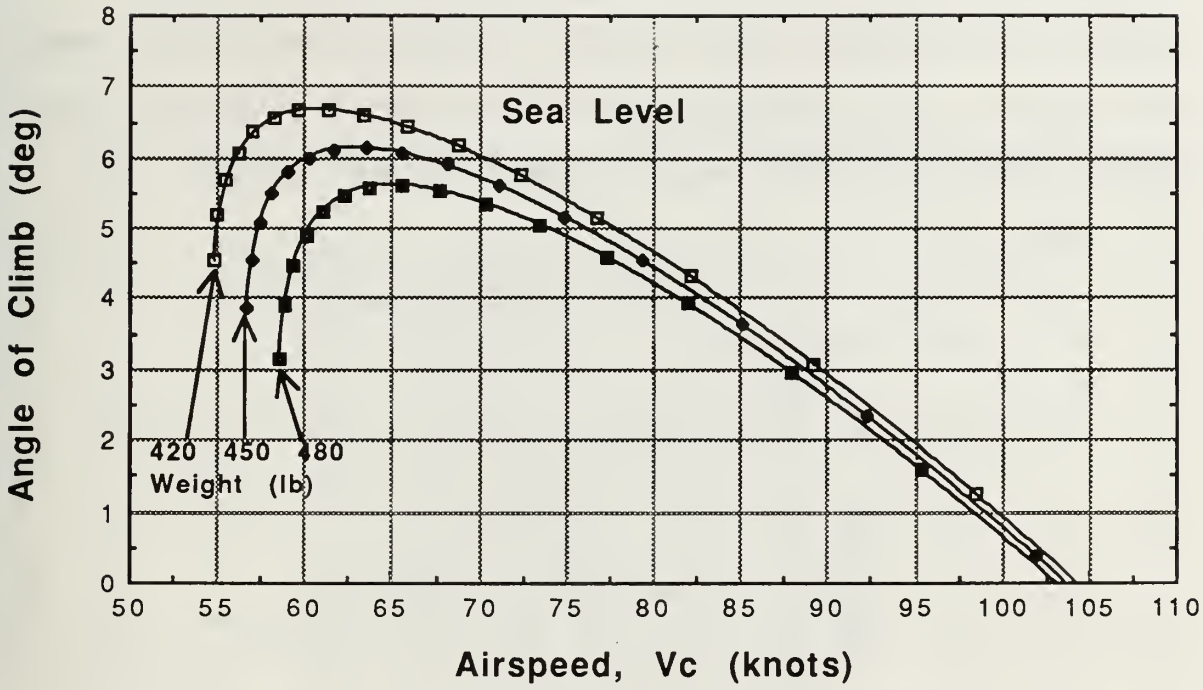

Figure 5.15 Angle of Climb at Sea Level

8. Crosswind Capability

Rudder power of the Pioneer RPV is important for determining its crosswind capabilities. Rudder deflection creates a side force that produces a yawing moment about the aircraft's center of gravity. If the rudder deflection is held, a sideslip develops such that the total yawing moment of the aircraft returns to zero. Figure 5.16 plots the sideslip developed for a given rudder deflection. It should be noted that the rudder loses the authority to increase sideslip when deflected more than 15 degrees. The rudder yaws the aircraft 0.780 degrees per degree of rudder deflection up to 15 degrees of rudder deflection.

This simplified analysis ignores the restoring rolling moment due to the sideslip that must be compensated for by an aileron deflection. This aileron

deflection in turn would create an adverse yaw that would change the equilibrium sideslip angle. This simplified analysis is acceptable since only a few degrees of aileron deflection would be necessary to counter the Pioneer RPV's relatively small rolling moment developed due to the sideslip.

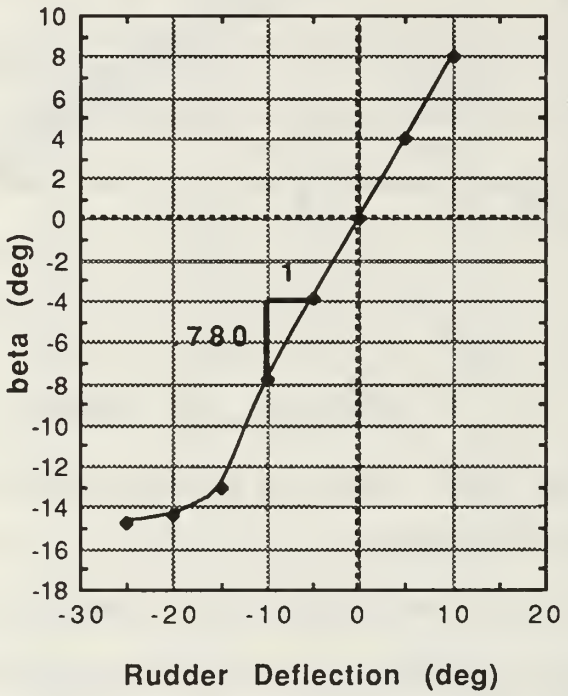

Figure 5.16 Sideslip versus Rudder Deflection for Zero Yaw Moment

Crosswind limitation can be defined by the ability of an aircraft to track the runway centerline in a crosswind during the landing approach. Nosewheel steering should be sufficient to counter the yawing moment created from a crosswind while the aircraft is firmly on the ground. Figure 5.16 shows that the Pioneer RPV can effectively hold a 13-degree sideslip with a 15-degree rudder deflection. The Pioneer RPV's maximum crosswind capability for a crosswind at 90 degrees to the runway centerline was calculated for this 13-degree

sideslip at approach speeds ranging from 50 to 90 knots, and plotted in Figure 5.17.

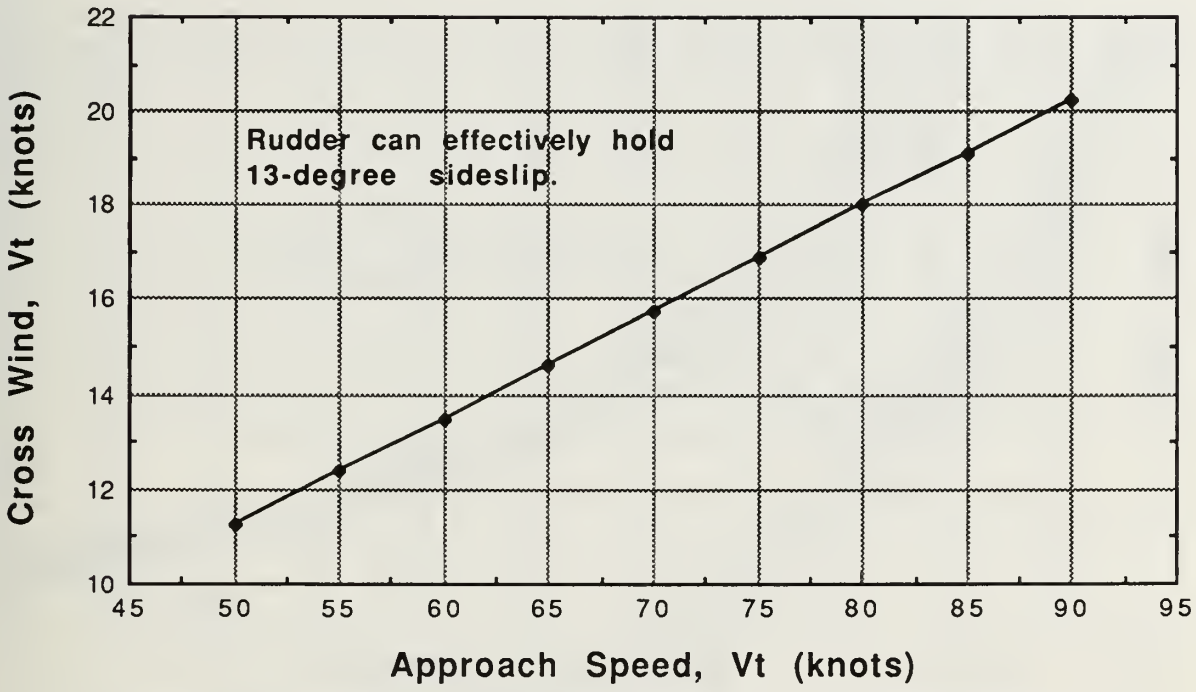

Figure 5.17 Crosswind Limitation versus Approach Speed

9. Airspeed Versus Angle of Attack

For a given aircraft weight and configuration, angle of attack controls airspeed. As the aircraft slows down, a higher angle of attack is necessary to produce sufficient lift to support the weight of the aircraft. By Equation 5.5

$$V_c \propto \sqrt{\frac{W}{C_L}}$$

and C_L is solely a function of angle of attack and was listed in Table 5.1.

For ease of comparison of predicted performance versus angle of attack (which doesn't vary with aircraft weight) to their corresponding

airspeeds, Figure 5.18 shows the angle of attack versus calibrated airspeed for various weights.

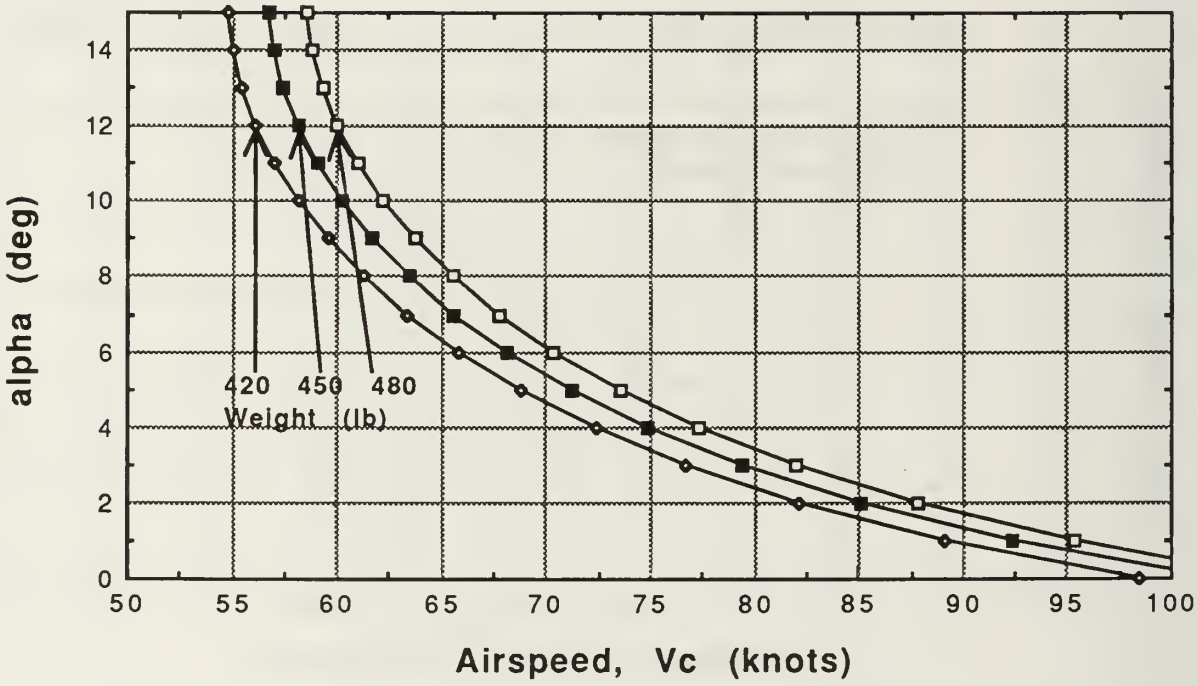

Figure 5.18 Angle of Attack versus Airspeed

D. DRAG OF EXTERNAL COMPONENTS

Minimizing drag is a design criterion that directly affects performance. Wind-tunnel runs were made to measure the drag contribution of the Pioneer RPV's large external components by successively removing items between runs. The payload bubble and shield, directional antenna and landing gear comprise over 35% of the Pioneer RPV's drag. Figure 5.19 shows the Pioneer RPV's drag coefficient versus angle of attack for consecutive runs after successive removal of external items. Table 5.2 list the drag counts (1 drag count is a C_D = .0001) of external items at a typical flight angle of attack of 6.5

degrees. Drag counts are also listed for zero angle of attack to facilitate calculations using Equation 5.2.

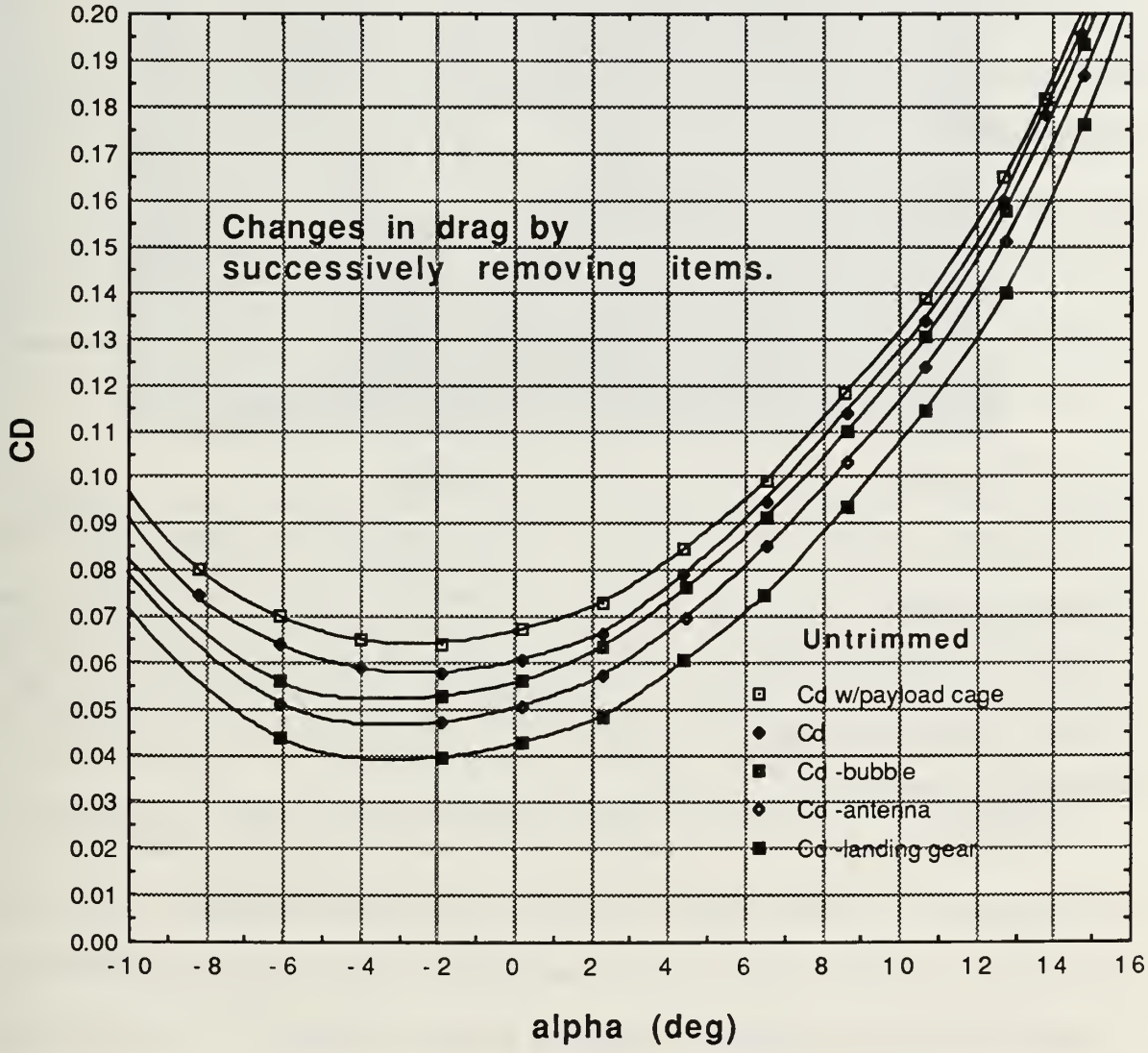

Figure 5.19 Drag Buildup (Untrimmed)

TABLE 5.2 DRAG COUNTS OF SELECTED ITEMS

Item	0 degrees AOA	6.5 degrees AOA
directional antenna	53	63
proposed directional antenna	56	65
payload bubble	45	33
payload shield	66	47
landing gear	80	103
saddlebag fuel tank	33	35

Drag Count = .0001

E. PROPOSED EXTERNAL FUEL TANKS

External conformal fuel tanks have been proposed as an option to increase flight endurance of the Pioneer RPV. These fuel tanks would provide an additional 18 liters of fuel to the Pioneers current 42-liter fuel capacity. These bolt-on fuel cells are attached to the sides of the fuselage below the wing as shown in Figure 5.20.

The drag increase due to attachment of these external fuel cells was 35 drag counts at 6.5 degrees angle of attack, which though significant, is less than the drag of any of the other external attachments (Table 5.2). The untrimmed drag coefficient versus angle of attack is plotted in Figure 5.21 both with and without the external fuel tanks.

Maximum lift coefficient decreased by only .02 and is plotted versus angle of attack in Figure 5.22.

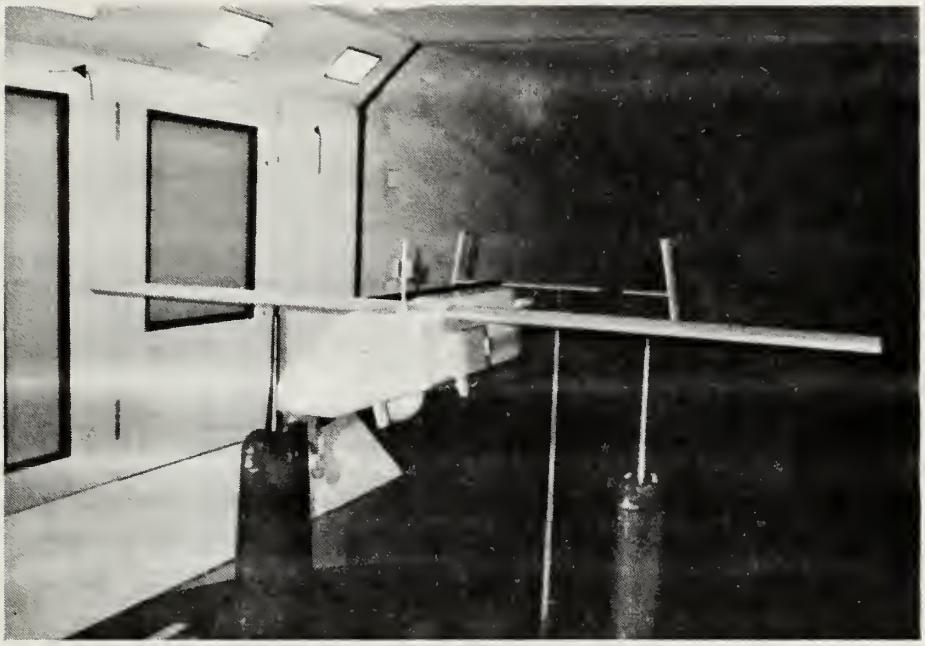

Figure 5.20 Pioneer RPV with Conformal External Fuel Tanks

Aerodynamically, the performance degradation is small for this increased fuel carrying capacity. The main performance degradation would result from the increased fuel weight requiring flight at faster speeds or higher angles of attack resulting in increased fuel consumption. Flying at weights above the Pioneer RPV's original design weight degrades its performance significantly.

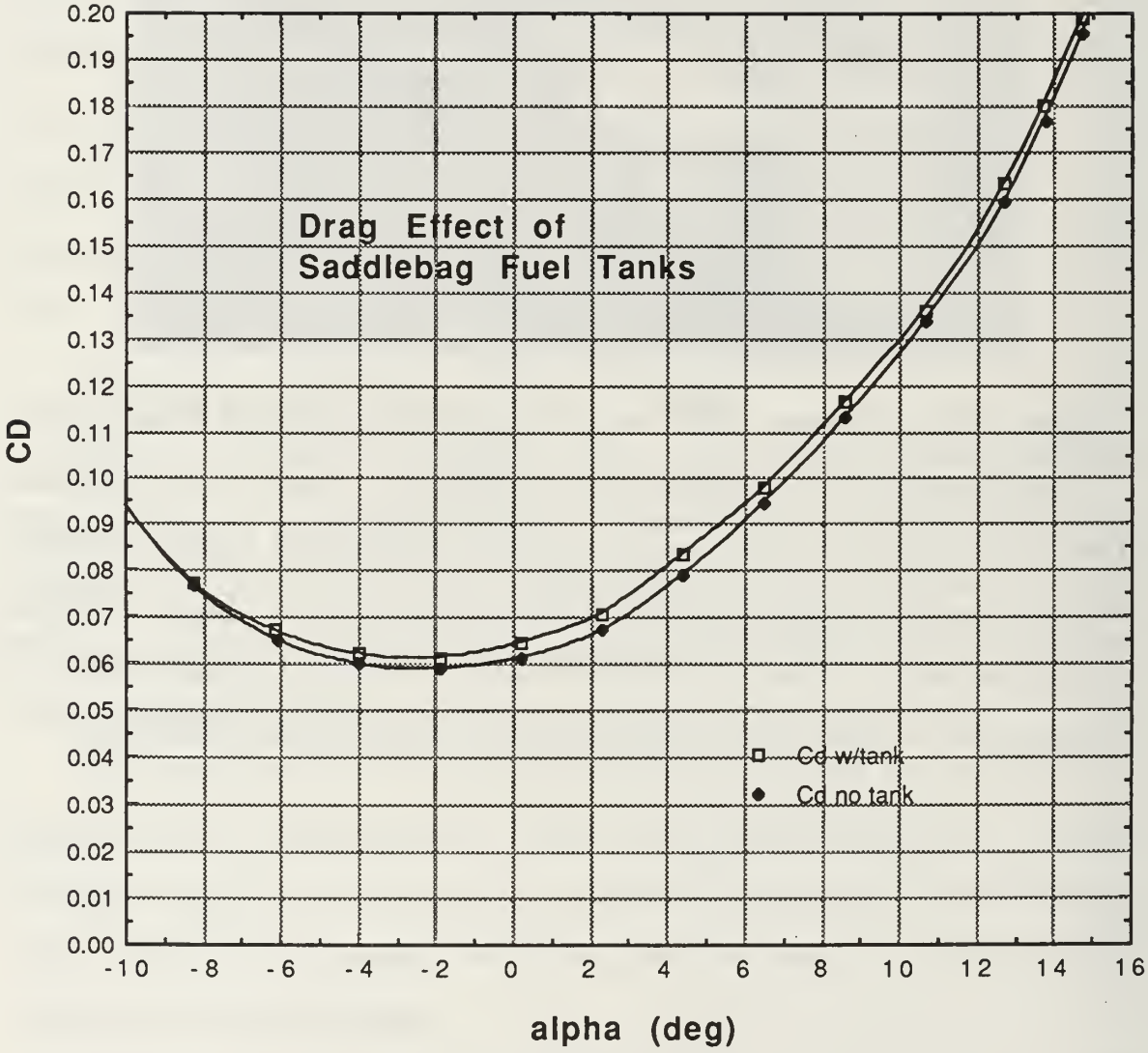

Figure 5.21 Drag Comparison of External Fuel Tank

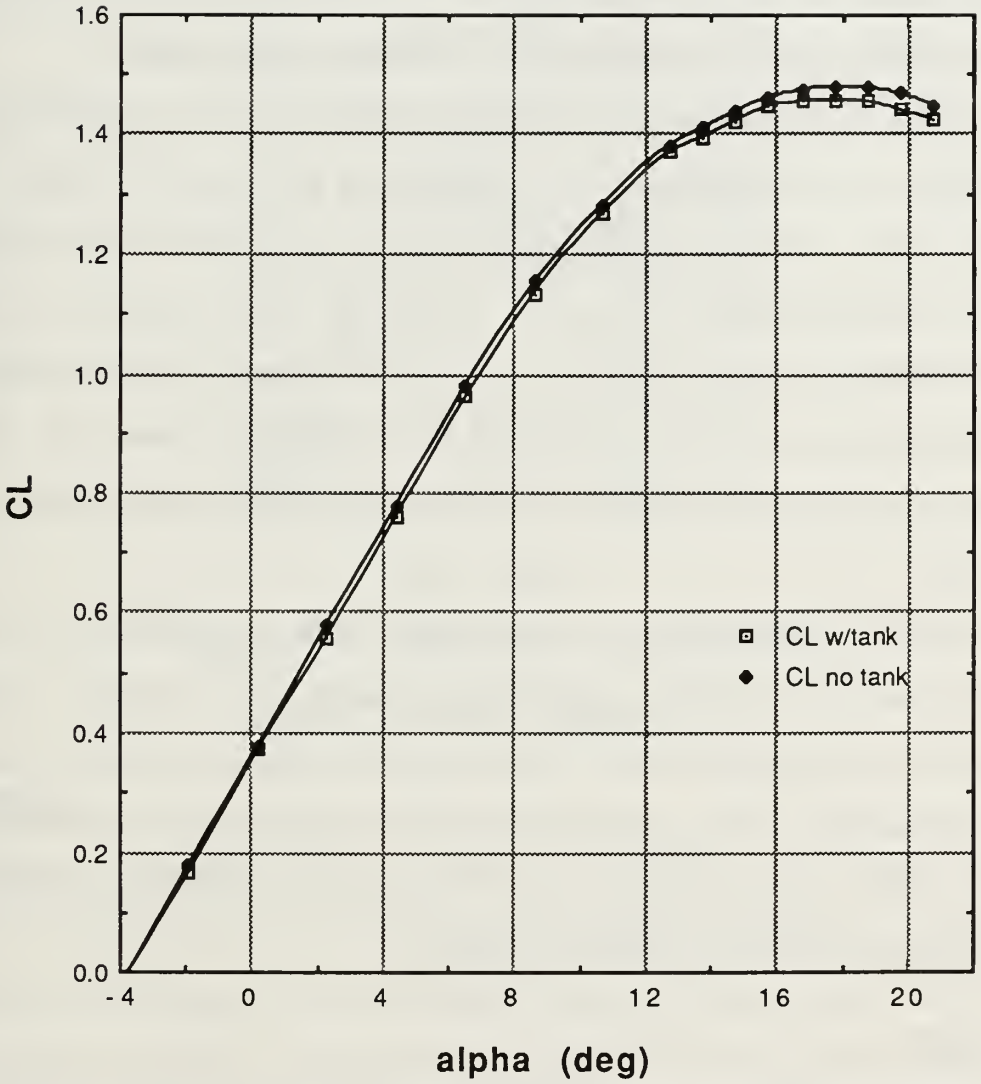

Figure 5.22 Change in Lift with External Fuel Tank

VI. COMPARISONS WITH PREVIOUS STUDIES

Several studies of the Pioneer RPV have been undertaken at the Naval Postgraduate School, Monterey, California. Results from the wind-tunnel test were compared with the results from the following three studies.

A study was conducted using a half-scale Pioneer RPV to predict the flight behavior of the full-scale aircraft. Engine rpm was recorded onboard with a small recorder. Thrust was determined by using propeller thrust coefficient curves determined from wind-tunnel testing and the recorded rpm. Airspeed was determined by timing runs over a 1500-foot course in both directions, while holding heading and allowing the plane to drift with any crosswind. Lift was determined from the test weight. Flight Reynolds numbers were about 500,000. [Ref. 20]

An aerodynamic analysis of the Pioneer RPV was conducted by Lyons [Ref. 2] using a low-order potential-flow panel code, PMARC. He also performed a drag analysis of the vehicle using a component-build-up approach.

Lift and drag coefficients for the full-scale vehicle are from Reference 20. These lift and drag coefficients were extracted from idle-power glide tests by assuming no residual thrust from the engine.

A. LIFT

Untrimmed lift curves are shown in Figure 6.1. The slope of the lift curve calculated by the PMARC panel code agrees closely with the slope of the lift curve from wind-tunnel testing at 6 degrees angle of attack. The numerical

prediction did not predict a maximum lift coefficient or the change in the lift curve slope with angle of attack.

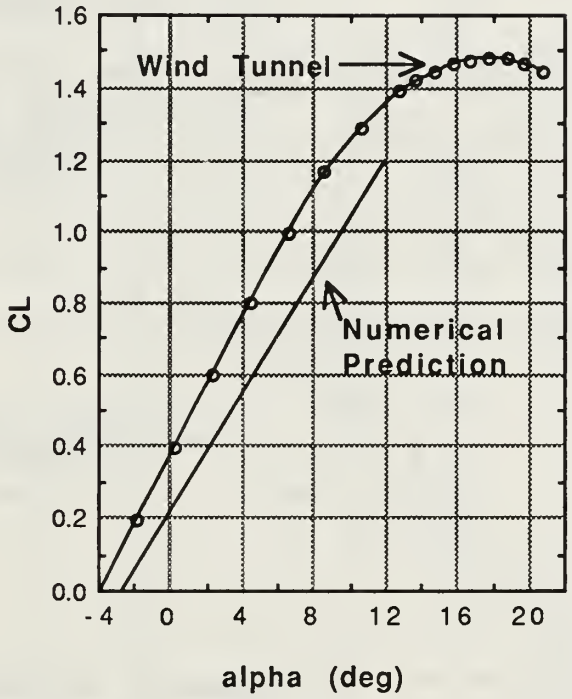

Figure 6.1 Lift Curve Comparison (Zero Elevator Deflection)

B. DRAG

Figure 6.2 compares the drag polars predicted by each of these methods. The drag extracted from full-scale glide tests agrees with that acquired from the wind-tunnel testing at lift coefficients where the NAPC engine tests [Ref. 17] recorded zero thrust. At high lift coefficients the drag extracted from full-scale glide tests is less than the drag measured from wind-tunnel testing. The most probable cause of this disparity is the residual thrust produced by the Pioneer RPV's idling engine. The assumption of zero residual thrust produces

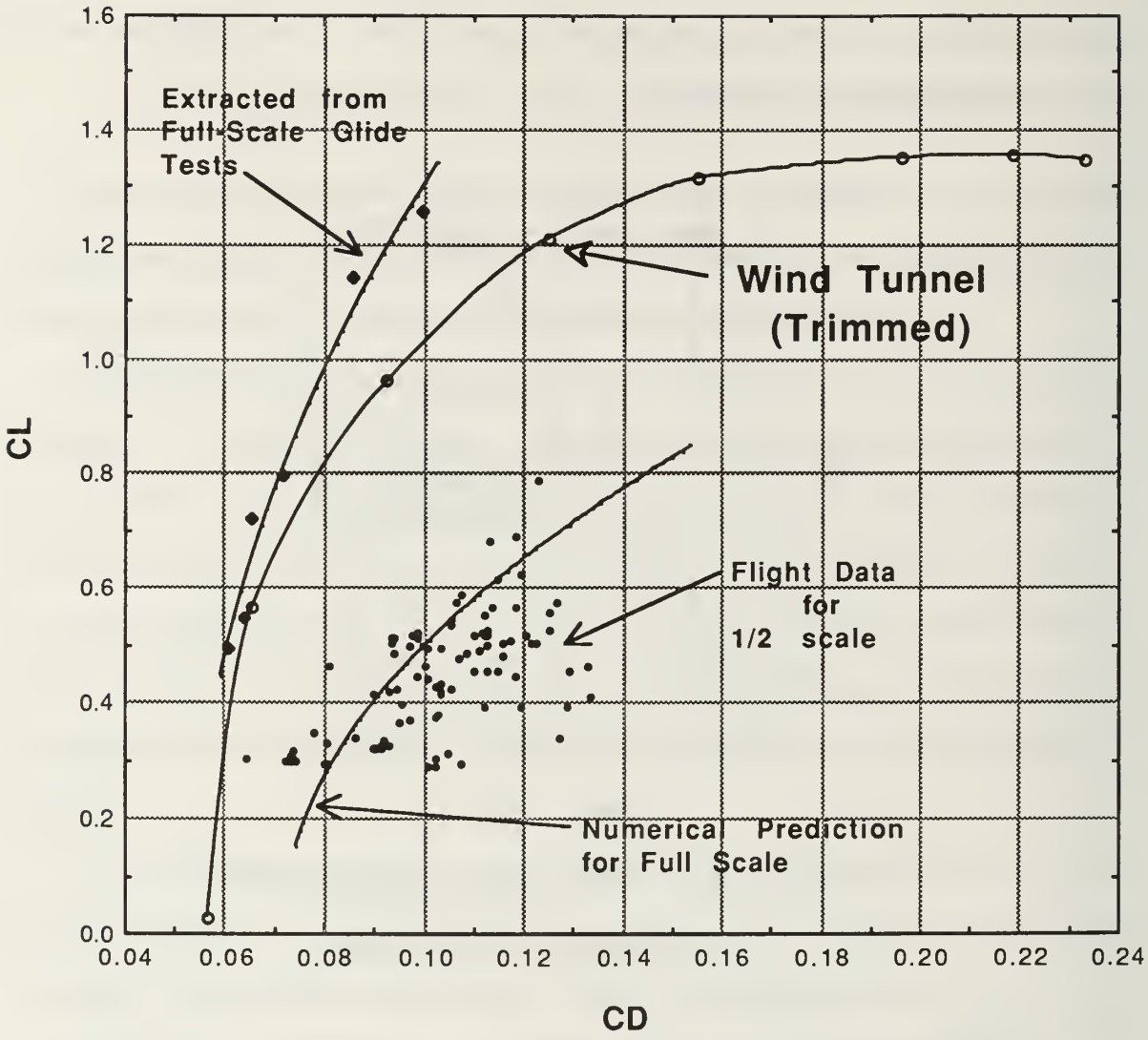

Figure 6.2 Drag Comparison

unrealistically low drag coefficients at high lift coefficients. Installed engine tests conducted by the Naval Air Propulsion Center (NAPC) recorded residual thrust at high angles of attack (low airspeed). The numerically predicted drag and the drag extracted from half-scale flight tests are much higher than the drag measured in the wind tunnel. The maximum L/D of 5.5 predicted by numerical methods is much less than the maximum L/D of 10.5 measured in the

wind-tunnel test. Limitations to the use of panel codes for the prediction of induced drag are discussed in Reference 20.

C. LONGITUDINAL STABILITY

Pitching moment coefficient versus angle of attack and the effect of elevator deflection are shown in Figure 6.3. The longitudinal static stability was predicted by Lyons using numerical methods [Ref. 2]. The longitudinal static stability agrees closely with that measured in the wind tunnel at moderate angles of attack as evidenced by the slope of the pitch moment curves in Figure 6.3. Pitch control power (change in pitching moment due to elevator deflection) was also accurately predicted.

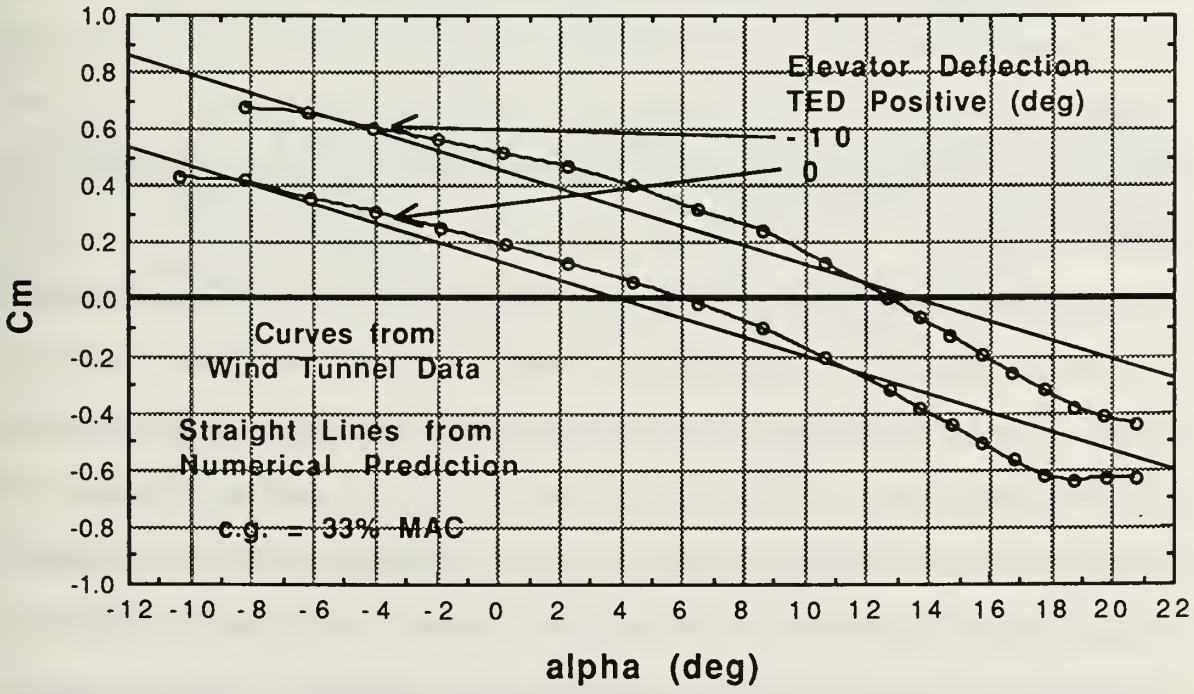

Figure 6.3 Pitching Moment Coefficient Comparison

The stick-fixed neutral point of the Pioneer RPV was a strong function of angle of attack. As was shown in Figure 4.9, the stick-fixed neutral point is between 60% and 65% MAC for relatively small angles of attack (less than 4 degrees). Above 4 degrees angle of attack the stick fixed neutral point moves aft at an increasing rate with increasing angle of attack. A constant stick-fixed neutral point of 74% MAC was calculated using the PMARC computer code [Ref. 2]. The Pioneer wind-tunnel test calculated a stick-fixed neutral point of 74% MAC at approximately 5 degrees angle of attack.

D. RUDDER POWER

Sideslip due to rudder deflection predicted by Lyons [Ref. 2] matched the wind-tunnel results perfectly in the linear region of sideslip versus rudder deflection (Figure 6.4). However, the crosswind capabilities predicted by Lyons were unrealistically high. He predicted a maximum sideslip angle of 18°, as opposed to the value of 13° determined from the wind-tunnel tests. Of course, his methods failed to account for the non-linear effects of separating flow over the tail surface.

This apparently good prediction of sideslip produced by rudder deflection cannot be explained. It was calculated from two control coefficients that differ from the values calculated from the wind-tunnel data by factors of 2 to 3. Table 6.1 lists the yawing moment coefficients due to both rudder deflection and sideslip predicted by the PMARC panel code and used to determine the sideslip where the yawing moment would be equal to zero for a given rudder deflection. Apparently, compensating errors prevailed in determining the ratio of directional coefficients.

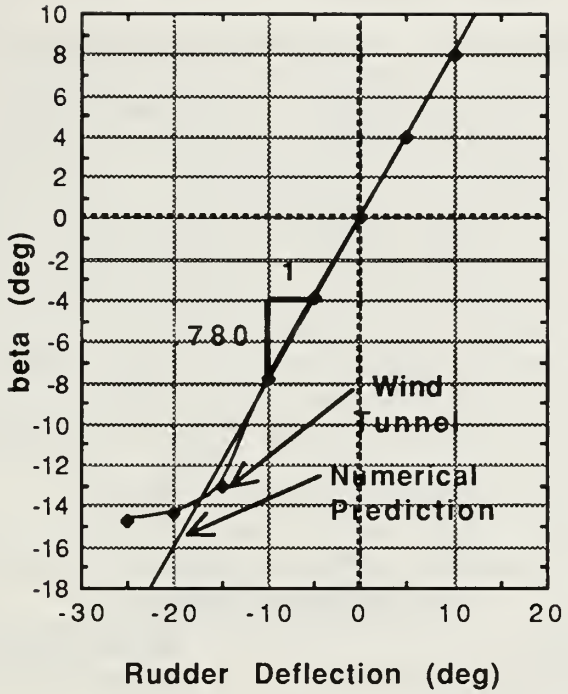

Figure 6.4 Sideslip Produced by Rudder Deflection

TABLE 6.1 PIONEER RPV DIRECTIONAL COEFFICIENTS

Name	Description	Wind Tunnel	PMARC
$Cn_{\delta r}$	yaw control power	-.0917	-.2464
Cn_{β}	weathercock stability	.109	.3151

E. STABILITY AND CONTROL COEFFICIENTS

The stability and control coefficients from the wind-tunnel test are compared with those predicted from the PMARC panel code and listed in Table 6.2. The numerical predictions of longitudinal coefficients did not vary with angle of attack. The directional coefficient predictions were calculated at 7° angle of attack with 5° up elevator (lift coefficient equal to 0.92).

The longitudinal coefficients agree very closely with the exception of the drag due to elevator deflection. This result is not surprising, since the drag due to elevator deflection varies significantly with angle of attack.

The directional coefficients vary significantly. One possible reason for this difference is that the compiled PMARC program has an upper limit of 5000 panels. Only half of the vehicle was modeled with the assumption that the sidewash due to the fuselage would have a negligible effect on the vertical tail surfaces. The analysis was performed using the combined effects of the components alone with no sidewash correction. [Ref. 2]

TABLE 6.2 PIONEER RPV STABILITY AND CONTROL COEFFICIENTS

Name	Description	Wind Tunnel	PMARC
S	surface area of wing, ft^2	30.42	
b	wingspan, ft	16.90	
c	chord, ft	1.80	
A	wing aspect ratio	9.4	
W	gross weight, lbs_f	420	
α	angle of attack (fuselage), deg	6	
V	velocity, knots TAS	66	
C.G.	33% MAC on thrust line		
CL	lift coefficient	.945	
CL_α	lift curve slope	4.78	4.77
Cm_α	pitch moment due to angle of attack	-2.12	-1.8
Cy_β	side force due to sideslip	-.819	-.2177
Cl_β	dihedral effect	-.023	-.565
Cn_β	weathercock stability	.109	.3151
$CL_{\delta e}$	lift due to elevator	.401	.407
$CD_{\delta e}$	drag due to elevator	.0180	.069
$Cm_{\delta e}$	pitch control power	-1.76	-1.833
$Cn_{\delta r}$	yaw control power	-.0917	-.2464
$Cy_{\delta r}$	sideforce due to rudder	.191	.2406
$Cl_{\delta r}$	roll due to rudder	-.00229	.0796

All coefficients are per radian.

F. SUMMARY

Drag polars were incorrectly predicted by numerical methods, half-scale flight testing, and full-scale glide tests. This conclusion assumes that the wind-tunnel results are the most accurate measurement of the Pioneer RPV's drag polar. A drag polar calculated from the full-scale glide test could be improved by including the residual thrust measured in the NAPC installed engine tests. The drag predicted from these glide tests did agree with the drag calculated from the wind-tunnel test at relatively high airspeeds where the NAPC test recorded zero residual thrust from an installed engine at idle. A windmilling or stopped propeller would add drag and reduce the glide performance considerably.

Longitudinal coefficients were very accurately predicted by the PMARC numerical methods for moderate angles of attack. Numerically-predicted directional coefficients differed significantly from those determined from the wind-tunnel test. For rudder deflections of less than 13 degrees, the numerically-determined sideslips in Reference 2 agreed with the wind-tunnel results, but the coefficients from which these predictions were calculated differed greatly. Numerically-predicted values should not be linearly extrapolated to determine performance capabilities and limitations.

VII. CONCLUSIONS

The recent success of the Pioneer RPV in the Gulf War increased awareness of the many uses of RPVs. Never before has the battlefield commander had such a quick, accurate and responsive intelligence-gathering platform both day and night. The Pioneer can also be used as a spotter for accurate ordnance delivery from either naval guns afloat or artillery ashore. As a radio-relay platform, the Pioneer RPV frees a multi-million-dollar manned aircraft for other missions and increases the range of our radio communications. Use of RPVs can keep our manned aircraft out of harm's way and free those assets for more critical roles requiring a pilot.

The aerodynamic analysis of the Pioneer RPV model tests in the Wichita State University wind tunnel by the Simulation Support Branch (Code 1074), PMTC in support of a training requirement for PMA-205 at NAVAIR yielded a mathematical description of its aerodynamic characteristics. The stability and control coefficients acquired and calculated from this wind-tunnel analysis can be combined using small-disturbance theory to produce an accurate real-time six-degree-of-freedom simulation of the Pioneer RPV.

This real-time simulation when married to a ground control station will permit realistic training of internal pilots. External pilots can be trained using a large-screen monitor displaying a three-dimensional Pioneer RPV flying in a realistic airfield environment.

The data acquired from the wind-tunnel testing was also used to predict aircraft performance. It has been shown that the c.g. envelope can be safely expanded, permitting flights without the use of extra lead weight in the aircraft's

nose to compensate for different payloads since the stick-fixed neutral point is always aft of 60% MAC. Excess weight above the Pioneer RPV's design weight drastically reduces its performance. Speeds for best endurance and best range were calculated and if used will result in improved mission profiles, enabling longer flight time on station without modification of the aircraft.

It is recommended that future flight testing be streamlined by incorporating these performance predictions. Since the shapes of the performance curves have been defined, flight tests can concentrate on validating and shifting these predicted curves to match actual flight data without having to define the entire curves. An accurate airspeed calibration must be conducted for a valid correlation of indicated flight speeds with those predicted, in particular at lower airspeeds.

REFERENCES

1. *JCS Pub 1-02, Department of Defense Dictionary of Military and Associated Terms*, 1 December 1989.

2. Hellman, P., *The Little Airplane That Could*, Discover, February 1987.

3. Lyons, D.F., *Aerodynamic Analysis of U.S. Navy and Marine Corps Unmanned Air Vehicle*, Masters Thesis, Naval Postgraduate School, Monterey, California, June 1989.

4. *Gulf War Experience Sparks Review of RPV Priorities*, Aviation Week & Space Technology, April 22, 1991.

5. *War Seen Boosting Prospects for Unmanned Aerial Vehicles*, Aerospace Daily, Vol. 158, No. 23, May 1, 1991.

6. Rae, W.H. Jr and Pope, A., *Low-Speed Wind Tunnel Testing*, John Wiley & Sons, Inc., 1984.

7. Phone Conversation, 6 March 1991 between author and Dr. D. Palumbo, AAI, Baltimore, Maryland.

8. Davidson, M.L., *Aeronautical Report 79-1, Facility Description of the 7 by 10 foot Walter H. Beech Memorial Low Speed Wind Tunnel*, Aeronautical Engineering Department, Wichita State University, Wichita, Kansas, January 1979.

9. Ross, G.B., *Three-Dimensional Boundary Corrections for the Walter H. Beech Memorial 7 by 10 Foot Low Speed Wind Tunnel*, Aeronautical Engineering Department, Wichita State University, Wichita, Kansas, April 1985.

10. Habluetzel, T., *Aeronautical Report 80-1, Three-Dimensional Force Data Acquisition and Reduction Routine for the Walter H. Beech Memorial 7 by 10 Foot Low Speed Wind Tunnel*, Aeronautical Engineering Department, Wichita State University, Wichita, Kansas, January 1980.

11. Glauert, H., *Wind Tunnel Interference on Wings, Bodies, and Airscrews*, R&M 1566, 1933.

12. Hurt, H.H., *Aerodynamics for Naval Aviators,* The Office of the Chief of Naval Operations Aviation Training Division, U.S. Navy, 1960.

13. Miley, S.J., *A Catalog of Low Reynolds Number Airfoil Data for Wind Turbine Applications*, Department of Aerospace Engineering, Texas A&M University, College Station, Texas, February 1982.

14. Raymer, D.P., *Aircraft Design: A Conceptual Approach*, AIAA Education Series, 1989.

15. Nelson, R.C., *Flight Stability and Automatic Control*, McGraw-Hill, Inc., 1989.

16. *USAF Stability and Control Datcom*, Douglas Aircraft Division of the McDonnel Douglas Corporation, 1976.

17. Lawton, J., *Altitude Test of the Pioneer Short Range Remotely Piloted Vehicle (RPV) Propulsion System*, Department of the Navy, Naval Air Propulsion Center, Trenton, New Jersey, 27 May 1988.

18. *Specifications of International RPVs and Drones*, Aviation Week & Space Technology, March 18, 1991.

19. Anderson, J.D., *Introduction to Flight,* McGraw-Hill , Inc., 1989.

20. Howard, R.M., Lyons, D.F., Tanner, J.C., *Research Flight Test of a Scaled Unmanned Air Vehicle*, 21st Annual Symposium Proceedings, Society of Flight Test Engineers, Garden Grove, California, 6-10 August 1990.

WICHITA STATE UNIVERSITY
7x10 FOOT LOW SPEED WIND TUNNEL

REMARKS FORCE RUNS
A ⇒ -10 to 12 by 2; 12 to 20 by 1
B ⇒ -24 to 16 by 2; -16 to 16 by 4; 16 to 24 by 2
C ⇒ -10; -6; -2 to 20 by 2
D ⇒ -24 to 24 by 4

TEST OF PIONEER RPV
FOR PACIFIC MISSILE
CONFIGURATION 3PT MOUNT ON EXTERNAL BALANCE

RUN NO. 1-10
DATE FEBRUARY 1991

DATE	RUN #	q	MC	ST	DT	RAW TAPE/FILE	RAW DISK/FILE	α	ψ	δ_e	δ_a/δ_r	RPM	PITCH	CAGE IN/OUT MODEL UP/DN	REMARKS				
2-4	2000	—	1	—	—	0-9/2	0-31/1.DAT	C	0	—	-/-	—	—	OUT/UP	STRUT PITCH STATIC TARE				
	2001	-		-	-	3		C	-10						"			"	
	2002	-		-	-	4		C	-20						"			"	
	3000	50		2000	-	5		C	0						STRUT PITCH DYNAMIC TARE				
	3001	50		2001	-	6		C	-10						"				"
	3002	50		2002	-	7		C	-20						"				"
															"				"
																			"
2-5	2003	—		—	—	8	2.DAT	C	0						PITCH STRUT OUT	PITCH	STATIC	TARE	
	3003	50		2003	—	9		C	0						PITCH STRUT OUT	PITCH	DYNAMIC	TARE	
	1000	—	2	—	—	10		C	0	0	0/0			IN/INV	MODEL PITCH STATIC TARE				
	1	50		1000	0	11		A	0										
	2	50		1000	0	12				+20									
	3	50		1000	0	13				-20					TAPED UPPER SURFACE TRUNNION				
	4	50		1000	0	14				0					REPEAT OF 1				
	1001	—	1	—	—	15		C						OUT/INV					
	5	50		1001	0	16		A											
	6	50		1001	0	17				-20									
	7	50		1001	0	18				20									
2-6	1002	—		—	—	19	3.DAT	C		0				OUT/UP	MODEL PITCH STATIC TARE				
															ADDED SECOND -10 TO SCHEDULE				
	8	50		1002	3004	0-10/2		A											
	9	50		1002	3004	3									REPEAT CHECK FOR RUN 8				
	10	50		1002	3004	4									CAGE OFF				

WICHITA STATE UNIVERSITY
7×10 FOOT LOW SPEED WIND TUNNEL

REMARKS FROM RUN 10 ON, THE BUBBLE CAGE IS REMOVED

TEST OF PIONEER RPV — RUN NO. ____
FOR PACIFIC MISSILE — DATE FEBRUARY 1991
CONFIGURATION 3FT MOUNT ON EXTERNAL BALANCE

DATE	RUN #	q	MIC	ST	OT	RAW TAPE/FILE	RAW DISK/FILE	α	ψ	δ_e	δ_a/δ_r	RPM	PITCH	IMAGE IN/OUT MODEL UP/DN	REMARKS				
2-6	3004	50	1	2000	—	0-10/—	0-31/3.DAT	C	0	0	0/0	—	—	OUT/UP	DUMMY	OT			
	3005	50		2000	—	—									DUMMY	OT			
	3006	50		2000	—	—									DUMMY	OT			
								↓											
	11	40		1002	3004	5		A							START OF Q SWEEP				
	12	20				6													
	13	10				7									END OF Q SWEEP				
	14	50				8				-5					START OF ELEVATOR POWER SWEEP				
	15	50				9				-10									
	16	50				10				-15									
	17	50				11				-20									
	18	50				12				-25									
	19	50				13				5									
	20	50				14	↓			0					REPEAT OF 10				
2-7	21	50				15	4.DAT			10									
	22	50				16				15					END OF ELEVATOR POWER SWEEP				
	23	50				17				20									
		SEE PRESSURE LOG FOR						ALPHA'S	24	-31									
					↓			↓	↓										
	2004	—			—	0-11/2		1	0	—	—				STRUT YAW STATIC TARE				
	2005	—			—	3		6							STRUT YAW STATIC TARE				

WICHITA STATE UNIVERSITY
7x10 FOOT LOW SPEED WIND TUNNEL

REMARKS 5 TUBE PROBE RUNS

α VAR ⇒ -2, 2, 6

F ⇒ 1.247, -0.6595, -2.7815

TEST OF PIONEER RPV

FOR PACIFIC MISSILE

CONFIGURATION 3PT MOUNT EXTERNAL BALANCE

RUN NO.

DATE FEBRUARY 1991

DATE	RUN #	q	RAW TAPE/FILE	RAW DISK/FILE	α	ψ	δ_e	δ_a	δ_r	RPM	PITCH	X PROBE "IN"	Z PROBE "IN"	ΔZ PROBE "IN"	PROBE TILT	SCAN POSITION				
2-7	24	50	D-10/18	D-31/4.DAT	VAR	0	0	0	0	—	—	400	F	0	0	3				
	25	50	19		VAR	0	0	0	0	—	—	400	F	0	0	3	Y=	4		
	26	50	20		VAR	0	0	0	0	—	—	400	F	0	0	3	Y=	14		
	27	50	20		VAR	0	0	0	0	—	—	350	F	0	0	3				
	28	50	21		VAR	0	0	0	0	—	—	350	F	0	0	3	TARE FOR 27			
	29	50	22		VAR	0	0	0	0	—	—	400	F	0	0	3	"		" 26	
	30	50	23		VAR	0	0	0	0	—	—	400	F	0	0	3	"		25	
	31	50	24		VAR	0	0	0	0	—	—	400	F	0	0	3	"		24	

WICHITA STATE UNIVERSITY
7×10 FOOT LOW SPEED WIND TUNNEL

REMARKS _____

TEST OF PIONEER UAV — RUN NO. 32 - 61
FOR PACIFIC MISSILE — DATE FEBRUARY 1991
CONFIGURATION 3PT MOUNT ON EXTERNAL BALANCE

DATE	RUN #	q	MC	ST	OT	RAW TAPE/FILE	RAW DISK/FILE	α	ψ	δ_e	δ_a/δ_r	RPM	PITCH	FLAPS IN/OUT AIL IN/UP		REMARKS				
2-7	1005	–	1	–	–	0-11/10	0-5/4.DAT	1°	A	0	0/-25	–	–	OUT/UP						
	1006	–		–	–	11		6°	A	0	0/-25	–	–							
	32	50		1005	3007	12		1	B											
	35			1006	3008	13		6	B											
	36			1005	3007	14		1	B		0/-20									
↓	37			1006	3008	15	↓	6	B		0/-20									
2-8	38			1005	3007	16	5.DAT	1	B		0/-15									
	39			1006	3008	17		6	B		0/-15									
	40			1005	3007	18		1	B		0/-10									
	41			1006	3008	19		6	B		0/-10									
	42			1005	3007	20		1	B		0/-5									
	43			1006	3008	21		6	B		0/-5									
	44			1005	3007	22		1	B		0/-2									
	45			1006	3008	24		6	B		0/-2									
	46			1005	3007	25		1	B		0/0									
	47			1006	3008	26		6	B		0/0									
	48			1005	3007	0-13/2		1	B		0/+2									
	49			1006	3008	3		6	B		0/+2									
	50			1005	3007	4		1	B		0/+5									
	51			1006	3008	5		6	B		0/+5									
	52			1005	3007	6		1	B		0/+10									
	53			1006	3008	7		6	B		0/+10									
	54			1002	3004	8		A	D		0/0									
	55			1005	3007	9		1	B		0/0									
	56			1002	3004	10		A	D		0/0					Baseline				
	57			1002	3004	11		E	D		0/0					ψ_{ACTUAL} =	-0.4			
	58			1005	3007	12		1	B		0/0					Baseline				
↓	59			1006	3008	13	↓	6	B		0/0					"				
2-11	60			1002	3004	0-15/2	6.DAT	A	D		0/0					REPEAT OF 56				
↓	61	↓		1002	3004	3		A	D		-20/0									

WICHITA STATE UNIVERSITY
7×10 FOOT LOW SPEED WIND TUNNEL

REMARKS _____

TEST OF PIONEER UAV — RUN NO. 62-

FOR PACIFIC MISSILE — DATE FEBRUARY 1991

CONFIGURATION 3PT AIRCRAFT W/ EXTERNAL BALANCE

DATE	RUN #	Q	MC	ST	DT	RAW TAPE/FILE	RAW DISK/FILE	α	ψ	δ_e	δ_a/δ_r	RPM	PITCH	IMAGE SNAPSHOT MODEL UP/DOWN	REMARKS				
2-11	62	50	1	1005	3007	D-15/4	0 51/6 DAT	1	B	0	20/0	—	—	OUT/UP					
	63			1006	3008	5		6	B		-20/0								
	64			1002	3004	6		A	0		20/0								
	65			1005	3007	7		1	B		20/0								
	66			1006	3008	8		6	B		20/0								
													↓						
	1007			—	—	9		C	0		0/0		19		REPEAT OF 1002.				
	67	20		1002	3004	10		-2	0		0/0	F							
	68			1002	3004	11	↓	-2	0		0/0	—							
2-12	69			1008	3004	12	7.DAT	-2	0		0/0	F	↓		REPEAT OF 67				
	70			1002	3004	13		-2	0				22						
	71					14		-2	0				25						
	72					15		-2	0				28						
	73					16		-2	0				40						
	74			1008		17		-2	0				40		REMOVED EXHAUST PODS				
				↓	↓														
	1008	—		—	—	18		C	0				↓		"	"	PROP ON		
	1009	—		—	—	19		C	0				—		"	"	PROP OFF		
	75	20		1009	3004	20		A	0				40						
		↓																	
	1010	—		—	—	21		C	0						EXHAUST PODS ON	PROP ON			
	76	20		1008	3004	22		-2	0			F	50						
	77	10				23		-2	0				40						
	78	15				24		-2	0				40						
	79	10				25		-2	0				34						
	80			1009		D-16½		A	0				↓		PROP OFF, REMOVED EXHAUST PODS				
	81	20		1008		3		G	0			G	40		PROP ON, EXHAUST OFF				
	82	10		↓	↓	4	↓	I	0			I	34		"	"	"	"	"	

WICHITA STATE UNIVERSITY
7x10 FOOT LOW SPEED WIND TUNNEL

REMARKS _____

TEST OF Pioneer UVM RUN NO. S3 - 112
FOR Pacific Missile Test Center DATE February 1991
CONFIGURATION 3 PT MOUNT ON EXTERNAL BALANCE

DATE	RUN #	Q	MC	ST	DT	RAW TAPE / FILE	RAW DISK / FILE	α	ψ	δ_e	δ_a/δ_r	RPM	PITCH	IMAGE ENABLE MODEL UPLINK OUT/UP		REMARKS				
2-13	83	10	1	1008	3004	D-15/5	8.DAT	I	0	0	0/0	I	34			PODS	OFF	Pop at 82		
	84			1005	3007	6		1	H	0	0/0	6600				"	"			
	85			1006	3008	7		6	H	0	0/0	7620				"	"			
	86			1003	3001	8		I	-10	0	0/0	I				"	"			
	87			1004	3002	9		I	-20	0	0/0	I				"	"			
	88			1008	3004	10		I	0	-5	0/0	I				"	"			
	89					11		I	0	-10	0/0	I				"	"			
	90					12		I	0	-15	0/0	I				"	"			
	91					13		I	0	-20	0/0	I				"	"			
	92					14		I		-25	0/0	I				"	"			
	93					15		I		5	0/0	I				"	"			
	94					16		I		10	0/0	I				"	"			
	95					17		I		15	0/0	I				"	"			
	96					18		I		20	0/0	I				"	"			
	97					19		J		0	0/0	J				"	"			
	98					20		-2		0	0/0	F(SPIRAL)				"	"	13.75 Blade		
	99					21		-2		0	0/0	F(SR-4 SPIRAL)28				"	"	"		
	100					22		-2		0	0/0	F(SR-4 SPIRAL)22				"	"	"		
	101					23		K		0	0/0	K				"	"	repeat of 97		
	102			1005	3007	24		1°	H	0	0/0	7812				"	"	13.75 "		
	103			1006	3008	25		6°	H	0	0/0	10335				"	"	"		
	104			1003	3001	26		K	-10	0	0/0	K				"	"	"		
	105			1004	3002	27		K	-20	0	0/0	K				"	"	"		
↓	106			1008	3004	28	↓	K	0	-5	0/0	K				"	"	"		
2-14	107					D-17/2	9.DAT	K		-10	0/0	K								
	108					3				-15										
	109					4				-20										
	110					5				-25										
	111					6				5										
	112	↓				7				10										

WICHITA STATE UNIVERSITY
7x10 FOOT LOW SPEED WIND TUNNEL

REMARKS

TEST OF PIONEER UAV RUN NO. 113-
FOR PACIFIC MISSILE DATE FEBRUARY 1991
CONFIGURATION 3PT MOUNT ON EXTERNAL BALANCE

DATE	RUN #	Q	MC	ST	DT	RAW TAPE/FILE	RAW DISK/FILE	α	ψ	δe	δa/δr	RPM	PITCH	ENGINE IN/OUT NOSE UP/DN		REMARKS			
2-14	113	10	1	1008	3004	0-17/8	0-31/9.DAT	K	0	15	0/0	K	22	OUT/UP					
	114					9		L		20									
	115					10		L		0		M							
	116					11,12		-2		0			16			4-BLADE PROP			
	117					13		1		0			19			"	"		
	118					14		P		0			↓			"	"		
	119	20		1010	3004	15		Q		0		Q	22			2 BLADE PROP	SMALL		
	120			1005	3007	16		1	H	0		6237							
	121			1006	3008	17		6	H	0		8466							
	122			1003	3001	18		Q	-10	0		Q							
	123			1004	3002	19		Q	-20	0									
	124			1010	3004	20			0	-5									
	125					21				-10									
	126					22				-15									
	127					23				-20									
	128					24				-25									
	129					25				5									
	130					26				10									
	131					27				15									
	132					28				20									
2-15	133	10		1010	3004	0-13/2	10.DAT	A	0	0		6865	34			α=6 Cruise Setting	small prop		
	135			1006	3008	3		6	11		0/-5								
	136					4		6			0/5								
	134			1005	3007	5		1			0/0	7900				α=1 Cruise Setting	REPEAT 84		
	1011	—		—	—	6		C	0			0	OFF			PROP OFF - WATER LINES IN			GENERIC PODS ON
	137	50		1011	3004	7		A	0										
	138					8					-5/0								
	139					9					5/0								

WICHITA STATE UNIVERSITY
7x10 FOOT LOW SPEED WIND TUNNEL

REMARKS

TEST OF PIONEER UAV — RUN NO. 140-
FOR PACIFIC MISSILE — DATE FEBRUARY 1991
CONFIGURATION 3PT MOUNT ON EXTERNAL BALANCE

DATE	RUN #	Q	AC	ST	DT	RAW TAPE/FILE	RAW DISK/FILE	α	ψ	δ_e	δ_a/δ_r	RPM	PROP PITCH	EMBOD ENGINE MODEL UP/DN	REMARKS			
2-15	140	50	1	1011	3004	D-19/10	D-21/10.DAT	A	0	0	+10/0	—	OFF	OUT/UP				
	141					11					+15/0							
	142					12					+20/0							
	143					13					+25/0							
	1012	—		—	—	14		C			0/0				NO CAMERA BUBBLE			
	144	50		1012	3004	15		C			0/0				" "	"		
	145	↓		↓	↓	16		↓	↓		0/0				NO BUBBLE & NO ANTENNA			
	1013					17		6	H		0/0				NO VERTICAL TAILS TABE			
	1'																	
↓	146	50		1013	3008	18	↓				0/0				"	"	"	
2-18							11.DAT											
	1014	—		—	—	19		C	0									
	147	50		1014	3004	20		A			0/OFF							
	148					21					0/OFF				HORIZONTAL TAIL INVERTED			
	149			1012		22					0/0				VERTICAL TAILS ON			
2-19																		
	1015	—		—	—	23		C			0/0							
	150	50		1015	3004	24									FUSELAGE OUT			
	151			1012		25									NO DOME NO ANTENNA			
	1016	-		—	—	26									"	"	"	NO GEAR
	152	50		1016	3004	27		↓						↓	"	"	"	"
2-20																		
	1017	—	2	—	—	D20/2	12.DAT	C						IN/UP	BASELINE CONFIG W/ IMAGE			
	153	50		1017	0	3		A										
	EOT																	

CUSTOMER	PACIFIC MISSILE
MODEL	PIONEER RPV
TYPE TEST	3PT MOUNT EXTERNAL BALANCE
DATE 2-4-91	DISC ID GEN DAT VIII

PROGRAM B913D::-

	D.FILE	NO.	CODE	LU	
5	M.C.	2	B91MC	-20	5
15	STATS	3	B91SDT	-20	15
130	S.T.	7	B91ST	-21	32
60	D.T.	8	B91DT	-21	30
	CL-CD	8	—		
4500	RAW	11	B91RAW	-20	450
2250	FINAL	12	B91RED	-20	450
300	DYN TARES	13	B91DTR	-22	30
500	ST TARES	14	B91STR	-22	50
2250	BODY	15	1391BOD	-20	450
2250	STABILITY	16	B91STA	-20	450

DATE	BARO. PRESS.
2-4	/ 2882 /
2-5	2887/2884 /
2-6	2887/2889
2-7	2901
2-8	2886
2-11	2883
2-12	2867
2-13	2824
2-14	2860
2-15	2884
2-18	2845
2-19	2884
--20	2884 in Hg

MODEL CONSTANTS

TABLE	DESCRIPTION
1	BASELINE
2	BASELINE WITH IMAGE SYSTEM

STATIC TARES

RUN	DESCRIPTION
1000	INVERTED IMAGE SYSTEM IN

DYNAMIC TARES

RUN	DESCRIPTION

RECORDED DATA

TABULATED	TYPE	NO.
WIND		
BODY	2	
STABILITY	1	
STORED	DISC	TAPE
WIND	X	
BODY	X	
STABILITY	X	

PLOTTING

	STAB ALPHA	PSI	BETA
X-AXIS	-8 to 24		-16 to 16
CL	2/1		2/1
CD	5/.2		5/.2
CM	7/1		9/.1
CRM	7/.10		7/.1
CYM	7/.10		7/.1
CY	7/.05		9/.1

Working Copy

All runs q = 20 unless otherwise noted

Run	α	β	δ_e	δ_a	δ_r	Plot	Data Sought	Comments
~~1~~	Y	0	0	0	0		Calibrate alpha Weight tares	Initial runs included static + dynamic tares for the model support system
~~2~~	0	Y	0	0	0		Calibrate beta Weight tares	set,
~~—~~	~~Y~~	~~0~~	~~0~~	~~0~~	~~0~~		~~Tare/Interfer~~	upright w/image
~~—~~	~~Y~~	~~0~~	~~0~~	~~0~~	~~0~~		~~Tare/Interfer~~	upright
~~—~~	~~Y~~	~~0~~	~~-1.5~~	~~0~~	~~0~~		~~Tare/Interfer~~	upright
~~—~~	~~Y~~	~~0~~	~~1.5~~	~~0~~	~~0~~		~~Tare/Interfer~~	upright
5	Y	0	0	0	0	C_L vs α	Tare/Interfer	inverted with landing cage
7	Y	0-20	~~-1.5~~	0	0		Tare/Interfer	inverted "
6	Y	0 20	~~1.5~~	0	0		Tare/Interfer	inverted "
1	Y	0	0	0	0		Tare/Interfer	inverted w/ image "
3	Y	0-20	~~-1.5~~	0	0		Tare/Interfer	inverted w/ image "
2	Y	0 20	1.5	0	0		Tare/Interfer	inverted w/image "
8	Y	0	0	0	0	C_L vs α	Baseline	~~1 deg increments~~ with landing cage
9	Y	0	0	0	0	C_L vs α	Baseline	for repeatability with landing cage
~~—~~	~~Y~~	~~0~~	~~0~~	~~0~~	~~0~~		~~Downwash~~	~~5 pressure probe~~
11	Y	0	0	0	0		Reynolds effect	q=40 w/out landing cage
12	Y	0	0	0	0		Reynolds effect	q=20 " " "
13	Y	0	0	0	0		Reynolds effect	q=10 " " "
10	Y	0	0	0	0	*	Baseline	w/out landing cage
4	Y	0	0	0	0		T/I	inverted w/image (repeat #1)
54	Y	0	0	0	0		Baseline	air scoops removed
55	1°	Y	0	0	0			

On 0s higher than Run 1 elevator trim on the vice center

Run	α	β	δ_e	δ_a	δ_r	Plot	Data Sought	Comments
								Want alpha for 1.2 Vstall $\alpha = 6^\circ$
47	6°	Y	0	0	0		Rudder Power	Baseline
49	↓	Y	0	0	2		Rudder Power	
51		Y	0	0	5		Rudder Power	
53		Y	0	0	10		Rudder Power	
45		Y	0	0	-2		Rudder Power	
43		Y	0	0	-5		Rudder Power	
41		Y	0	0	-10		Rudder Power	
39		Y	0	0	-15		Rudder Power	
37		Y	0	0	-20		Rudder Power	
35	↓	Y	0	0	-25		Rudder Power	
								Want alpha for 1.2 Vstall $\alpha = 6^\circ$
59	6°	Y	0	0	0		Aileron Power	
~~—~~	↓	~~Y~~	0	~~-5~~	0		~~Aileron Power~~	
~~—~~		~~Y~~	0	~~-10~~	0		~~Aileron Power~~	
~~—~~		~~Y~~	0	~~-15~~	0		~~Aileron Power~~	
63		Y	0	-20	0		Aileron Power	
~~—~~		~~Y~~	0	~~5~~	0		~~Aileron Power~~	
		Y	0	10	0		Aileron Power	
~~—~~		~~Y~~	0	~~15~~	0		~~Aileron Power~~	
66		Y	0	20	0		Aileron Power	after run ~~Repeated~~ aileron power checked α (more runs .1° high) (reset α = 0)
~~—~~		~~Y~~	0	~~25~~	0		~~Aileron Power~~	
~~—~~	↓	~~Y~~	0	~~-25~~	0		~~Aileron Power~~	
60	↓	0	0	0	0		Aileron Power	repeat of 56
								repeat of 58
								repeat of 59

Run	α	β	δ_e	δ_a	δ_r	Plot	Data Sought	Comments
20	Y	0	0	0	0		Elevator Power	- check α after releveling
14	Y	0	-5	0	0		Elevator Power	w/out landing cage
15	Y	0	-10	0	0		Elevator Power	"
16	Y	0	-15	0	0		Elevator Power	"
17	Y	0	-20	0	0		Elevator Power	"
18	Y	0	-25	0	0		Elevator Power	← " re-leveled mount
19	Y	0	5	0	0		Elevator Power	" after rotor
21	Y	0	10	0	0		Elevator Power	" break down.
22	Y	0	15	0	0		Elevator Power	"
23	Y	0	20	0	0		Elevator Power	"
33	Y	10	0	0	0		Effect of Yaw	on static longitudinal stability
34	Y	20	0	0	0		Effect of Yaw	on static longitudinal stability
~~—~~	~~Y~~	~~30~~	~~0~~	~~0~~	~~0~~		~~Effect of Yaw~~	~~on static longitudinal stability~~
								Want alpha for 90 knots (low priority)
46	1°	Y	0	0	0		Rudder Power	Baseline $\alpha = 1^\circ$
48	|	Y	0	0	2		Rudder Power	
50	|	Y	0	0	5		Rudder Power	
52	|	Y	0	0	10		Rudder Power	
44	|	Y	0	0	-2		Rudder Power	
42	|	Y	0	0	-5		Rudder Power	
40	|	Y	0	0	-10		Rudder Power	
38	|	Y	0	0	-15		Rudder Power	
36	|	Y	0	0	-20		Rudder Power	
32	↓	Y	0	0	-25		Rudder Power	

Run	α	β	δ_e	δ_a	δ_r	Plot	Data Sought	Comments
137	Y	0	0	0	0		Aileron Power	Baseline w/ motor installed 110 psig
142	Y	0	0	20	0		Aileron Power	Want alpha for 90 knots (low priority)
58	1°	Y	0	0	0		Aileron Power	Baseline $\alpha = 1^\circ$
		Y	0	-5	0		Aileron Power	
		Y	0	5	0		Aileron Power	
		Y	0	10	0		Aileron Power	
		Y	0	15	0		Aileron Power	
65		Y	0	20	0		Aileron Power	
		Y	0	25	0		Aileron Power	
		Y	0	-10	0		Aileron Power	
		Y	0	-15	0		Aileron Power	
62		Y	0	-20	0		Aileron Power	
	V	Y	0	-25	0		Aileron Power	
56	Y	0	0	0	0			Baseline repeat
138	Y	0	0	-5	0			
	Y	0	0	-10	0			
	Y	0	0	-15	0			
61	Y	0	0	-20	0			
	Y	0	0	-25	0			
139	Y	0	0	5	0			
140	Y	0	0	10	0			
141	Y	0	0	15	0			
64	Y	0	0	20	0			
143	Y	0	0	25	0			
57	Y	0	0	0	0			repeat of 56 with $\gamma = -.4$ @ $\alpha = 0$ for $C_Y = 0$ wind on
24	* Y	0	0	0			Downwash	Position 1
25	* Y	0	0	0			"	2
26	* Y	0	0	0			"	3
27	* Y	0	0	0			"	4
	* Y	0	0	0			"	5

31
30
29
28

Run	α	β	δ_e	δ_a	δ_r	Plot	Data Sought	Comments
	Y	0	0	0	0	$C_m - \alpha$	H Tail	
149	Y	0	0	0	0	$C_m - \alpha$	"	horizontal stab inverted to $i_t = +3°$ no bubble
148	Y	0	0	0	None		Vertical stab	removed horiz stab inverted no bubble
146	6°	Y	0	0	None		vertical stab	removed no bubble
147	Y	0	0	0	None		"	" no bubble
144	Y	0	0	0	0		C_D bubble	remove bubble new static tare taken
145	Y	0	0	0	0		C_D antenna	remove bubble and antenna
152		0	0	0	0		C_D " wingpen	remove landing gear, bubble, antenna
	Y	0	0	0	0	$C_L - \alpha$	wing alone	
151							repeat 145	remove bubble antenna slight diff
153							up flow	upright W image tests
							270 Hz	flow vis blade angle 40° small prop
							rpm 8100	geometric rpm
150	Y	0	0	0	0			wing only

Working Copy Q=20 for all powered runs

Run	α	β	δ_e	RPM	Pitch	Plot	Data Sought	Comments with propeller
					Blade			
~~——~~	~~Y~~	~~0~~	0	0	0		~~Tare~~/Interfer	upright - w/image
~~——~~	~~Y~~	0	0	0	0		~~Tare~~/Interfer	upright
~~——~~	~~Y~~	0	-1.5	0	0		Tare/Interfer	upright
~~——~~	~~Y~~	0	1.5	0	0		Tare/Interfer	upright
——	Y	0	0	0	0		Tare/Interfer	inverted
——	Y	0	-1.5	0	0		Tare/Interfer	inverted
——	Y	0	1.5	0	0		Tare/Interfer	inverted
~~——~~	~~Y~~	0	0	0	0		~~Tare~~/Interfer	inverted - w/ image
——	Y	0	-1.5	0	0		Tare/Interfer	inverted - w/ image
——	Y	0	1.5	0	0		Tare/Interfer	inverted w/image
	Y	0	0	0	0		Baseline	
						Q=20		**Powered Calibration Runs**
~~—~~	~~-2~~	~~0~~	~~0~~	~~Y~~	73°		C_D vs RPM	$T_c' = C_{D(power\ off)} - C_{D(power\ on)}$
67	-2	0	0	Y	16°			using old static tares
69	-2	0	0	Y	19°			
70	-2	0	0	Y	22°			
71	-2	0	0	Y	25°			
72	-2	0	0	Y	28°			
73	-2	0	0	Y	40°			
68	-2	0	0	0	No prop			1st Q=20 Cp run
74	-2	0	0	Y	40°#			Removed engine cooling fins
76	-2	0	0	Y	50#			reached temp limit on engine
77	-2	0	0	Y	40#			*Q=10
78	-2	0	0	Y	40#			*Q=15
79	-2	0	0	Y	34*			*Q=10
80	-2	0	0	Y	No blade	#	Baseline	Q=10 cooling fins removed
75	Y	0	0	0	No blade	#		Baseline cooling fins removed

cooling fins removed

no ceiling fins
Prop β = 34°

Q = 10 all Cruise Runs

Run	α	β	δ_e	RPM	Pitch	Plot	Data Sought	Comments 30% Power
81	Y	0	0		40°		Elevator Power	prop β = 40°, maximum power UNABLE to hold power high for Climb stall
88	Y	0	-5		34°		Elevator Power	
89	Y	0	-10				Elevator Power	
90	Y	0	-15				Elevator Power	
91	Y	0	-20				Elevator Power	
92	Y	0	-25				Elevator Power	
93	Y	0	5				Elevator Power	
94	Y	0	10				Elevator Power	
95	Y	0	15				Elevator Power	
96	Y	0	20				Elevator Power	
82	Y	0	0				Baseline	Q = 10 Matching T = 0
83	Y	0	0				Baseline repeat	1 of 82 if only good data point
84	1°	Y	0				Directional Stab	alpha for 1.2 Vstall = 65 knots
85	6°	Y	0				Directional Stab	alpha for 90 knots (low priority)
86	Y	10	0	0	0		Effect of Yaw	on static longitudinal stability
87	Y	20	0	0	0		Effect of Yaw	on static longitudinal stability
	~~Y~~	~~30~~	~~0~~	~~0~~	~~0~~		~~Effect of Yaw~~	~~on static longitudinal stability~~
133	Y	0	0	65 or 1.2	34°		Power = 4 for α = 6°	
135	6°	Y	0	δ_r = -15			Rudder Power	
136	6°	Y	0	δ_r = +15			Rudder Power	
134	10	Y	0					

Q=10

Run	α	β	δ_e	RPM	Pitch	Plot	Data Sought	Comments 100% Power
97	Y	0	0		34*		Elevator Power	couldn't reach max power - didn't account for
106	Y	0	-5		22%		Elevator Power	
107	Y	0	-10				Elevator Power	
108	Y	0	-15				Elevator Power	
109	Y	0	-20				Elevator Power	
110	Y	0	-25				Elevator Power	
111	Y	0	5				Elevator Power	
112	Y	0	10				Elevator Power	
113	Y	0	15				Elevator Power	
114	Y	0	20		↓		Elevator Power	
Base 101	Y	0	0		22%		"	repeat run 97 w/ prop β = 22(% 13.75" blade)
* 115	Y	0	0				C_L - α w/ Power	Stall power to α = 6° climb w/ α = 6° power 5 = 11.4
102	1°	Y	0				Directional Stab	alpha for 1.2 Vstall
103	6°	Y	0		↓		Directional Stab	alpha for 90 knots (low priority)
118	Y	0	0		19*		Full Power 4-6	idle
104	Y	10	0	0	0 22?		Effect of Yaw	on static longitudinal stability
105	Y	20	0	0	0 ↓		Effect of Yaw	on static longitudinal stability
~~——~~	~~Y~~	~~30~~	~~0~~	~~0~~	~~0~~		~~Effect-of-Yaw~~	~~on static longitudinal stability~~
98	-2	0	0	Y	34%		T_c Q=10	13.75" blade prop pitch (34% no Cooling flow 13.75" blade
99	-2	0	0	Y	28?		Q=10	"
100	-2	0	0	Y	22%		"	"
116	-2	0	0	Y	22*		" (* 4 blade = 13.75")	
117	-2	0	0	Y	19*		"	4 blade = 13.75"

A idle runs Q = 20

Run	α	β	δ_e	RPM	Pitch	Plot	Data Sought	Comments Idle
119	Y	0	0		22°		Elevator Power	Small prop cylinders
124	Y	0	-5				Elevator Power	
125	Y	0	-10				Elevator Power	
126	Y	0	-15				Elevator Power	
127	Y	0	-20				Elevator Power	
128	Y	0	-25				Elevator Power	
129	Y	0	5				Elevator Power	
130	Y	0	10				Elevator Power	
131	Y	0	15				Elevator Power	
132	Y	0	20				Elevator Power	
120	1°	Y	0				Directional-Stab	alpha for 1.2 Vstall
121	6°	Y	0				Directional-Stab	alpha for 90 knots (low priority)
122	Y	10	0	0	0		Effect of Yaw	on static longitudinal stability
123	Y	20	0	0	0		Effect of Yaw	on static longitudinal stability
~~——~~	~~Y~~	~~30~~	~~0~~	~~0~~	~~0~~		~~Effect of Yaw~~	~~on static longitudinal stability~~

INITIAL DISTRIBUTION LIST

		No. Copies
1.	Defense Technical Information Center Cameron Station Alexandria, Virginia 22314-6145	2
2.	Library, Code 52 Naval Postgraduate School Monterey, California 93943-5100	2
3.	Commandant of the Marine Corps Code TE 06 Headquarters, U.S. Marine Corps Washington, D.C. 20380-0001	1
4.	Chairman, Code AA Department of Aeronautics and Astronautics Naval Postgraduate School Monterey, California 93943-5100	1
5.	Professor R. M. Howard, Code AA/Ho Department of Aeronautics and Astronautics Naval Postgraduate School Monterey, California 93943-5100	1
6.	Professor L. V. Schmidt, Code AA Department of Aeronautics and Astronautics Naval Postgraduate School Monterey, California 93943-5100	1
7.	Captain Robert M. Bray USMC 1016 Hideaway Ln Estes Park, Colorado 80517	1
8.	Simulation Support Branch (Code 1074) Pacific Missile Test Center ATTN: Keith Bratberg Point Mugu, California 93042-5000	1

9. Commanding Officer 1
Unmanned Air Vehicles Joint Project
Naval Air Systems Command
ATTN: PMA 205
Washington, D.C. 20361-1263

10. Commanding Officer 1
Marine Corps Test & Evaluation Agency
ATTN: Maj Heikes
Quantico, Virginia 22134

11. Commanding Officer 1
Unmanned Air Vehicles Joint Project
Naval Air Systems Command
ATTN: PMA 263M
Washington, D.C. 20361-1263

12. Commanding Officer 1
UAV Office
Code 1098
ATTN: Maj Horne
Pacific Missile Test Center
Point Mugu, California 93042-5000

13. Commanding Officer 1
Marine Aviation Detachment
ATTN: Capt Ballinger
Pacific Missile Test Center
Point Mugu, California 93042-5000